Diss. ETH No. 19218

Accelerated Magnetic Resonance Myocardial Perfusion Imaging

A thesis submitted for the degree of

DOCTOR OF SCIENCES

to the

ETH ZURICH

presented by

Viton Vitanis
Dipl. Eng. Aristotle University of Thessaloniki
born February 15, 1982
citizen of Greece

accepted on the recommendation of

Prof. Dr. Peter Boesiger, examiner
Prof. Dr. Sebastian Kozerke, co-examiner
Prof. Dr. René Botnar, co-examiner

Zurich, 2010

ABSTRACT

Ischemic heart disease refers to a discrepancy between oxygen demand and supply which is most often caused by insufficient blood flow to parts of the myocardium. This reduced blood flow is the precursor to acute myocardial infarction (heart attack) and cardiac arrest leading to sudden death. Considering that cardiovascular diseases account for approximately 4.3 million deaths in Europe each year, half of which are coronary disease related, there is a consensus that early diagnosis of ischemia is of great importance.

A method to detect ischemia using Magnetic Resonance Imaging (MRI) is based on the assessment of the first passage of paramagnetic contrast material through the myocardium. Despite having several advantages over methods utilized on other imaging modalities, such as catheter-based angiography or radionuclide imaging, first-pass myocardial perfusion MRI presents a number of challenges. The most important among those is the relatively long duration of the imaging process, related to the fact that MR images are acquired in the Fourier domain, also referred to as *k*-space. Considering that perfusion imaging requires both high spatial and high

temporal resolution as well as large coverage of the heart, one can infer that the acquisition speed is a crucial factor for obtaining diagnostically reliable perfusion information.

In this thesis the application of novel parallel imaging methods to accelerate first-pass perfusion MRI is proposed. Those methods, based on undersampling the *k*-space over time, reconstruct images of high quality by exploiting the spatial encoding capabilities of receiver coil arrays along with spatiotemporal correlations that are present in dynamic image series of natural objects.

The first reconstruction method proposed here is a modification of *k-t* SENSE, which aims at increasing acquisition speed (8× undersampling) without compromising image quality. In *k-t* SENSE, MR data acquisition performed in parallel by multiple coils is accelerated by sparsely sampling the *k*-space over time (*k-t* space). The resulting aliasing is resolved in the reciprocal *x-f* space by drawing signal distribution information from a low-resolution training data set. A drawback of the method is the temporal filtering observed with increasing acceleration factors. The acquisition of a higher resolution training data set could alleviate this issue, however at the expense of acquisition time. The new technique is based on applying parallel imaging on the training data in order to increase their spatial resolution, while keeping the same number of acquired training profiles. Employing two-dimensional (2D) multi-slice imaging at a net acceleration of 5.8 (*k-t* factor=8, training profiles=11) accurate representations of dynamic signal-intensities were achieved. The efficacy of this approach as well as limitations due to noise amplification were first investigated in computer simulations. A study comprising 20 patients demonstrated further the clinical performance of the technique.

The second reconstruction method, motivated by the necessity for larger myocardial coverage and built upon the *k-t* Principle Component Analysis (PCA)framework, was designed to accelerate imaging even further (10× undersampling). *k-t* PCA is an extension of *k-t* SENSE and is based on a transformation of the training data from the *x-f* domain to a coefficient *x-pc* domain, obtained after applying PCA. The advantage of this technique lies in its efficiency in reconstructing non-periodic dynamic signals. This work proposes a compartment-based *k-t* PCA reconstruction approach that addresses important issues in perfusion imaging, namely temporal filtering and signal contamination in the septal wall. Those issues are introduced due to partial-volume effects in the low-resolution training data. Using prior knowledge related to the temporal evolution of the contrast bolus passage through different cardiac compartments, voxels that exhibit non-physiological signal evolution over time are excluded from the calculation of the Principle Components of the training data. This scheme was shown to be more robust than previous methods against temporal filtering and signal contamination and rendered three-dimensional (3D) myocardial perfusion imaging feasible under hyperemic conditions and at high resolution (2.3×2.3 mm^2).

Finally, it was investigated in this thesis whether perfusion quantification methods could successfully be employed in conjunction with spatiotemporal reconstruction methods, such as the ones mentioned above. Widespread adoption of perfusion quantification in a clinical setting has been hampered by the complexity of its application: The nonlinear relationship between signal intensity and contrast agent concentration, signal saturation, regional variations in the B1 and B0 fields, breathing motion and registration have rendered quantification highly involved and limited its application to relatively low-resolution 2D image series. The effects of spatiotemporal acceleration on perfusion quantification were investigated, its limitations were delineated and finally its feasibility when a particular reconstruction procedure is employed was demonstrated.

In conclusion, the present dissertation promotes the application of accelerated parallel imaging to assess myocardial perfusion. To this end, it is demonstrated that the development and utilization of image reconstruction methods that permit faster acquisitions in 2D and 3D could enhance the diagnostic ability of MRI and consequently contribute to its establishment in the clinics as a reliable modality to assess ischemic heart disease.

ZUSAMMENFASSUNG

Die ischämische Herzkrankheit beruht auf dem Missverhältnis zwischen Sauerstoffbedarf und Sauerstoffangebot, welches oft auf einen verminderten Blutfluss durch Teile des Myokards zurückzuführen ist. Dieser reduzierte Blutfluss ist eine Vorstufe des akuten Myokardinfarktes und des Herzstillstands, welcher einen akuten Herztod zur Folge haben kann. Jährlich sterben in Europa 4.5 Millionen Menschen an kardiovaskulären Erkrankungen, wobei die Hälfte der Fälle aufgrund koronarer Herzerkrankungen zu verzeichnen ist. Deshalb ist die frühzeitige Diagnose einer Ischämie von grosser Bedeutung.

Ein Verfahren zur Ischämiedetektion mittels Magnetresonanztomographie (MRT) basiert auf der Bestimmung des "first-pass" eines paramagnetischen Kontrastmittels durch das Myokard. Ungeachtet der zahlreichen Vorteile gegenüber anderen bildgebenden Modalitäten, stellt die first-pass Myokardperfusions-MRT eine Reihe von Herausforderungen. Insbesondere gilt die relativ lange Akquisitionsdauer als problematisch, da diese intrinsisch mit dem MRT-Verfahren verbunden ist, welches Bilder in der Fourier-Domäne, auch *k*-Raum gennant, kodiert. Zieht man in

Betracht, dass die Perfusionsbildgebung sowohl eine hohe örtliche und zeitliche Auflösung als auch eine grosse räumliche Abdeckung erfordert, wird klar, dass die Akquisitionsgeschwindigkeit ein entscheidender Faktor ist, um Bilder mit hoher diagnostischen Relevanz aufzunehmen.

In der vorliegenden Dissertation werden neue Methoden zur Beschleunigung der first-pass Perfusions-MRT mittels paralleler Bildgebung beschrieben. Diese Verfahren beruhen auf der Unterabtastung des *k*-Raums über die Zeit und erlauben die Rekonstruktion von Bildern mit hoher Qualität, indem sie das örtliche Kodierpotenzial von Spulenelementen und die in der Bildgebung von natürlichen Objekten bestehenden örtlichen und zeitlichen Korrelationen verwerten.

Die erste hier vorgeschlagene Rekonstruktionsmethode erweitert das *k-t* SENSE Prinzip und erlaubt eine erhöhte Akquisitionsgeschwindigkeit (8× Unterabtastung) ohne die Bildqualität zu beeinträchtigen. In *k-t* SENSE wird die mittels mehrerer Spulen parallel durchgeführte Datenaufnahme durch Unterabtastung des *k*-Raums über die Zeit (*k-t* Raum) beschleunigt. Die resultierenden Signalfaltungen werden im reziproken *x-f* Raum durch die Verwendung zusätzlicher Informationen, welche durch einen niedrig aufgelösten Datensatz gewonnen werden, korrigiert. Ein Nachteil der Methode besteht in der Dämpfung hochfrequenter zeitlicher Signalanteile – ein Effekt der mit grösseren Unterabtastfaktoren verstärkt wird. Die Aufnahme eines höher aufgelösten Trainingsdatensatzes kann dieses Problem reduzieren, jedoch wird dadurch auch die Messzeit verlängert. Das in dieser Dissertation vorgeschlagene Verfahren beruht auf der Anwendung der parallelen Bildgebung auf den Trainingsdaten. Entsprechend kann damit eine erhöhte räumliche Auflösung erzielt werden, ohne dabei die Anzahl der akquirierten Trainingsprofile zu ändern. Es konnte gezeigt werden, dass das Verfahren die Aufnahme zweidimensionaler (2D) Mehrschichtbilder mit einer Netto-Beschleunigung von 5.8 (*k-t* factor=8, Trainingsprofilen=11) mit hoher Detailtreue der dynamischen Signalanteile ermöglicht. Anhand von Computersimulation wurden die Wirksamkeit dieser Methode sowie Einschränkungen durch Rauschverstärkung untersucht. In einer klinischen

Studie in 20 Patienten konnte gezeigt werden, dass die neu entwickelte Methode eine hervorragende diagnostische Qualität liefert.

Eine weitere im Rahmen dieser Dissertation entwickelte Methode erlaubt die dreidimensionale Darstellung der Herzens. Diese auf der *k-t* Principal Component Analysis (PCA) Technik beruhende Methode erlaubt eine bisher unerreichte Beschleunigung der Datenaufnahme (10× Unterabtastung). *k-t* PCA ist eine Erweiterung von *k-t* SENSE und verwendet eine Transformation der Trainingsdaten aus der *x-f* Darstellung in einen Koeffizientenraum, welche als *x-pc* Raum bezeichnet wird. Dieser Koeffizientenraum wird durch eine Hauptkomponentenanalyse (englisch: Principal Component Analysis, PCA) berechnet. Dieses Verfahren kann insbesondere nicht periodische dynamische Signale sehr effizient kodieren. Im Rahmen dieser Arbeit wurde die Methode erweitert, indem räumliche Kompartimente definiert wurden. Diese reduzieren Signalkontaminationen als Folge von Teilvolumeneffekten vor allem in Bereichen des Septums des Herzens, welche sich als problematisch in der beschleunigten Perfusionsbildgebung herausgestellt haben. Unter Verwendung von Vorwissen, bezogen auf die zeitliche Entwicklung des Kontrastmittelbolus in verschiedenen Bereichen des Myokards, konnten nicht physiologische Signalanteile von der Berechnung der Hauptkomponenten der Trainingsdaten ausgeschlossen werden. Es wurde gezeigt, dass dieses Schema zeitliche Filterung und Signalkontaminierung signifikant reduziert und damit die dreidimensionale Perfusionsbildgebung des Myokards unter hyperaemische Bedingungen und mit hoher örtlicher Auflösung (2.3×2.3 mm^2) ermöglicht.

In einem dritten Schwerpunkt wurde in dieser Dissertation untersucht, ob Methoden zur Quantifizierung der Perfusion in Verbindung mit einer beschleunigten Datenaufnahme, welche auf örtlicher und zeitlicher Unterabtastung basiert, Verwendung finden können. Quantifizierungsmethoden für die Perfusionsbestimmung sind sehr komplex und haben daher bisher keine Verwendung in der klinischen Diagnostik gefunden. Folgende Faktoren spielen in diesem Zusammenhang eine Rolle: das nichtlineare Verhältnis zwischen Signalintensität und Kontrastmittel-Konzentration, Signalsättigung, räumliche Variationen der B1 und B0 Felder, Atembewegung, sowie die Bilderregistrierung. Entsprechend wurden Quantifizierungmethoden bisher nur auf relativ niedrig aufgelösten 2D Bilder angewendet. In dieser Arbeit wurden die Effekte der beschleunigten Bildgebung auf die Quantifizierung der Perfusion untersucht, Limitationen bestimmt und schließlich die praktische Anwendung erprobt.

CONTENTS

CHAPTER 1

INTRODUCTION

Cardiovascular diseases (CVD) present a major cause of morbidity and mortality on a global scale. According to the World Health Organization (WHO), an estimated 17 million people died from CVD in 2002, representing 30% of all global deaths in that year [1]. More recent statistics (see Section 1.1) confirm the fact that CVD are the single leading cause of death nowadays.

In the first section of this chapter, statistics with respect to the burden of CVD in Europe and the United States are presented, including data on death, illness, treatment, and an estimate of economic costs associated to those diseases. Focus will be given to the most prevalent cardiovascular disease, Ischemic Heart Disease (IHD), also referred to as Coronary Heart Disease or Coronary Artery Disease. Aim of this analysis is to demonstrate the necessity of early diagnosis of CVD and in particular IHD, which in turn motivated the work presented in this thesis. More details regarding the motivation are presented in Section 1.2. In the third section of this chapter the contribution of the dissertation with respect to the assessment of the IHD is elaborated. Finally, a short description of the chapters to follow is given.

1.1 Statistics

Cardiovascular diseases (CVD) are the main cause of mortality in Europe and the United States[1]. Each year they cause over 4.3 million deaths in Europe [2] and approximately 900,000 deaths in the United States [3].

The main forms of CVD are Ischemic Heart Disease (IHD) and stroke. The former by itself is the single most common cause of death in westernized societies, accounting for 1.92 million deaths in Europe and 450,000 deaths in the US every year.

Comparable data on morbidity from IHD are more difficult to collect than mortality data, but the trends presented by the WHO MONICA project in 2002 confirm the high morbidity rates caused by CVD [4]. The main measure of the disease burden was the DALY (Disability Adjusted Life Year) –an aggregate of years of life lost due to premature death and years of healthy life lost due to disability. According to this report, CVD account for 10% of all DALYs lost in WHO regions, a third of which lost by IHD alone.

A recent cost-of-illness study in the European Union (EU) estimated that CVD cost approximately €170 billion annually [5]. This number included healthcare costs, informal care costs and productivity loss. In the US, the same cost was estimated to be $450 billion [6]. IHD alone was estimated to have cost the EU €45 billion (2006 statistics) and the US $156 billion (2008 statistics).

Focusing on IHD, it should be noted that the aforementioned reports show a general trend of reduction in the number of IHD patients in the past few years. However, the burden due to the disease remains high. Considering in addition the fact that an ischemic episode (see Chapter 2)

---

[1] The comparison is being made between “Diseases of the circulatory system” (Chapter IX 10th Revision) of the International Classification of Diseases, and diseases of other chapters (e.g. Chapter II “Neoplasms”)

may appear suddenly without preceding symptoms, one can conclude that early diagnosis of the disease is crucial to prevent infarction and eventually death.

1.2 Motivation for the Thesis

The significance of the assessment of IHD led to the employment of a variety of techniques to assess myocardial perfusion. The reference modality to study coronary arteries, i.e. *catheter-based angiography*, provides limited information with respect to the functional impact of a stenosis on the perfusion of a distal myocardial region [7; 8]. Such limitations can be overcome by nuclear medicine techniques, namely by *Single Photon-Emission Computed Tomography* (SPECT) and by *Photon-Emission Tomography* (PET). Both techniques are well validated and established, but present significant drawbacks, in particular patient exposure to radiation and low spatial resolution [9]. Another means to obtain information on myocardial perfusion is *Myocardial Contrast Echocardiography* [10; 11]. Despite its excellent temporal resolution and the lack of radioactive tracers, shadowing artifacts have compromised the image quality, rendering the technique problematic in a clinical setting.

Considering the above, *Magnetic Resonance Imaging* (MR Imaging or MRI) appears particularly appealing as a technique to assess myocardial perfusion. Due to its noninvasive nature it is preferable over nuclear medicine techniques, while its high spatial resolution and tissue contrast outmatches those of echocardiography. Moreover, the fact that a first-pass myocardial perfusion study can be embedded into a more comprehensive MR protocol to complement exams that assess function, viability and coronary occlusion, renders MRI the modality of choice for the evaluation and therapeutic decision-making in patients with known or suspected IHD.

Several of the issues that MR perfusion imaging has been facing since its introduction almost two decades ago [12; 13] have been addressed in the recent past. However, the low image acquisition speed, an inherent consequence of Fourier imaging, remained a hindrance to the clinical adoption of this technique. The requirement of rapid image acquisition has been dictated by the prerequisites that have to be met in order to acquire diagnostically useful perfusion information, i.e. high spatial and temporal resolution as well as large cardiac coverage, requirements that contradict each other. Image reconstruction methods based primarily on parallel imaging [14] succeeded in partly addressing this issue [15–18]. Nonetheless, the necessity for higher resolution [18] and larger coverage [19–21] without compromising temporal fidelity dictates the development of reconstruction methods that permit higher accelerations in two (2D) and three dimensions (3D).

The following summarizes the motivation for this thesis: The development and application of image reconstruction methods that permit faster acquisitions in 2D and 3D without compromising image quality could have a significant impact on enhancing the diagnostic ability and fostering the clinical adoption of myocardial perfusion MR imaging.

1.3 Contribution of the Thesis

Based on the motivation delineated above, this thesis addresses temporal fidelity issues in 2D myocardial perfusion imaging for higher accelerations by proposing a modification of the *k-t* SENSE reconstruction method. This modification allows for up to 8× undersampled multi-slice 2D acquisitions at the highest spatial resolution reported to this point (1.1×1.1 mm^2), without compromising image quality. The clinical performance of this method was further demonstrated in a study comprising 20 patients. It was shown that the area under the curve (AUC) of the Receiver Operating Characteristic (ROC) analysis for the ability of the perfusion score to detect the presence of coronary artery disease was 0.94.

Furthermore, considering the necessity for larger coverage, this work proposes a technique to reconstruct highly accelerated (10×), high-resolution (2.3×2.3 mm^2) 3D perfusion images. This technique, based on the *k-t* PCA framework, an extension of *k-t* SENSE, and on prior knowledge with respect to the temporal evolution of the contrast bolus passage through the myocardium, can ameliorate issues that emerge when such high acceleration factors are employed and render 3D myocardial perfusion feasible at this resolution.

Finally, this dissertation investigates the effects of acceleration on the values derived from the quantitative analysis of perfusion images. Focus was given on *k-t* SENSE, *k-t* PCA and compartment-based *k-t* PCA and on the acceleration factors that could be employed without compromising image quality and the subsequent quantification. Further aspects of perfusion quantification are also discussed and an *in vivo* case of blood flow quantification in a subject with suspected coronary artery disease is demonstrated.

A more comprehensive discussion of the contribution of this work is presented in Chapter 9. In the following section we present the outline of this treatment.

1.4 Outline

Chapter 2 describes briefly the anatomy and function of the heart and provides details on the pathophysiology of Ischemic Heart Disease (IHD). Terms such as atherosclerosis, coronary stenosis, infarction and viability are explained.

Chapter 3 focuses on methods commonly used to assess myocardial perfusion with Magnetic Resonance Imaging (MRI). First, the clinical requirements are described and then details on commonly employed techniques are provided along with issues to be addressed.

Chapter 4 formulates the general MRI reconstruction problem and provides a solution. Reconstruction equations for methods such as SENSE, *k-t* SENSE and *k-t* PCA are derived and additional considerations with respect to image noise are presented.

In Chapter 5 the first part of the contribution of this thesis is given. A modified *k-t* SENSE reconstruction method for multi-slice 2D perfusion imaging is described and its efficacy and limitations are investigated using computer simulations and *in vivo* experiments. The results of the clinical evaluation of this approach are demonstrated in Chapter 6.

Chapter 7 presents a compartment-based *k-t* PCA reconstruction technique for 3D myocardial perfusion. Purpose of this method is to achieve whole-heart coverage with adequate spatial and temporal resolution without severely compromising temporal fidelity.

In Chapter 8 the effect of *k-t* acceleration on the quantitative analysis of myocardial perfusion is investigated. Focus is given on the error introduced in the calculation of Myocardial Blood Flow due to potential temporal filtering introduced by methods such as *k-t* SENSE and *k-t* PCA.

The thesis is concluded in Chapter 9 with a discussion on the contribution of the work along with an outlook of what could be pursued further in the field of accelerated myocardial perfusion imaging.

CHAPTER 2

ISCHEMIC HEART DISEASE

In this chapter, the pathophysiology of Ischemic Heart Disease (IHD) is described. Previously, a brief overview of the cardiac anatomy and function will provide the necessary medical background to comprehend the mechanism behind IHD.

2.1 Cardiac Anatomy and Function

The heart is a highly sophisticated organ, responsible for supplying blood and oxygen to all parts of the body. It is about the size of a clenched fist, weighs about 400 grams and is shaped like a pear. It is placed obliquely in the chest cavity, posterior to the sternum, between the lungs and superior to the diaphragm.

The heart is divided by the *septum* into two halves, each of which is further divided into an *atrium* and a *ventricle* (Figure 2.1). Four *valves* allow

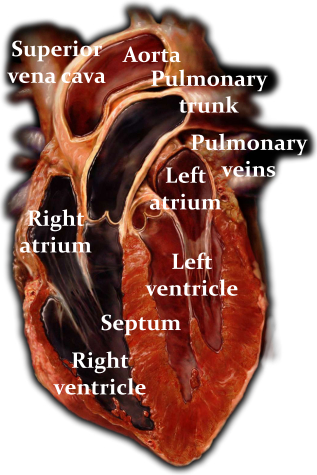

FIGURE 2.1 *Frontal view of an adult heart.*

blood to flow unidirectionally between the chambers into the pulmonary and systemic circulations. Blood is pumped away from the heart through arteries (aorta and pulmonary artery) and returns to the heart through veins (vena cava and pulmonary vein). The cycle of events that occurs as the heart contracts and the blood is pumped to the body is known as the *cardiac cycle* [22].

Cardiac Cycle

There are two phases of the cardiac cycle. In the *diastolic* phase, the heart ventricles are relaxed and the heart fills with blood. In the *systolic* phase, the ventricles contract and pump blood into the arteries.

During diastole, the atria and ventricles are dilated. Blood flows into the right and left atria and then directly through the open valves into the ventricles. In summary:

- Blood flows into the atria (deoxygenated blood in the right atrium, oxygenated blood into the left atrium).

- The atrioventricular valves are open, allowing blood to flow directly into the ventricles.
- Electric impulses initiated by the *sinoatrial node* cause contraction of the atria.
- The atria empty the remaining blood into the ventricles.
- The semilunar valves close, preventing back flow into the atria.

During systole, the ventricles contract, pumping blood into the arteries. The right ventricle sends blood to the lungs via the pulmonary artery, while the left ventricle pumps blood through the aorta to the whole body. Here is a summary of the events during the systolic phase:

- The ventricles contract.
- The atrioventricular valves close and semilunar valves open.
- Deoxygenated blood flows into the lungs through the pulmonary artery where the blood picks up oxygen through a process called diffusion.
- Oxygenated blood flows to all parts of the body through the aorta.

It is important to note that contraction of both atria occurs simultaneously; the same holds true for the contraction of the ventricles. This synchronization is of utmost importance for an effective pump function and can only be achieved with a uniform contraction throughout the periphery of the myocardium.

2.2 Cardiac Ischemia

Prerequisite of good myocardial contractility is sufficient oxygen supply to the cardiac muscle. Oxygenated blood flows into the myocardium through the heart's own nutrient vessels, known as *coronary arteries*, at a rate of 250ml/min (or about 1ml/min per gram), i.e. approximately 5% of normal cardiac output. This rate can increase by a factor of 3.5-5 in the hyperemic myocardium[23–25], a situation which is coped with by dilation of the coronary arteries.

Unfortunately, coronary arteries are particularly vulnerable to a systemic disease of the arterial vessel wall known as *atherosclerosis*. Atherosclerosis induces coronary stenosis, thrombus formation and eventually myocardial infarction and sudden coronary death. In the following sections the cascade of events is described in detail.

Atherosclerosis and Coronary Stenosis

Atherosclerosis is a pathological phenomenon which appears at an early age [26] and develops silently over several decades. It is characterized by an accumulation of lipids in the artery (mainly cholesterol and its esters), which begins in the subendothelial space [27] and results in remodelling of the arterial wall (thickening and hardening of the artery) and plaque formation.

Small atherosclerotic *plaques* are present in most people under the age of 30 years; however, they are small and progress very slowly (phase 1 plaques, type I to III lesions [28]). Presence of risk factors, such as abnormal lipids, smoking, hypertension, diabetes and abdominal obesity [29], may result in establishment of atherosclerosis and development of plaques, not necessarily stenotic, with a high lipid content that are prone to rupture (phase 2 plaques, type IV and Va lesions). The plaques of phase 2 may rupture with predisposition to form mural thrombus –these processes by definition represent phase 3 (type VI lesions) – with a subsequent increase in stenosis, possibly resulting in angina [30].

Thrombosis and Infarction

The same rupture of the plaques of phase 2 may lead to acute coronary *occlusion* (phase 4 plaques, type VI lesions). Occlusion is the result of exposure of material from the core of the plaque (e.g. phospholipids, tissue factor) to the blood, which activates the *clotting* cascade [31; 32].

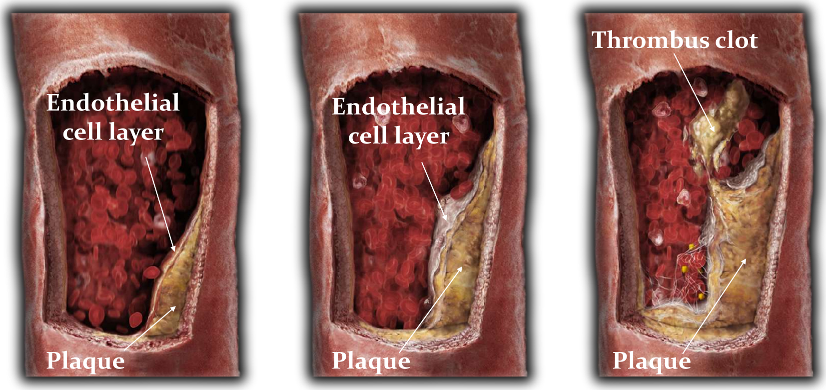

FIGURE 2.2 *Plaque build up and clot development in an artery.*

The mural and occlusive thrombi from plaques of phases 3 and 4, by being organized by connective tissue, may contribute to the progression of the atherosclerotic process represented by severely stenotic or occlusive plaques of phase 5 (type Vb and Vc lesions). Under certain circumstances, the severely stenotic plaques of phase 5 can become complicated and also lead to an occlusive plaque of phase 5 [30].

The resulting *ischemia* (restriction in blood supply), if left untreated for a certain period (20-30 minutes after occlusion), is succeeded by flux of calcium and sodium in myocardial cells, which, in turn, causes intracellular *edema* and finally cell apoptosis.

As systolic wall stress and the resulting oxygen consumption are greater at the *endocardium* (inner layer of the heart) than at the *epicardium* (outer layer of the heart), the infarction will occur earlier and more prominently in subendocardial than in subepicardial tissue. As a consequence, the subendocardial lateral boundaries of a myocardial infarction are established within the first 40 minutes, while the myocardial infarction enlarges in a transmural wave front at a much slower rate over a period of 3-6 hours [33] (see Figure 2.3).

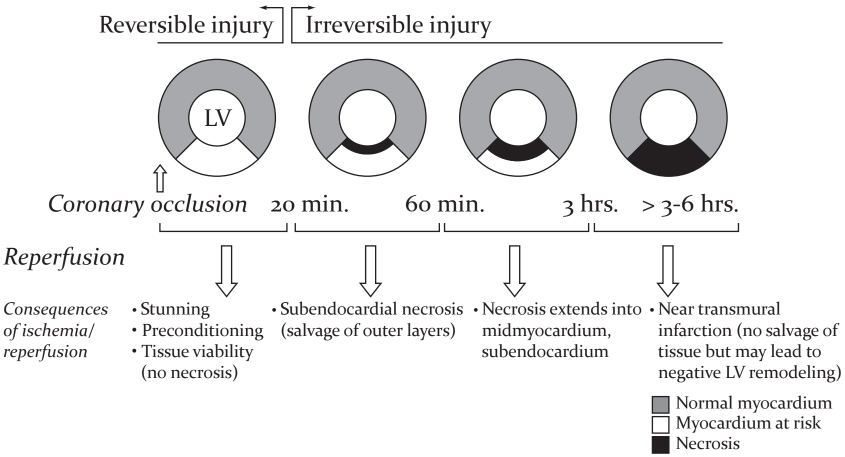

FIGURE 2.3 *Effects of ischemia and reperfusion on myocardial tissue viability and necrosis (Adapted from [34])*

Myocardial Viability

Depending on the severity and the extent of the infarction, areas of the myocardium may present reduced or no contractility. However, these areas are not necessarily necrotic, as they may correspond to regions of potentially reversible damage, which can improve spontaneously or after reestablishment of coronary flow by interventional procedures [35]. It is significant to note at this point, that, in general, the faster the restoration of myocardial perfusion, the smaller the area of the myocardium affected by the infarction. Furthermore, the presence of even a small fraction of perfusion to the infarct bed can significantly delay *necrosis* and limit infarct size [36]. Other factors, such as *collateral circulation*, also contribute to the maintenance of *myocardial viability* [37; 38].

From a clinical point of view, these facts lead to the conclusion that differentiating viable from non-viable myocardium is a particularly significant step during the post-infarct cardiac management. In the past, viability was defined based on functional information: Jeopardized myocardium that manifests improved contractile function after appropriate therapy is considered viable, while myocardium that is persistently dysfunctional is regarded as non-viable [22; 39]. Nowadays, noninvasive discrimination of normal, ischemic and infarcted myocardium can be achieved by using a combined MRI protocol assessing function, perfusion, presence of edema and infarct size. Moreover, this procedure can be performed both in the settings of acute myocardial infarction (AMI) as well as in coronary artery disease (CAD) and suspected CAD patients. The latter is particularly interesting, if we consider that myocardial infarction usually occurs in asymptomatic, apparently healthy people, where the evaluation of atherosclerotic burden is a major clinical challenge [40].

In the following chapter, we focus on methods that can be used to assess *myocardial perfusion*.

CHAPTER 3

PERFUSION IMAGING

During the past years, numerous techniques have been developed for measuring coronary flow and myocardial perfusion. Electromagnetic flowmetry, inert gas washout analysis, radioactive microspheres or radionuclides trapped in the myocardium have been used both in experimental and clinical settings. In clinics, only *radionuclide imaging* has been used routinely, but *myocardial MR perfusion* is drawing increasing attention. Compared to the radionuclide techniques, MR imaging has several advantages, including higher spatial resolution and no radiation exposure.

In this chapter, we focus on perfusion MR imaging, reviewing techniques commonly employed and issues to be addressed.

3.1 First-Pass Imaging

Nowadays, the most commonly used approaches for cardiac perfusion imaging are based on the changes in signal intensity during the first pass of contrast agent through the myocardium. The *contrast agent* is administered intravenously and induces shorter T1 relaxation times of blood signals, resulting in higher signal intensities in T1-weighted imaging sequences. Using such sequences, regions with reduced regional blood flow will appear hypointense compared to well-perfused regions and consequently qualitative assessment of coronary stenosis can be achieved. For quantitative results, *signal intensity-time curves* also referred to as *perfusion curves* have to be extracted and analyzed (see Fig. 3.1). In the following two subsections we elaborate on the effects of contrast agent administration as well as on the influence of vasodilation on normal and ischemic myocardium.

Contrast Agents

Most of the contrast agents clinically approved and used nowadays are extravascular and based on gadolinium. Having seven unpaired electrons, the largest number possible for an atom, gadolinium is one of the most effective paramagnetic agents [41]. In its unbound state it is highly toxic; as such, for biomedical applications, it can only be used in a chelated form, e.g. DTPA.

Paramagnetic contrast agents alter the local magnetic field and thereby enhance the relaxation rate of water protons in close proximity to the agent. Thus, when injected during an MRI exam, they strongly decrease the T1 relaxation times of the surrounding tissue, resulting in higher signal intensities in the perfused regions. The relationship between the contrast concentration and the signal intensity is generally non-linear [42; 43], a fact that has several implications with respect to the pulse sequence that can be employed, in particular when perfusion needs to be quantified.

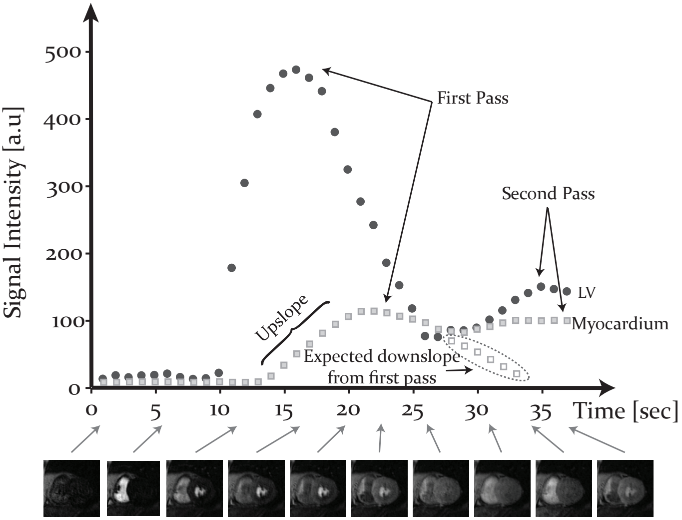

FIGURE 3.1 *Signal intensity-time curves from the myocardium of a healthy volunteer (left to right, a selection of short-axis images). The signal of the myocardium is nulled by a saturation pulse. After enhancement of the right ventricular blood pool, the left ventricular blood pool (LV) and the myocardium are enhanced. The second-pass is visible approximately 20 s later. During this phase, the enhancement in the myocardium is much less pronounced and characterized by the absence of a sharp decline in signal intensity and the absense of a second peak. The latter phenomena are caused by rapid extravasation of the agent into the interstitium, which is responsible for a slow washout (Adapted from [22])*

Vasodilation

Coronary artery stenosis can be hemodynamically significant even in cases of unaltered rest perfusion [44]. Hence, stress testing is generally considered a prerequisite for the assessment of the functional significance of a stenosis. Stress perfusion is most commonly studied using vasodilation induced by administration of adenosine or dipyridamole [45]. Both agents act through stimulation of a certain type of receptors in the microvasculature, known as A2 receptors. Their stimulation results in relaxation of the resistive arterioles, which normally autoregulate

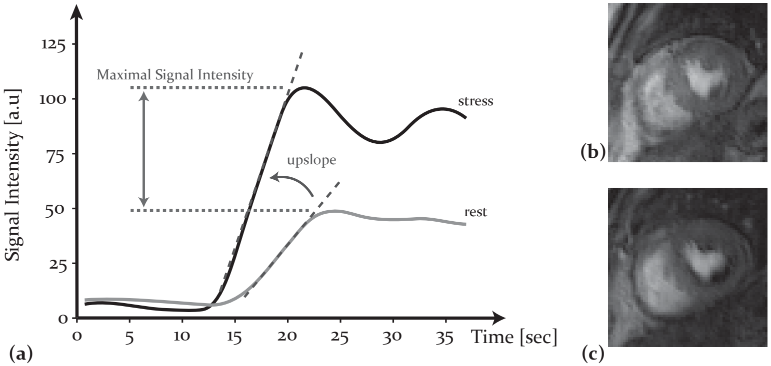

FIGURE 3.2 *(a) Signal intensity curves derived from rest and stress perfusion images. After vasodilation the upslope becomes steeper and the maximal signal intensity increases. (b) Rest and (c) stress perfusion images from a patient with inferolateral defect. Whereas the ischemic region cannot be discriminated in the rest image, it appears hypointense in the stress exam.*

myocardial perfusion relative to coronary perfusion pressure [43]. In normal non-ischemic myocardium, this drop in arteriolar resistance results in a flow increase without changes in myocardial blood volume [46]. In ischemic myocardium during stress, the flow increase is compromised due to the drop of coronary perfusion pressure downstream of the stenosis [46]. This pressure drop results in capillary closure, reduced perfusion and reduced blood volume during hyperemia, which translate into a slower arrival and lower contrast agent concentration in the ischemic myocardium compared to the normal one (Fig. 3.2). As such, ischemic regions appear hypointense on T1-weighted images during hyperemia [43].

3.2 Requirements

Myocardial perfusion scans typically comprise 30–60 images for each slice location. The myocardium appears to be frozen, due to the relatively short acquisition time for each image, while the acquisition is synchronized to the heart cycle by use of the R-wave on the ECG as a trigger signal for the scanner. Moreover, breathing is usually suspended for at least part of the scan to maintain image quality and facilitate image analysis [47].

In order to derive relevant diagnostic information from a first-pass perfusion scan, several requirements have to be fulfilled [48; 49]:

1. **Temporal Resolution** High temporal resolution is needed to resolve the rapid signal intensity changes during the myocardial passage of the contrast agent.

2. **Spatial Resolution** Spatial resolution must be adequate in order to differentiate transmural differences in perfusion.

3. **Coverage** It is necessary to achieve adequate cardiac coverage to assess the extent of the perfusion defect. Three slices is usually the minimum requirement.

4. **Linearity** A linear or quantifiable relationship between signal intensity and contrast agent concentration is necessary for perfusion quantification.

Apart from the knowledge of the relationship between signal intensity and agent concentration, further requirements must be met in order to quantify perfusion, e.g. accurate estimation of the arterial input function. Quantitative perfusion will be discussed in detail later in this chapter.

3.3 Sequences

As stated at the beginning of this chapter, first-pass perfusion imaging is performed by acquiring multiple slices of T1-weighted images that portray perfusion. To provide T1 contrast, inversion recovery (IR) (Fig. 3.3a) was the first contrast preparation to be used [50–53]. With this preparation scheme, images are usually acquired at a time following inversion (TI) which nulls the pre-contrast blood to maximize the contrast. This results in a comparatively long imaging duration and thus limits imaging to a single slice per heartbeat. In addition to this limitation, inversion recovery

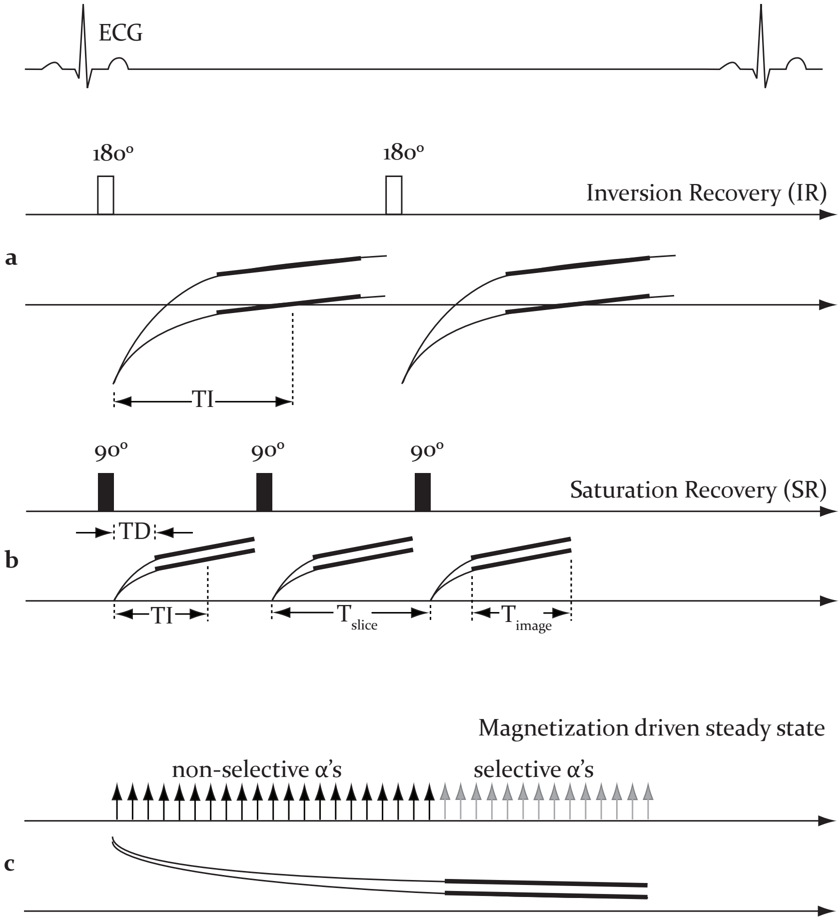

FIGURE 3.3 *Magnetization preparation schemes for T1-weighted myocardial perfusion imaging: (a) inversion recovery (IR), (b) saturation recovery (SR), and (c) magnetization driven steady state (Adapted from [49])*

is sensitive to heart rate variation or missed triggers, which, in turn, result in signal intensity variation due to incomplete magnetization recovery.

The most prevalent method to achieve T1-weighting nowadays is a saturation recovery (SR) preparation (Fig. 3.3b) and may be used in conjunction with various methods for image readout. Using this scheme, T1 weighting is achieved by saturating the magnetization with a non-selective RF pulse prior to the imaging sequence. The advantage of this method is that the contrast is theoretically independent of the magnetization "history", e.g. heart rate and previous acquisitions, and a higher number of slices can be acquired with interleaved acquisitions. Saturation recovery can be sensitive to variations of the transmitted RF field [54; 55], a phenomenon that can be mitigated by using pulse trains, composite RF pulses and B1-insensitive rotation pulses, which provide more uniform saturation at the expense of increased RF heating [43]. More information on the saturation pulses used in perfusion imaging is given in the following subsection.

An alternative magnetization driven steady state preparation approach (Fig. 3.3c) was proposed [56] to achieve a higher degree of linearity (i.e. signal intensity vs. contrast agent concentration) than inversion recovery. In this scheme, the longitudinal magnetization is driven to steady state by a series of RF (alpha) pulses, followed by the readout. Despite achieving linearity with this scheme, the lengthy preparation time limits the acquisition to a single slice per heart beat.

Saturation Recovery Preparation

The performance of the saturation pulse is of particular importance in order to acquire perfusion images of high quality, all the more so, in cases where a semi- or fully-quantitative analysis is to be conducted. For this purpose, the 90° SR preparation has commonly been used due to its insensitivity to arrhythmia or missed ECG triggers. Moreover, it provides improved *Contrast-to-Noise Ratio* (CNR) given an adequate TI [57].

However, static magnetic field (B0) and radio frequency (RF) field (B1) variations within the heart degrade the performance of a single rectangular saturation pulse, especially at high field strengths. The peak-to-peak variation of B0 within the heart has been estimated to be on the order of 70Hz at 1.5T [58] and 130Hz at 3T [59]. Moreover, the magnitude of flip angle variation within the heart for a rectangular 1 ms 90° pulse was calculated to be approximately 10% at 1.5T and 20% at 3T [55; 60]. In order to address those issues, a few RF pulse designs have been proposed that are relatively insensitive to both B0 and B1 variations within the left ventricle. Kim et al. applied an adiabatic B1-insensitive rotation (BIR-4) pulse [54], which achieves uniform saturation of magnetization by sweeping over a broad band of frequencies and phase cycling four adiabatic half-passage (AHP) pulses. As the authors noted [55], the penalties associated with these pulses include longer pulse duration and higher RF power deposition than the corresponding single rectangular pulse. Oesingmann et al. proposed a rectangular RF pulse train [61], which achieves saturation by applying a train of three rectangular 90° pulses, where crusher gradients are cycled to eliminate stimulated echoes. Efficient saturation with low RF power deposition can be further obtained by the use of tailored hard-pulse trains [62], also known as WET pulses [63], or by a hybrid adiabatic-rectangular pulse train [64]. Figure 3.4 presents a comparison of the saturation achieved by a standard 90°, an AHP and a WET pulse.

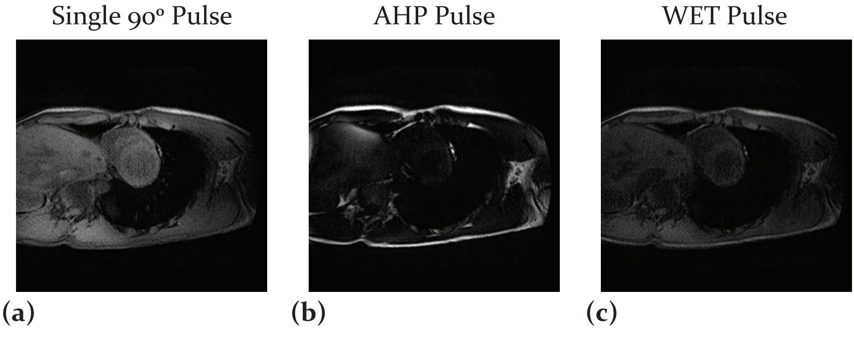

FIGURE 3.4 *Comparison of the saturation achieved by (a) a standard 90° pulse, (b) an AHP pulse and (c) a WET pulse. It is seen that the AHP and WET pulses achieve better saturation than the standard rectangular pulse, with the AHP suppressing the signal more effectively, but in a less homogeneous way compared to the WET pulse.*

Image Readout

After T1 preparation, a multislice image acquisition is performed. As illustrated in Fig. 3.3, different slices have different cardiac phases; each one of them, however, is obtained repeatedly at the same cardiac phase. Images acquired during systole have the advantage of increased myocardial thickness, which facilitates robust analysis, especially when signal intensity-time curves are to be extracted. By contrast, mid- or end-diastole slices have the advantage of reduced motion artifacts.

For sufficient coverage, a minimum of three slices is usually required. The slice thickness is typically 5–10 mm, while the in-plane resolution is usually between 1.5–3.0 mm. Depending on the resolution, field-of-view (FOV) and the use of acceleration (see. Chapter 4), the acquisition of each slice can take 50–250 ms. This involves the employment of an ultra-fast acquisition, usually based on gradient-echo (GRE) [51], gradient echo-planar (GRE-EPI) [65; 66] or balanced steady-state free precession (SSFP) [67] sequences. SSFP provides a higher signal-to-noise ratio compared to GRE, but can suffer from off-resonance effects when going to higher magnetic fields [43]. Until now, there is no clear consensus regarding the sequence of choice for myocardial perfusion imaging, although there is considerable debate and several published comparisons [68–70]. A comprehensive review of imaging sequences for perfusion can be found in [49].

3.4 Quantitative Perfusion

In the majority of clinical studies in the past, the interpretation of perfusion CMR images has been performed qualitatively [71–74]. The necessity to assess the severity of ischemia, however, led to the adoption of *semi-quantitative* [75–78] or *fully quantitative* methods [79–81] to analyze perfusion. Such an analysis is crucial, particularly for cases where a qualitative assessment could be insufficient, such as for patients suffering from multiple-vessel coronary artery disease [47] or for patients with microcirculatory disease (syndrome X) [82].

In the following subsections we elaborate on the most common semi- and fully-quantitative analysis methods. Particular focus is placed on the later due to their increased significance in a clinical setting as well as due to the additional considerations related to their application.

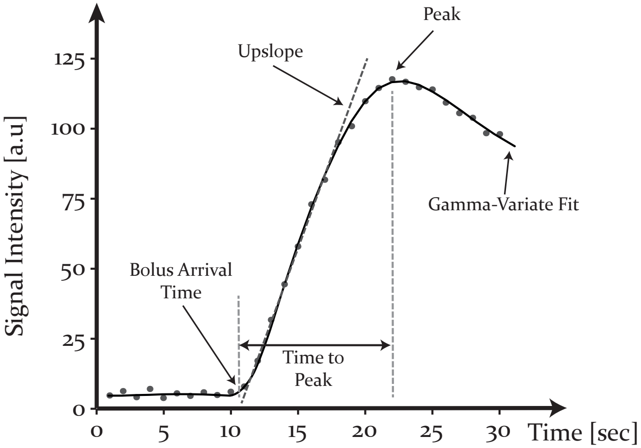

FIGURE 3.5 *A signal intensity-time curves from a myocardial sector in the lateral wall of a healthy volunteer. Each data point (round circle) represents the mean signal intensity in the sector at this time point/ dynamic. The black line represents the best fit of the gamma-variate function to the experimental data. Semi-quantitative perfusion parameters, such as the upslope, the peak signal intensity and the time to peak, are also illustrated.*

Semi-Quantitative Analysis

In order to analyze perfusion in a semi-quantitative manner signal intensity-time curves need to be extracted from regions of the myocardium. The parameters of the curves, such as those depicted in Fig. 3.5, generally do not have well-defined units. As such, an analysis based on these parameters is considered semi-quantitative. The most commonly employed parameters are the following [47]:

1. **Peak Signal Intensity**: The peak value of the signal intensity during the first-pass of the contrast agent, relative to its pre-contrast level.
2. **Upslope**: The rate of change of the signal intensity during the initial ascent of the first pass. The rate of contrast enhancement in the myocardium is often normalized by the rate of contrast enhancement in the LV cavity.
3. **Time to Peak**: The time from the onset of the contrast enhancement, also referred to as *bolus arrival time* (t_{bat}) or foot of the curve, to the peak of the perfusion curve.
4. **Mean Transit Time**: The average time required for a tracer to pass through a region of interest.
5. **Area Under the Curve**: The area under the perfusion curve from the bolus arrival to the peak.

The upslope has been the most widely used parameter in clinical settings [9; 75; 78; 83]. For its robust calculation a smooth fit to the acquired data is required. To obtain such a fit, especially in cases when the recirculation component is not to be taken into consideration, a Gamma-variate function can be employed [84; 85]:

$$g(t) = \begin{cases} 0 & \text{for } t < t_{bat} \\ A \cdot (t - t_{bat})^{a} \cdot e^{-(t-t_{bat})/\tau} & \text{for } t > t_{bat} \end{cases} \tag{3.1}$$

The upslope has often been used to compare the contrast enhancement in different myocardial sectors during an injection. In case a myocardial region suffers from ischemia, the upslope of the curve derived from its sector will be lower compared to that of a healthy region. The upslope can also be used to compare contrast enhancement between rest and stress exams. The ratio of the two upslope values represents an estimate of the

Myocardial Perfusion Reserve, which, in turn, can be used to determine the functional significance of a coronary stenosis (see also the dedicated section later in this chapter). However, this comparison cannot be performed in a straightforward fashion, due to the fact that the upslope will also reflect hemodynamic changes that occur during vasodilation and affect the arterial input. To partly compensate for differences in the arterial input, one can normalize the myocardial upslope values with those from the left ventricular blood pool. A more elegant approach is to perform a fully quantitative analysis of perfusion using the *Central Volume Principle* framework.

Central Volume Principle

The central volume principle, first introduced in [86; 87], provides a theoretical basis to calculate blood flow from perfusion images. This theory assumes a region of interest (ROI) with a single input and a single output. From the principle of mass balance it follows that the amount of tracer in the ROI at any time, $q(t)$, is equal to the difference between the amount of tracer that was supplied to and exited the region. If the variation of tracer concentration at the (arterial) input is denoted by $c_{in}(t)$ and at the output by $c_{out}(t)$, then $q(t)$ can be calculated as follows:

$$q(t) = F \int_0^t \big(c_{in}(\tau) - c_{out}(\tau)\big) d\tau \tag{3.2}$$

where F is the tissue flow rate. The units of measurement are ml/min/g of tissue for the flow F, mmol/ml for the input and output concentrations $c_{in}(t)$ and $c_{out}(t)$, respectively, and mmol/g for the residue $q(t)$. Assuming that the tracer transport within a tissue ROI is a linear and stationary, the output tracer concentration $c_{out}(t)$ is equal to the convolution of $c_{in}(t)$ with the *impulse response transport function* $h(t)$ through the region of interest:

$$c_{out}(t) = \int_0^t h(\tau - t) \cdot c_{in}(\tau) d\tau = h(t) \otimes c_{in}(t) \tag{3.3}$$

The impulse response transport function, $h(t)$, gives the probability that, with an idealized instantaneous input (a Dirac delta function) at $t = 0$, a tracer molecule has left the ROI at time t.

Using Eq. 3.3, Eq. 3.2 can be rewritten as:

$$\begin{aligned} q(t) &= F \cdot \int_0^t \big(1 - h(\tau)\big) \otimes c_{in}(\tau) d\tau \\ &= F \cdot R(t) \otimes c_{in}(t) \\ &= R_F(t) \otimes c_{in}(t) \end{aligned} \tag{3.4}$$

$R(t)$ is the normalized *impulse residue function* and represents the probability that a tracer molecule remains in the ROI up to time t. It is related to the impulse response transport function $h(t)$ by the equation

$$R(t) = 1 - \int_0^t h(\tau) d\tau \tag{3.5}$$

$R_F(t)$ is the *flow-weighted impulse residue function*:

$$R_F(t) = F \cdot R(t) = F \cdot \Big(1 - \int_0^t h(\tau) d\tau\Big) \tag{3.6}$$

Since a tracer molecule cannot instantaneously reach the output after injection, it is $h(t = 0) = 0$. From Eq. 3.6 it follows that:

$$R(t = 0) = F \tag{3.7}$$

i.e. the initial amplitude of the impulse residue function is equal to the flow rate F. This property is independent of the vascular and compartmental structure inside the ROI [47]. Besides, the assumption that there is no flow in and out of the ROI holds, as long as the transport of contrast agent from the capillaries to the interstitial space by diffusion and convection is much slower than by blood flow. This is the case when Gd-DTPA is used as a contrast agent.

It is important to note at this point that the analysis of the perfusion curves using the Central Volume Principle is based on the following assumptions [88]:

1. The MR image intensity is linearly proportional to the regional contrast agent concentration for the dosage used in the exam. If this is not the case, the signal intensity has to be converted to concentration values (see also Section 3.5).

2. The linear relationship between image intensity and contrast concentration is independent of the heart rate with a saturation recovery prepared gradient echo signal [89].

3. The relationship between image intensity and contrast concentration is the same in both the blood pool and the myocardium [90; 91].

4. In the myocardium the linearity assumption holds with a short TR gradient echo sequence with a relatively high flip angle that minimizes the effects of water exchange, and a no-exchange model can be applied [92].

5. The signal time course in the LV blood pool can be used as an input function, as previously validated in PET studies [93].

To summarize, the central volume principle indicates that the blood flow through the myocardium can be determined by deconvolution of the measured tissue residue curve with the arterial input curve. The deconvolution analysis can be performed either by assuming that the impulse residue can be modeled by a known function or in a model-independent fashion. In the following two subsections we elaborate on both methods.

Model-Dependent Analysis

Deconvolution is very sensitive to noise. Despite giving results that fit the observed data, those results can represent physiologically unrealistic impulse responses. As such, the deconvolution operation must be constrained by assuming that the impulse residue function $R(t)$ can be modeled by a known function. $R(t)$ should decay monotonically with time and be smooth. An empirical model often used is the Fermi function:

$$R(t) = \frac{A}{1 + e^{-(t-\omega)/\tau}} \tag{3.8}$$

where A, ω and τ are the model parameters; A is the amplitude of the function, ω is the width of the initial plateau and $1/\tau$ is the decay rate. The Fermi function decays monotonically with the time, is smooth and provides a reasonable approximation to the shape of the impulse response of an intravascular tracer [88; 94].

Despite being widely used, the three model parameters bear no direct relationship to any physiological parameters of the myocardial microcirculation [47]. For a model with adequate realism, parameters can be defined that correspond to vessel volumes, capillary permeability or blood flow. Such models can be employed to quantify MR perfusion imaging [82; 95].

Model-Independent Analysis

The use of models in quantitative perfusion raises questions with respect to which model is most appropriate and what optimization strategy is the best in order to determine model parameters [95]. As such, model-independent methods for constraining the impulse residue function have been proposed in order to determine myocardial blood flow from perfusion curves [96; 97]. The most widely used model-independent method performs deconvolution using Tikhonov regularization with linear constraints and a representation of the impulse residue function in a spline function basis [96].

First, it should be noted that both the input function and the residue curve are measured at equally spaced discrete time points $\boldsymbol{t} = [t_1 \ldots t_n]$. Under the convention that the i-th element q_i of a vector $\boldsymbol{q}$ corresponds to its value at the i-th time point t_i, the discretized representation of Eq. 3.4 is:

$$\boldsymbol{q}(t_i) = q_i \approx \sum_{j=1}^{i} \boldsymbol{c}_{in}(t_i - \tau_j) \cdot \boldsymbol{r}(\tau_j) \cdot \Delta t + \boldsymbol{\epsilon}(t_i) = \sum_{j=1}^{i} A_{ij} r_j + \epsilon_i \tag{3.9}$$

where Δt is the sampling interval and $\boldsymbol{r}$ is a vector representing the discrete form of $R(t)$. The noise in the signal, represented by ϵ_i, is assumed to have a Gaussian distribution with zero mean and standard deviation σ_N. In the rightmost equation, the $n \times n$ convolution matrix A is constructed from the arterial input $i_j = \boldsymbol{c}_{in}(t_j)$ and is real and lower triangular:

$$A = \begin{pmatrix} i_1 & 0 & \dots & 0 \\ i_2 & i_1 & \dots & 0 \\ \vdots & \vdots & \ddots & \vdots \\ i_n & i_{n-1} & \dots & i_1 \end{pmatrix}, \quad A \in \Re^{n \times n} \tag{3.10}$$

In order to estimate the values r_j of the impulse residue function, the error ϵ should be minimized:

$$\hat{\boldsymbol{r}} = \underset{\boldsymbol{r}}{argmin}\big(\|A \cdot \boldsymbol{r} - \boldsymbol{q}\|\big) \tag{3.11}$$

In principle, a simple inversion of A could return an estimate $\hat{\boldsymbol{r}}$ for the impulse residue function, but in the presence of noise the problem is ill-posed and such a solution is unstable. Otherwise stated, a small perturbation of the arterial input values can cause an arbitrarily large perturbation of the values of the impulse residue function. As such, the numerical stability of of the solution needs to be improved.

One way to achieve this is by analyzing the *singular values* of matrix A. The *Singular Value Decomposition* of A is defined as:

$$SVD(A) = U \cdot \Sigma \cdot V^T \tag{3.12}$$

where U and V are orthogonal matrices (i.e. $UU^T = I$ and $VV^T = I$) and Σ is a diagonal matrix containing the singular values σ_i in decreasing order as a function of row index. T indicates matrix transposition. The singular values σ_i decay toward zero at a rate that characterizes the ill-posedness of the inversion of A. The column vectors of U and V, denoted by $\boldsymbol{u}_i$ and $\boldsymbol{v}_i$, respectively, are referred to as singular vectors. As a side-note, it should be mentioned that the ratio of the largest singular value of A to its smallest nonzero singular value σ_s, $\kappa(A) = \sigma_1/\sigma_s$, is the *condition number* of the matrix.

In order to derive the least-squares solution of Eq. 3.11 it should be noted that a unitary matrix preserves length[1]:

$$\begin{aligned}\|A\cdot\boldsymbol{r}-\boldsymbol{q}\| &= U^T\cdot\|A\cdot\boldsymbol{r}-\boldsymbol{q}\|\\ &= \|U^T\cdot A\cdot\boldsymbol{r}-U^T\cdot\boldsymbol{q}\|\\ &= \|\Sigma V^T\boldsymbol{r}-U^T\boldsymbol{q}\|\\ &= \sum_{i=1}^{s}(\sigma_i\boldsymbol{v}_i^T\cdot\boldsymbol{r}-\boldsymbol{u}_i^T\cdot\boldsymbol{q})^2+\sum_{i=s+1}^{p}(\boldsymbol{u}_i^T\cdot\boldsymbol{q})^2\end{aligned} \tag{3.13}$$

The first sum is for the s nonzero singular values σ_i (from a total of n singular values) and consists of non-negative terms. Since the second sum of Eq. 3.13 is independent of $\boldsymbol{r}$:

$$\begin{aligned}\hat{\boldsymbol{r}} &= \underset{\boldsymbol{r}}{argmin}\big(\|A\cdot\boldsymbol{r}-\boldsymbol{q}\|\big)\\ &= \underset{\boldsymbol{r}}{argmin}\Big(\sum_{i=1}^{s}(\sigma_i\boldsymbol{v}_i^T\cdot\boldsymbol{r}-\boldsymbol{u}_i^T\cdot\boldsymbol{q})^2\Big)\\ &= \sum_{i=1}^{s}\Big(\frac{\boldsymbol{u}_i^T\cdot\boldsymbol{q}}{\sigma_i}\cdot\boldsymbol{v}_i\Big)\end{aligned} \tag{3.14}$$

The last sum in Eq. 3.14 may not converge if the singular values σ_i in the denominator decay too rapidly relative to the scalar products of the nominator. In such a case the solution will present oscillations. In order to ameliorate the conditioning of the problem Jerosch-Herold et al. [96] followed a two-step approach: a) they imposed *a priori* continuity and smoothness constraints on the solution by representing $\boldsymbol{r}$ as a sum of piecewise smooth B-splines and then b) they applied Tikhonov regularization.

Assuming that $B_j^{(k)}$ is the jth spline of order k for the knot sequence $\tau_1 \le \tau_2 \cdots \le \tau_{p+k}$, $p+k$ being the number of knots, we can write $\boldsymbol{r}$ as [98; 99]:

$$\boldsymbol{r}(t_i)=\sum_{j=1}^{p}B_j^{(k)}(t_i)\cdot\boldsymbol{\alpha}_j,\ \ \boldsymbol{\alpha}_j\in\Re \tag{3.15}$$

---

[1] Assuming a unitary matrix U and a norm $\|x\|$, it holds: $U\|x\|=\|x\|$

where $\boldsymbol{\alpha}$ is the vector of real-valued B-spline coefficients. The B-spline functions, $B_j^{(k)}$, are positive definite and the jth B-spline $B_j^{(k)}$ is nonzero at a time point t_i only if $\tau_j \leq t_i \leq \tau_{j+k}$. The measured response, $q(t_i)$, can be written as a sum of convolution integrals of B-spline functions with the input function (see Eq. 3.9):

$$\begin{aligned} q(t_i) &= \sum_{j=1}^{N} \alpha_j \int_0^{t_i} B_j^{(k)}(s) \cdot c_{in}(t_i - s) \\ &\approx \sum_{j=1}^{p} \sum_{l=1}^{i-1} \alpha_j B_j^{(k)}(\xi_l) \cdot c_{in}(t_i - \xi_l) \\ &= \sum_{j=1}^{p} D_{i,j} \cdot \alpha_j \end{aligned} \tag{3.16}$$

where ξ is the integration variable and D is a matrix of size $n \times p$, which is calculated by convolution of the input function $c_{in}(t)$ with the B-spline polynomials:

$$D_{i,j} = \int_0^{t_i} B_j^{(k)}(\xi) \cdot c_{in}(t_i - \xi) \cdot d\xi,\ D \in \Re^{n \times p} \tag{3.17}$$

Using this notation, the minimization problem of Eq. 3.14 translates into the following problem:

$$\hat{\boldsymbol{a}} = \underset{\boldsymbol{a}}{argmin}\big(\|D \cdot \boldsymbol{a} - \boldsymbol{q}\|\big),\ \boldsymbol{\alpha} \in \Re^{p} \tag{3.18}$$

where α is the minimization variable. The solution is derived exactly as before (Eq. 3.14):

$$\hat{\boldsymbol{\alpha}} = \sum_{i=1}^{s} \left(\frac{\boldsymbol{w}_i^T \cdot \boldsymbol{q}}{\sigma_i'} \right) \cdot \boldsymbol{z}_i \tag{3.19}$$

The vectors $\boldsymbol{w}$ and $\boldsymbol{z}$ are the singular vectors of matrix D, while σ_i' are its singular values.

To further improve the conditioning of the ill-posed problem, Tikhonov regularization was proposed. By using Tikhonov regularization, one tries to suppress local oscillations of $\boldsymbol{\alpha}$ by additionally trying to minimize its norm.

In other words, a vector $\boldsymbol{\alpha}$ is sought that minimizes both the residual norm of Eq. 3.18 as well as its own norm:

$$\hat{\boldsymbol{\alpha}} = \underset{\boldsymbol{\alpha}}{argmin}\big(\|D \cdot \boldsymbol{\alpha} - \boldsymbol{q}\| + \lambda\|\boldsymbol{\alpha}\|\big),\ \boldsymbol{\alpha} \in \Re^p \tag{3.20}$$

The scalar λ is a weighting factor that is used to adjust the trade-off between the goodness of the fit (first norm) and the smoothness of the solution (second norm). The least-squares solution to this problem is as follows:

$$\boldsymbol{\alpha} = \sum_{i=1}^{s} \Big(\frac{\sigma_i'^2}{\sigma_i'^2 + \lambda^2}\Big)\frac{\boldsymbol{w}_i^T \cdot \boldsymbol{q}}{\sigma_i'}\boldsymbol{z}_i \tag{3.21}$$

The factor in the parenthesis is called filter factor and for $\sigma_i' < \lambda$ it can dampen the contributions that can cause numerical instabilities. The optimal value for λ can be chosen based on the L-curve method [100]. Using the optimal λ along with the coefficients derived from Eq. 3.21 one can derive the values $\boldsymbol{r}(t)$ for the impulse response function by employing Eq. 3.15.

It should be noted at this point that the Tikhonov regularization step can be applied directly to the solution of Eq. 3.18, presented in Eq. 3.14, without the intermediate step of the impulse residue decomposition using B-splines. However, the latter is proposed to further improve the stability of the numerical solution.

The model-independent approach presented here was validated experimentally and was shown to overcome the shortcomings of the model-dependent approaches mentioned before [96].

Myocardial Perfusion Reserve

A commonly used indicator of the functional significance of coronary artery lesions is the ratio of myocardial blood flow during maximal vasodilation divided by the baseline blood flow. This ratio is referred to as *Myocardial Perfusion Reserve* (MPR) and, as several investigators have confirmed [101–103], correlates well with the degree of luminal narrowing in a coronary artery.

Due to the relative complexity of the absolute quantification of flow, most clinical studies in the past have used the ratio of the stress and rest upslope values as an estimate of the MPR [9; 75; 78; 83]. As mentioned in the section about Semi-Quantitative Perfusion Analysis, the myocardial upslopes are usually normalized by the upslope values in the blood pool to address the variations in the arterial input between stress and rest. Nevertheless, the MPR values derived using this method often deviate from the ones measured with other well-established modalities, such as quantitative Positron Emission Tomography. Such results render the derivation of the MPR from absolutely quantified flows a necessity.

As described above, the Central Volume Principle specifies the relationship between the impulse residue function $R(t)$ and the arterial input function $c_{in}(t)$ (see Eq. 3.4):

$$q(t) = \int_0^t R(t-\tau) \cdot c_{in}(\tau) d\tau \tag{3.22}$$

Assuming that $f(\tau, t) = R(t-\tau) \cdot c_{in}(\tau)$, the rate of change of the amount of tracer in the myocardium can be calculated by considering the Leibniz integral rule[2]:

$$\begin{aligned} \frac{dq(t)}{dt} &= \frac{d}{dt} \int_0^t f(\tau, t) d\tau \\ &= \int_0^t \frac{\partial f}{\partial t} d\tau + f(t,t)\frac{dt}{dt} - f(0,t)\frac{d0}{dt} \\ &= f(t,t) + \int_0^t \frac{\partial f}{\partial t} d\tau \\ &= R(t-t)c_{in}(t) + \int_0^t \frac{\partial\big(R(t-\tau)c_{in}(\tau)\big)}{\partial t} d\tau \\ &= R(0)c_{in}(t) + \int_0^t \frac{\partial R(t-\tau)}{\partial t} c_{in}(\tau) d\tau \end{aligned} \tag{3.23}$$

---

[2] The Leibniz integral rule gives a formula for differentiation of a definite integral whose limits are functions of the differential variable: $\frac{\partial}{\partial z} \int_{a(z)}^{b(z)} f(x,z)dx = \int_{a(z)}^{b(z)} \frac{\partial f}{\partial z} dx + f(b(z), z)\frac{\partial b}{\partial z} - f(a(z), z)\frac{\partial a}{\partial z}$

The following equation holds for the partial derivatives of R with respect to t and τ:

$$\frac{\partial R(t-\tau)}{\partial \tau} = -\frac{\partial R(t-\tau)}{\partial t} \tag{3.24}$$

Equation 3.23 using first Eq. 3.24 and then the rule of integration by parts becomes:

$$\begin{aligned}
\frac{dq(t)}{dt} &= R(0)c_{in}(t) - \int_0^t \frac{\partial R(t-\tau)}{\partial \tau} c_{in}(\tau) d\tau \\
&= R(0)c_{in}(t) - \left(\left[R(t-\tau)c_{in}(\tau) \right]_0^t - \int_0^t R(t-\tau) \frac{dc_{in}(\tau)}{d\tau} d\tau \right) \\
&= R(0)c_{in}(t) - R(0)c_{in}(t) + \int_0^t R(t-\tau) \frac{dc_{in}(\tau)}{d\tau} d\tau \\
&= \int_0^t R(t-\tau) \frac{dc_{in}(\tau)}{d\tau} d\tau
\end{aligned} \tag{3.25}$$

The change of signal intensity in the left ventricular blood pool, where the $c_{in}(t)$ is usually calculated from, can be approximated as a constant rate input, i.e. $c_{in}(t) = \beta \cdot t$ [79], in which case Eq. 3.25 becomes:

$$\begin{aligned}
\frac{dq(t)}{dt} &= \int_0^t R(t-\tau) \frac{dc_{in}(\tau)}{d\tau} d\tau \\
&\approx \beta \int_0^t R(t-\tau) d\tau \\
&= \beta \cdot M_0(t)
\end{aligned} \tag{3.26}$$

where $M_0(t)$ is the area under the impulse residue function up to time t. For an intravascular tracer, $R(t)$ can be approximated as a single exponential function that corresponds to the impulse response of a lumped, single-compartment model [104; 105]:

$$R(t) = F \cdot e^{-t \cdot F / V_D} \tag{3.27}$$

$R(t)$ is normalized so that the area under the entire impulse residue equals the dynamic distribution volume, V_D and the amplitude of the impulse response at $t = 0$ equals the tissue blood flow F [86; 87]. As such the area under the impulse residue curve up to time t is:

$$M_0(t) = V_D\big(1 - e^{-t \cdot F/V_D}\big) \tag{3.28}$$

and the rate of change of the tracer concentration is:

$$\begin{aligned} \frac{dq(t)}{dt} &\approx \beta V_D\big(1 - e^{-t \cdot F/V_D}\big) \\ &\approx \beta \cdot t \cdot F \end{aligned} \tag{3.29}$$

The last approximation can be made if the injection is short compared to the transit time, i.e. $t < V_D/F$, in which case the exponential function can be extended to a power series and the first two terms of these series can be taken into consideration.

Different assumptions with respect to the shape of the impulse residue function might introduce different prefactors in Eq. 3.29. As such the following approximate proportionality relationship between the upslope measured at time t relative to the foot of the curve, the upslope of the arterial input β and the myocardial flow F can be derived [96]:

$$\frac{dq(t)}{dt} \propto \beta \cdot t \cdot F \tag{3.30}$$

The correction introduced here was found to improve the calculation of the ratio of the upslopes during stress and rest, in comparison to the case where the myocardial upslopes were normalized only by the upslope of the arterial input.

3.5 Artifacts and Issues

In this section we present artifacts and issues commonly encountered in first-pass perfusion imaging, which need to be acknowledged and addressed in order to correctly interpret and analyze the images. We distinguish artifacts and issues into those that are relevant for the qualitative analysis of perfusion images and those that are more crucial for quantitative perfusion. It should be mentioned though, that artifacts that affect the correct qualitative interpretation of images will also compromise the quantitative analysis. As such, the issues mentioned in the first subsection complement those mentioned in the second when quantitative perfusion is examined.

Qualitative Perfusion

The most prominent artifact encountered in perfusion imaging is the *dark rim artifact*. It consists of a transient dark rim, which is visible on the subendocardial layer of the myocardium and can be confounded with a hypoperfused area. An experience observer can discriminate between a dark rim artifact and an actual perfusion defect by the fact that the former presents a transient behavior, whereas the latter tends to be visible throughout the image series. Occasionally, however, a mild defect can appear hypointense for a short period, due to delayed perfusion of the region, e.g. through collateral circulation, in which case its identification becomes challenging.

Several possible causes have been suggested for the dark rim artifact [106]. It is believed that the artifact is largely produced by Gibbs ringing in the phase encoding direction at the interface between the left-ventricular (LV) blood pool and myocardium. This can be explained by the inability of the Fourier transform to perfectly represent a discontinuity, which results in at least 9% signal variation (overshoot and undershoot) near the edge or interface. The transience of the artifact can be attributed to the variation of the intensity difference between the blood pool and the tissue. The Gibbs ringing interpretation is also consistent with the increased manifestation of the artifact when higher contrast concentrations or higher injection rates are employed. In order to reduce Gibbs ringing one can filter k-space with a window function at the expense, however, of spatial resolution. Another option is to acquire images at higher resolution [18], with the trade-off of increasing scan time.

Other investigators attribute the appearance of the dark rim artifact to magnetic susceptibility, associated with the concentration of Gd-DTPA in the bolus [67; 69], to banding artifacts or oscillations at tissue boundaries due to motion [107] or partial volume effects at the border between the blood pool and the endocardium [49; 106]. Despite those contributions, there is still no unanimity about the exact causes of the artifact.

Apart from the dark rim artifact, other types of artifacts may impede the correct interpretation of myocardial perfusion images. Chemical shifts and N/2 artifacts, for instance, can be problematic for certain types of sequences. In such cases, the incorporation of fat suppression pulses and phase correction reference scans, respectively, could alleviate those issues [43].

When parallel imaging is performed, aliasing artifacts could be introduced due to errors in the estimation of coil sensitivities. Another issue that relates to parallel imaging is the spatially variant noise; attributed to the non-orthogonality of coil encoding it can limit the acceleration of image acquisitions beyond certain undersampling factors [108; 109].

Quantitative Perfusion

As mentioned before, the issues that have an effect upon the images and their qualitative analysis also influence quantitative perfusion. For instance, the dark rim artifact could result in a signal intensity drop, often below the baseline signal, resulting in an erroneous estimation of blood flow. In the following, we concentrate on issues that primarily concern quantitative perfusion.

First, it should be noted that a typical myocardial perfusion acquisition requires that the patient holds their breath for 30-40 heartbeats. The duration of such a breathhold could be too long for a number of patients, which implies that, in order to acquire signal intensity-time curves, image registration with endo- and epicardial borders is necessary and preferably using an automated algorithm [110; 111].

Quantitative exams assume a perfect magnetization preparation. However, as explained in Section 3.3, the pulses used cannot achieve perfect saturation due to B0 and B1 field inhomogeneities. Consequently, the residual regional magnetization alters the apparent T1 relaxation times and eventually leads to quantification errors. In addition to that, signal intensity variations due to surface coil B1-field inhomogeneities will affect quantitative perfusion and must be compensated for, either by taking the actual coil sensitivity profiles into consideration or by normalizing with proton density weighted images [112; 113].

One of the most significant issues affecting quantification is the nonlinear relationship between signal intensity and contrast concentration due to the exponential recovery following saturation. Ignoring the effect of readout on magnetization, the magnetization recovery is simply described by

$$M = M_0(1 - e^{-TI/T1}) \tag{3.31}$$

with T1 described by

$$\frac{1}{T_1} = \frac{1}{T_{1_0}} + \Gamma \cdot [Gd] \tag{3.32}$$

where T_{1_0}≈850 ms is the precontrast T1 and Γ = 4.5 (s mmol/L)$^{-1}$ is the *relaxivity* of the Gd based contrast agent with concentration [Gd]. The assumption that the magnetization is approximately proportional to the gadolinium concentration [Gd] holds for TI≪T1, in which case exp(-TI/T1)≈(1-TI/T1). However, in most cases and particularly for high concentrations, this assumption does not hold, resulting in effectively saturated signals in the LV blood pool during peak enhancement, therefore to distorted AIFs and underestimated concentrations. To address this issue, several solutions have been proposed. The *dual-bolus* technique uses a low dose of contrast to maintain the linearity of the LV pool signal, succeeded by a higher concentration (∼20×) for myocardial analysis [114; 115]. The *dual-sequence* technique [116; 117], on the other hand, acquires AIF reference images using a low TE and short saturation recovery delay (TD) and then it acquires images with a long TD for myocardial analysis.

In tissue, water exchange between the vascular and interstitial space can alter the relationship between the signal intensity and the contrast agent concentration. In order to be able to assume that all the water in the tissue is equally exposed to the contrast agent (*fast exchange* condition), appropriate parameters for the employed pulse sequence should be chosen [92].

Finally, parallel imaging methods that employ spatiotemporal acceleration [118; 119] are often associated with a special type of artifact, that of *temporal filtering* or *temporal blurring* [18; 120]. This issue is of particular importance and will be addressed extensively in the rest of the thesis.

CHAPTER 4

RECONSTRUCTION

Considering that perfusion imaging requires high spatial and temporal resolutions, it is evident that fast image acquisition and accurate reconstruction are of particular importance when evaluating myocardial perfusion. A concise description of the current image acquisition techniques was given in the previous chapter.

Aim of this chapter is to describe the general reconstruction problem, focussing primarily on parallel imaging, and provide a solution. The mathematical formulation presented in this first section is based on concepts described in [14] and is subsequently used to describe the more specific Sensitivity Encoding (SENSE), *k-t* SENSE and *k-t* PCA reconstructions.

4.1 The Reconstruction Problem

MR imaging aims to reconstruct an image of the excited spin distribution from sampled *k*-space data acquired by one or multiple receiver coils. To keep the mathematical formulation as generic as possible, we assume parallel acquisition using N_c coils and arbitrary sampling. The measured signal value $d_{\kappa,\gamma}$ at *k*-space position $\kappa \in \{1, 2, \ldots, N_\kappa\}$, acquired with coil $\gamma \in \{1, 2, \ldots, N_c\}$, represents the spatial integral of the object-specific signal density function $M(\boldsymbol{r})$ (spin density at position $\boldsymbol{r}$), modulated by an encoding function $enc_{\kappa,\gamma}(\boldsymbol{r})$:

$$d_{\kappa,\gamma}(\boldsymbol{k}) = \int M(\boldsymbol{r}) \cdot enc_{\kappa,\gamma}(\boldsymbol{r}) d\boldsymbol{r} + \eta_{\kappa,\gamma} \tag{4.1}$$

where $\eta_{\kappa,\gamma}$ denotes the complex noise component acquired along with the resonance signal. The noise is considered white with zero-mean Gaussian statistics [108; 121].

The encoding functions can reflect any modulation which the object's magnetization experiences. Typical means of spatial encoding are plane-wave modulation by linear gradient fields, sensitivity encoding by one or multiple coils or RF encoding by RF pulses. Considering only the first two, the encoding functions can be written as:

$$enc_{\kappa,\gamma}(\boldsymbol{r}) = s_\gamma(\boldsymbol{r}) \cdot e^{-j\boldsymbol{k}_\kappa \boldsymbol{r}} \tag{4.2}$$

and the measured signal in Eq. 4.1 becomes:

$$d_{\kappa,\gamma}(\boldsymbol{k}) = \int M(\boldsymbol{r}) s_\gamma(\boldsymbol{r}) e^{-j\boldsymbol{k}_\kappa \boldsymbol{r}} d\boldsymbol{r} + \eta_{\kappa,\gamma} \tag{4.3}$$

where $\boldsymbol{k}_\kappa$ denotes the position in *k*-space at which the value $d_{\kappa,\gamma}$ is taken and $s_\gamma(\boldsymbol{r})$ denotes the complex spatial sensitivity of the receiver coil γ, which it is taken with.

Reconstructing an image from the acquired data amounts to recovering $M(\boldsymbol{\rho})$ from the sampled data $d_{\kappa,\gamma}$ at a finite number of positions $\boldsymbol{r}_i$ [14]. This corresponds to inverting Eq. 4.3. Since Eq. 4.3 is linear in $M(\boldsymbol{r})$, current reconstruction methods generate the image values (pixels) ρ_i as linear combinations of the raw data:

$$\rho_i = \sum_{\kappa,\gamma} F_{i,(\kappa,\gamma)} d_{\kappa,\gamma} \tag{4.4}$$

where F denotes the net reconstruction matrix. Using matrix notation, Eq. 4.4 can be rewritten as

$$\boldsymbol{\rho} = F\boldsymbol{d} \tag{4.5}$$

where $\boldsymbol{\rho}$ and $\boldsymbol{d}$ are vectors containing the image and data values respectively.

Ideally, each image value ρ_i should exclusively represent resonance signal from the corresponding voxel at position $\boldsymbol{r}_i$. However, this is not possible since sampling is limited to a finite portion of the *k*-space. Instead, each image value should at best reflect signal from a small volume around $\boldsymbol{r}_i$ and exhibit only little contamination from a greater distance. By replacing Eq. 4.3 in Eq. 4.4 those imperfections can be expressed as the spatial weighting of the object signal in the image value ρ_i:

$$\begin{aligned}\rho_i &= \int \Big(\sum_{\kappa,\gamma} F_{i,(\kappa,\gamma)} s_\gamma(\boldsymbol{r}) e^{-j\boldsymbol{k}_\kappa \boldsymbol{r}}\Big) M(\boldsymbol{r}) d\boldsymbol{r} + \sum_{\kappa,\gamma} F_{i,(\kappa,\gamma)} \eta_{\kappa,\gamma} \\ &= \int \Big(\sum_{\kappa,\gamma} F_{i,(\kappa,\gamma)} enc_{\kappa,\gamma}(\boldsymbol{r})\Big) M(\boldsymbol{r}) d\boldsymbol{r} + \sum_{\kappa,\gamma} F_{i,(\kappa,\gamma)} \eta_{\kappa,\gamma}\end{aligned} \tag{4.6}$$

The expression in brackets reflects the spatial weighting of the MR signal in the pixel ρ_i and is thus called *Spatial Response Function* (SRF) of the pixel:

$$srf_{\rho_i}(\boldsymbol{r}) = \sum_{\kappa,\gamma} F_{i,(\kappa,\gamma)} enc_{\kappa,\gamma}(\boldsymbol{r}) \tag{4.7}$$

The reconstruction problem can now be viewed as the calculation of the reconstruction matrix such that the $srf_{\rho_i}(\boldsymbol{r})$ approximates a Dirac peak at $\boldsymbol{r}_i$:

$$srf_{\rho_i}(\boldsymbol{r}) \rightarrow \delta(\boldsymbol{r} - \boldsymbol{r_i}) \tag{4.8}$$

In order to optimize the SRF, either globally or on a pixel by pixel basis, we discretize it by sampling the encoding functions along a finite set of positions $\boldsymbol{r}_i$ in space, where $i \in \{1, 2, \ldots, N_\rho\}$, thus yielding the encoding matrix:

$$E_{(\kappa,\gamma),i} = enc_{(\kappa,\gamma)}(\boldsymbol{r}_i) = s_\gamma(\boldsymbol{r}_i)e^{\boldsymbol{i}\boldsymbol{k}_\kappa \boldsymbol{r}_i} \tag{4.9}$$

which has $N_k N_c$ rows and N_ρ columns. After this discretization, the reconstruction problem (Eq. 4.8) can be rewritten in matrix form:

$$SRF = FE \to I \tag{4.10}$$

where I denotes the $N_\rho \times N_\rho$ identity matrix.

The deviation of the SRF from the ideal (represented by the identity matrix) will be referred to as *fidelity term* and can be expressed by using the following Frobenius norm[1]:

$$\Delta = \|FE - I\|_F \tag{4.11}$$

Since the difference between FE and I is an expression of the error or the artifacts of a reconstruction, Δ represents the *artifact power* of this reconstruction. Minimizing Δ or, equivalently, its square, yields the following reconstruction matrix (see Appendix A for mathematical derivation):

$$F = (E^H E)^{-1} E^H \tag{4.12}$$

4.2 Noise Propagation

The reconstruction formula presented in the previous section was derived without additional considerations with respect to the image noise. In this section, a detailed description of the noise in *k*-space is given and its statistics after the application of a linear reconstruction scheme are presented.

The noise term $\eta_{\kappa,\gamma}$ in Eq. 4.1 can be described as an additive, uncorrelated, complex contribution to the pure MR signal. The primary sources of noise in MR are electronic (i.e. Johnson-Nyquist noise [122; 123])

---

[1] The Frobenius norm of an $m \times n$ matrix is defined as the square root of the sum of the absolute squares of its elements: $\|A\|_F = \sqrt{\sum_{i=1}^{m} \sum_{j=1}^{n} |a_{ij}|^2}$

and dielectric and inductive coupling to the conducting solution inside the body, also referred to as sample noise [121; 124]. The former is in most cases neglected. Based on the reciprocal nature of the underlying electrodynamics [125], the noise statistics can be expressed in terms of the electric field generated by the array when driving each individual coil with unit input current at the appropriate Larmor frequency [126].

The noise statistics of a single coil receiver for a certain data point can be described by the noise variance σ_n:

$$\sigma_n^2 = \overline{U_n^2(t)} = 4k_B \cdot BW \cdot T \cdot R \tag{4.13}$$

where U_n is the noise voltage detected by the coil, k_B is Boltzmann's contant, BW is the bandwidth of the noise-voltage detecting system, T is the (absolute) sample temperature and R is the effective resistance of the coil loaded by a sample of volume V. This resistance is given by:

$$R = \int_V \sigma(\boldsymbol{r})|E(\boldsymbol{r})|^2 d\boldsymbol{r}^3 \tag{4.14}$$

where σ denotes the electric conductivity of the sample and E the electric field generated by the receiver, considering the reciprocity principle.

The noise statistics of a multi-coil receiver for a certain data point can be described by the *receiver noise matrix* Ψ_c [108]. The element (l, m) of this matrix reflects the noise correlation between two different channels l and m at the same time and is given by:

$$\psi_c^{(l,m)} = \overline{U_n^{(l)}(t) U_n^{(m)*}(t)} = 4k_B \cdot BW \cdot T \cdot R_m \tag{4.15}$$

where $U_n^{(m)*}$ indicates the complex conjugate of the noise voltage detected by coil m, $U_n^{(m)}$. In Eq. 4.15, R_m refers to the mutual coil resistance, given by:

$$R_m = \int_V \sigma(\boldsymbol{r}) E_l(\boldsymbol{r}) E_m^*(\boldsymbol{r}) d\boldsymbol{r}^3 \tag{4.16}$$

Again, $(^*)$ indicates complex conjugation.

The diagonal elements of the receiver noise matrix Ψ_c refer to the single coil variance, whereas the off-diagonal elements refer to the noise

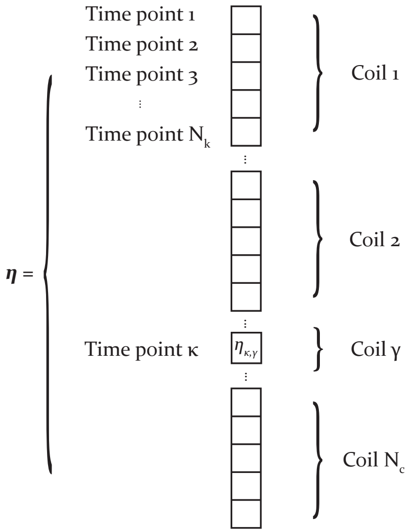

FIGURE 4.1 *The noise data $\eta_{\kappa,\gamma}$ arranged as a vector.*

correlation between different channels at the same time. This matrix can be easily determined experimentally from a reasonably large set of samples reflecting mere noise, e.g. data acquired without any RF excitation before the actual signal acquisition [108; 127]. An important point to note here is that there is no correlation between noise samples detected by the same or different coils at different time points (no auto-correlation):

$$\overline{U_n^{(l)}(t)U_n^{(m)*}(t+\Delta t)} = 0 \tag{4.17}$$

The noise content $\boldsymbol{\eta}$ of an MR image in the k-space can be expressed as a vector whose elements are the complex noise components $\eta_{\kappa,\gamma}$ (Eq. 4.1).

Fig. 4.1 depicts this arrangement. The noise covariance matrix, also known as *sample noise matrix* [108], is:

$$\Psi = \overline{\boldsymbol{\eta}\boldsymbol{\eta}^H} = \begin{pmatrix} \psi_c^{(1,1)} \cdot I_{N_k} & \psi_c^{(1,2)} \cdot I_{N_k} & \dots & \psi_c^{(1,N_c)} \cdot I_{N_k} \\ \psi_c^{(2,1)} \cdot I_{N_k} & \psi_c^{(2,2)} \cdot I_{N_k} & \dots & \psi_c^{(2,N_c)} \cdot I_{N_k} \\ \vdots & \vdots & \ddots & \vdots \\ \psi_c^{(c,1)} \cdot I_{N_k} & \psi_c^{(N_c,2)} \cdot I_{N_k} & \dots & \psi_c^{(N_c,N_c)} \cdot I_{N_k} \end{pmatrix} \tag{4.18}$$

or

$$\Psi = \Psi_c \otimes I_{N_k} \tag{4.19}$$

where Ψ_c denotes the $N_c \times N_c$ receiver noise matrix (Eq. 4.15), I_{N_k} denotes the $N_k \times N_k$ identity matrix and $\otimes$ denotes the Kronecker product. The diagonal form of each block in the sample noise matrix (Fig. 4.2) is due to the zero temporal correlation between the sampled data points as expressed by Eq. 4.17. It can be shown [128] that the matrix Ψ is Hermitian and positive definite.

Since reconstruction, as described in Section 4.1, is a linear mapping, the noise $\boldsymbol{\eta}'$ in the image domain can be expressed in terms of the noise $\boldsymbol{\eta}$ in *k*-space and the reconstruction matrix F:

$$\boldsymbol{\eta}' = F\boldsymbol{\eta} \tag{4.20}$$

The noise statistics in the image domain can be calculated as follows:

$$\begin{aligned} \Psi' &= \overline{\boldsymbol{\eta}'\boldsymbol{\eta}'^H} \\ &= \overline{F\boldsymbol{\eta}\boldsymbol{\eta}^H F^H} \\ &= F\overline{\boldsymbol{\eta}\boldsymbol{\eta}^H} F^H \\ &= F\Psi F^H \end{aligned}$$

Ψ' is referred to as *image noise matrix* [108]. The i-th element on the diagonal of Ψ' ($\psi_{i,i}$) represents the noise variance in the i-th image value, while the off-diagonal elements reflect noise correlation between image values. As it was the case for the noise statistics in *k*-space, noise statistics in image space are zero-mean Gaussian. Moreover, the matrix Ψ', retaining the properties of matrix Ψ under a linear transform F, is Hermitian and positive definite.

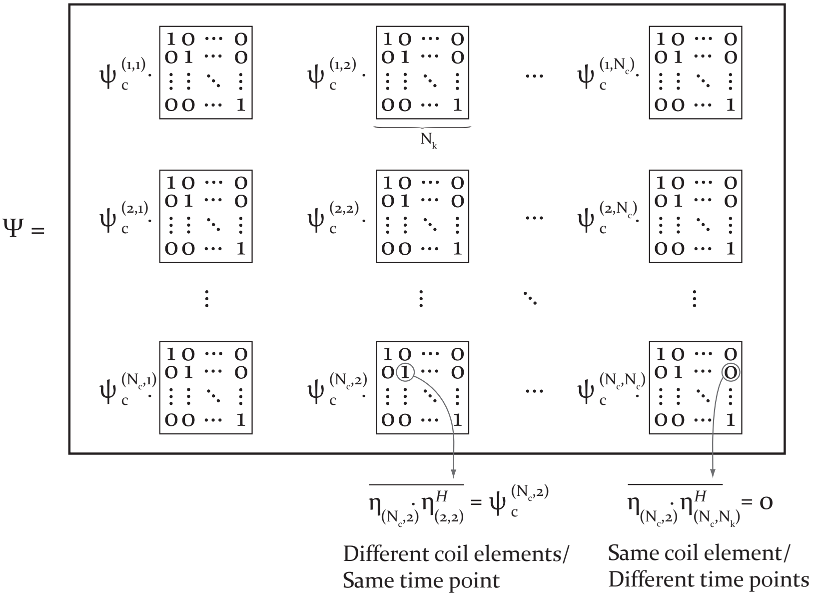

$\overline{\eta_{(N_c,2)}\cdot\eta^H_{(2,2)}} = \psi_c^{(N_c,2)}$

Different coil elements/
Same time point

$\overline{\eta_{(N_c,2)}\cdot\eta^H_{(N_c,N_k)}} = 0$

Same coil element/
Different time points

FIGURE 4.2 *The sample noise matrix represented in block form. Since the temporal correlation between noise samples received by the same or different coil elements is zero (Eq. 4.17), each block is a diagonal matrix.*

4.3 SENSE

If E has full rank and more rows than columns (i.e. more encodings than pixels to resolve), there is an infinite number of solutions that satisfy Eq. 4.12. This implies that some information was redundantly sampled and can be used to optimize the signal-to-noise ratio (SNR) of the reconstructed image. This optimization amounts to finding a reconstruction matrix F that minimizes the sum of all diagonal elements (trace) of the image noise matrix

$$\Lambda^2 = tr(\Psi') = tr(F\Psi F^H) \tag{4.21}$$

under the constraint expressed in Eq. 4.11:

$$FE = I \tag{4.22}$$

In order to cast the optimization into the form of a minimum-norm problem, we eliminate the noise covariance matrix from Eq. 4.21. The basic idea is to create a set of virtual coils by linear combination of the original ones, such that they exhibit unit noise levels and no mutual correlation [128]. Since Ψ is positive definite, its Cholesky decomposition can be calculated:

$$\Psi = L_\Psi L_\Psi^H \tag{4.23}$$

and Eq. 4.21 can be rewritten as:

$$\begin{aligned}\Lambda^2 &= tr(F\Psi F^H) \\ &= tr(FL_\Psi L_\Psi^H F^H) \\ &= tr\big((FL_\Psi)(FL_\Psi)^H\big) \\ &= tr(\tilde{F}\tilde{F}^H)\end{aligned} \tag{4.24}$$

where $\tilde{F} = FL_\Psi$. The constraint can now be expressed as follows:

$$\begin{aligned}FE &= I \\ FL_\Psi L_\Psi^{-1}E &= I \\ \tilde{F}\tilde{E} &= I\end{aligned} \tag{4.25}$$

where $\tilde{E} = L_\Psi^{-1}E$. According to this formulation, the optimal $\tilde{F}$ is the minimum-norm solution of Eq. 4.25 and is equal to the Moore-Penrose pseudoinverse of $\tilde{E}$ [129]:

$$\tilde{F} = \tilde{E}^\dagger \tag{4.26}$$

Since E and thus $\tilde{E}$ have full rank and more rows than columns, the Moore-Penrose pseudoinverse is:

$$\tilde{E}^\dagger = (\tilde{E}^H\tilde{E})^{-1}\tilde{E}^H \tag{4.27}$$

The optimal F is then calculated from Eq. 4.26:

$$\begin{aligned}
FL_\Psi &= \big((L_\Psi^{-1}E)^H(L_\Psi^{-1}E)\big)^{-1}(L_\Psi^{-1}E)^H \\
F &= \big((L_\Psi^{-1}E)^H(L_\Psi^{-1}E)\big)^{-1}(L_\Psi^{-1}E)^H L_\Psi^{-1} \\
F &= \big(E^H(L_\Psi^H)^{-1}L_\Psi^{-1}E\big)^{-1}E^H(L_\Psi^H)^{-1}L_\Psi^{-1} \\
F &= \big(E^H(L_\Psi L_\Psi^H)^{-1}E\big)^{-1}E^H(L_\Psi L_\Psi^H)^{-1} \\
F &= (E^H\Psi^{-1}E)^{-1}E^H\Psi^{-1}
\end{aligned} \tag{4.28}$$

As stated above, this matrix is optimal when the reconstruction problem is overdetermined. If the MR acquisition is performed at the Nyquist rate using several receiver coils, this reconstruction is also referred to as *Roemer reconstruction* [130]. Contrary to that, if the sampling density is reduced by a factor smaller than the number of receiver coils, this scheme is referred to as *SENSE* reconstruction.

4.4 *k-t* SENSE

If prior information is available with respect to the magnetization of certain pixels (e.g. if it is known to be close to or equal to zero), a suitable weighting vector $\boldsymbol{\mu}$ of size $N_\rho \times 1$ can be incorporated in the fidelity term of Eq. 4.11 to improve reconstruction:

$$\Delta = \|(FE - I)\boldsymbol{\mu}\|_F \tag{4.29}$$

Considering that the Frobenius norm of a vector is by definition equal to its 2-norm, taking the square of Eq. 4.29 yields:

$$\begin{aligned}
\|\Delta\|_2^2 &= \|(FE - I)\boldsymbol{\mu}\|_2^2 \\
&= \boldsymbol{\mu}^H(FE - I)^H(FE - I)\boldsymbol{\mu}
\end{aligned} \tag{4.30}$$

$\|\Delta\|_2^2$ is a scalar and therefore it is equal to its trace:

$$\|\Delta\|_2^2 = tr\big(\boldsymbol{\mu}^H(FE - I)^H(FE - I)\boldsymbol{\mu}\big) \tag{4.31}$$

The trace of a matrix product is invariant under cyclic permutations of its elements; as such:

$$\|\Delta\|_2^2 = tr\big((FE-I)\boldsymbol{\mu}\boldsymbol{\mu}^H(FE-I)^H\big) \tag{4.32}$$

Since $\boldsymbol{\mu}$ cannot be known in advance in an MR experiment, the actual error Δ cannot be calculated. However, if an estimate of $\boldsymbol{\mu}$ can be derived, the mean error can be minimized:

$$\begin{aligned}\overline{\|\Delta\|_2^2} &= \overline{tr\big((FE-I)\boldsymbol{\mu}\boldsymbol{\mu}^H(FE-I)^H\big)}\\ &= tr\overline{\big((FE-I)\boldsymbol{\mu}\boldsymbol{\mu}^H(FE-I)^H\big)}\\ &= tr\big((FE-I)\overline{\boldsymbol{\mu}\boldsymbol{\mu}^H}(FE-I)^H\big)\\ &= tr\big((FE-I)\Theta(FE-I)^H\big)\end{aligned} \tag{4.33}$$

where Θ is an estimate of the *signal covariance matrix* .

Considering again the image noise matrix Ψ', the reconstruction problem amounts now to finding a matrix F that minimizes both the trace of Eq. 4.33 and that of the image noise matrix Λ (see Eq. 4.21):

$$F_{opt} = \underset{F}{argmin}(\mathcal{D}) \tag{4.34}$$

where $\mathcal{D}$ is the sum of the two traces:

$$\begin{aligned}\mathcal{D} &= tr\big((FE-I)\Theta(FE-I)^H\big) + \lambda\, tr\big(\lambda F\Psi F^H\big)\\ &= tr\big((FE-I)\Theta(FE-I)^H + \lambda\, F\Psi F^H\big)\end{aligned} \tag{4.35}$$

Here, λ is an arbitrarily chosen scalar, also referred to as *regularization factor*, that, depending on its value, favors either the reconstruction fidelity or the SNR optimization.

In order to calculate the reconstruction matrix F that minimizes $\mathcal{D}$, the Cholesky decomposition of both Θ and Ψ is calculated:

$$\Theta = L_\Theta L_\Theta^H \tag{4.36}$$

and

$$\Psi = L_\Psi L_\Psi^H \tag{4.37}$$

Replacing in Eq. 4.35 yields:

$$\begin{aligned}\mathcal{D} &= tr\big((FE-I)L_\Theta L_\Theta^H (FE-I)^H + \lambda\, FL_\Psi L_\Psi^H F^H\big)\\ &= tr\Big(\big((FE-I)L_\Theta\big)\big((FE-I)L_\Theta\big)^H + \lambda\,\big(FL_\Psi\big)\big(FL_\Psi\big)^H\Big)\end{aligned} \tag{4.38}$$

To facilitate the minimization of $\mathcal{D}$, we make use of the following property of a block matrix that is a concatenation of two matrices A and B with the same number of rows:

$$\begin{aligned}\big(A|B\big)\big(A|B\big)^H &= \big(A|B\big)\begin{pmatrix}A^H\\ B^H\end{pmatrix}\\ &= AA^H + BB^H\end{aligned} \tag{4.39}$$

Eq. 4.38 can thus be written as follows:

$$\mathcal{D} = tr\Big(\big((FE-I)L_\Theta|\sqrt{\lambda}\,FL_\Psi\big)\big((FE-I)L_\Theta|\sqrt{\lambda}\,FL_\Psi\big)^H\Big) \tag{4.40}$$

or equally as the square of a Frobenius norm:

$$\mathcal{D} = \big\|\big((FE-I)L_\Theta|\sqrt{\lambda}\,FL_\Psi\big)\big\|_F^2 \tag{4.41}$$

$\mathcal{D}$ can be expressed as a Frobenius norm of the form $\| FA - B \|_F^2$. The idea is then to find the optimal F as a product of B and the Moore-Penrose pseudoinverse of A, i.e. $F = BA^\dagger$. Employing properties of block matrices:

$$\begin{aligned}\mathcal{D} &= \big\|\big((FEL_\Theta - L_\Theta)|(\sqrt{\lambda}\,FL_\Psi - 0)\big)\big\|_F^2\\ &= \big\|\big((FEL_\Theta|\sqrt{\lambda}\,FL_\Psi) - (L_\Theta|0)\big)\big\|_F^2\\ &= \big\|\big(F\underbrace{(EL_\Theta|\sqrt{\lambda}\,L_\Psi)}_{A} - \underbrace{(L_\Theta|0)}_{B}\big)\big\|_F^2\end{aligned} \tag{4.42}$$

The optimal F is then given as:

$$F = BA^\dagger \tag{4.43}$$

where the $\dagger$ indicates the Moore-Penrose pseudoinverse of A:

$$A^\dagger = A^H(AA^H)^{-1} \tag{4.44}$$

Replacing in Eq. 4.42 we get:

$$
\begin{aligned}
F &= (L_\Theta|0)(EL_\Theta|\sqrt{\lambda}\,L_\Psi)^\dagger \\
&= \big(L_\Theta|0\big)\begin{pmatrix} L_\Theta^H E^H \\ \sqrt{\lambda}\,L_\Psi \end{pmatrix}\left(\big(EL_\Theta|\sqrt{\lambda}\,L_\Psi\big)\begin{pmatrix} L_\Theta^H E^H \\ \sqrt{\lambda}\,L_\Psi^H \end{pmatrix}\right)^{-1} \\
&= (L_\Theta L_\Theta^H E^H + 0)(EL_\Theta L_\Theta^H E^H + \lambda L_\Psi
\end{aligned}
\tag{4.45}
$$

or

$$
F = \Theta E^H (E\Theta E^H + \lambda\Psi)^{-1} \tag{4.46}
$$

In Appendix B the optimal F is derived using a Bayesian approach. There, it is also shown that, in case E is a full-rank matrix, there is a second mathematically equivalent formulation of the solution F, i.e.:

$$
F = \big(E^H(\lambda\Psi)^{-1}E + \Theta^{-1}\big)^{-1} E^H (\lambda\Psi)^{-1} \tag{4.47}
$$

The expression in Eq. 4.46 is more efficient to evaluate if E has more columns than rows (i.e. when the acceleration factor is higher than the number of receivers); conversely the expression in Eq. 4.47 is more efficient to calculate when E has more rows than columns [118].

Although the above mentioned expressions can be used in a SENSE reconstruction problem, where prior knowledge with respect to the signal distribution is available, they have primarily been used in the frame of *k-t* BLAST and *k-t* SENSE [118] to reconstruct undersampled dynamic images that exhibit signal correlations in space and time.

In *k-t* BLAST and *k-t* SENSE acquisition efficiency is increased by sparsely sampling data in the *k-t* space [131]. As a result, the object signals are replicated in the reciprocal *x-f* space, potentially leading to undesirable signal overlap (i.e. aliasing). The *k-t* reconstruction approach resolves the aliasing by using prior knowledge about the expected signal distribution in the *x-f* space obtained from a fully-sampled low-resolution training data set. This data set, expressed here as a $N_\rho \times 1$ vector $\boldsymbol{\rho}_{tr}$, is used to calculate an estimate of the signal covariance matrix in Eq. 4.46:

$$
\Theta = \overline{\boldsymbol{\rho}_{tr}\boldsymbol{\rho}_{tr}^H} \tag{4.48}
$$

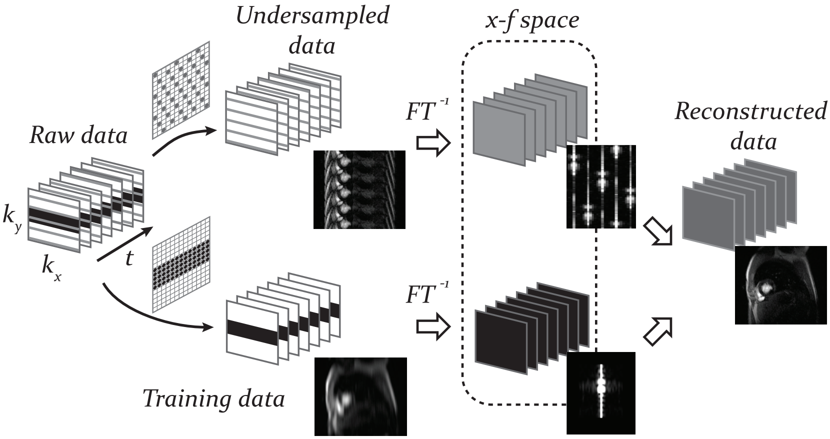

FIGURE 4.3 *Schematic of the k-t SENSE reconstruction.*

The training data can be acquired either in a separate scan or in an interleaved fashion with the undersampled data. In *k-t* SENSE the spatial encoding capabilities of coil arrays also assist in accurately reconstructing the undersampled data. Fig 4.3 gives a schematic of the *k-t* SENSE reconstruction scheme.

As explained in Section 4.2, the noise covariance matrix Ψ can be easily determined experimentally from a reasonably large set of samples $\boldsymbol{\eta}$ reflecting mere noise, e.g. data acquired without any RF excitation before the actual signal acquisition.

$$\Psi = \overline{\boldsymbol{\eta}\boldsymbol{\eta}^H} = \Psi_c \otimes I_{N_k} \tag{4.49}$$

where Ψ_c denotes the $N_c \times N_c$ receiver noise matrix, I_{N_k} the $N_k \times N_k$ identity matrix and $\otimes$ the Kronecker product.

Equation 4.46 solves a linear equation system with $N_k N_\gamma$ equations and N_ρ unknowns:

$$\boldsymbol{\rho} = \Theta E^H (E \Theta E^H + \lambda \Psi)^{-1} \boldsymbol{\rho}_{alias} \tag{4.50}$$

where $\boldsymbol{\rho}_{alias}$ is a $N_k N_c \times 1$ vector containing the undersampled data and $\boldsymbol{\rho}$ is a $N_\rho \times 1$ vector containing the reconstructed data. It is important to note that even if the number of coils is large enough, the equations of this system are not linearly independent, since the hybrid encoding functions (incorporated in E) are not orthogonal. Lack of orthogonality can cause bad conditioning of the inverse problem, which leads to noise enhancement or temporal filtering, depending on the value of the regularization parameter λ. For an acceptable noise enhancement, critically large temporal filtering tends to occur primarily with high acceleration factors [18; 120]. This issue will be considered in depth later in Chapters 5 and 7.

4.5 *k-t* PCA

k-t PCA [132] was recently proposed as an extension of *k-t* BLAST and *k-t* SENSE. It is based on a transformation of the training data from the *x-f* domain to a coefficient domain D. To simplify notation, we will present the inverse transformation from D to *x-f* space, using a matrix A of size $N_\rho \times N_{\rho'}$ whose columns are linearly independent. Such a matrix could be derived from an orthogonal matrix, after cropping a number of its columns (the choice of A will be elaborated on later):

$$\boldsymbol{\rho}_{tr} = A\boldsymbol{w}_{tr} \tag{4.51}$$

The signal covariance matrix Θ can then be transformed as follows:

$$\begin{aligned}\Theta &= \overline{\boldsymbol{\rho}_{tr}\boldsymbol{\rho}_{tr}^H}\\ &= \overline{A\boldsymbol{w}_{tr}(A\boldsymbol{w}_{tr})^H}\\ &= \overline{A\boldsymbol{w}_{tr}\boldsymbol{w}_{tr}^H A^H}\\ &= A\overline{\boldsymbol{w}_{tr}\boldsymbol{w}_{tr}^H}A^H\\ &= A\tilde{\Theta}A^H\end{aligned} \tag{4.52}$$

By replacing Eq. 4.52 in Eq. 4.46, we get:

$$\begin{aligned}\boldsymbol{\rho} &= A\tilde{\Theta}A^H E^H (EA\tilde{\Theta}A^H E^H + \lambda\Psi)^{-1}\boldsymbol{\rho}_{alias}\\ &= A\tilde{\Theta}(EA)^H\big((EA)\tilde{\Theta}(EA)^H + \lambda\Psi\big)^{-1}\boldsymbol{\rho}_{alias}\end{aligned} \tag{4.53}$$

Changing variable:

$$\tilde{E} \equiv EA \tag{4.54}$$

yields:

$$\boldsymbol{\rho} = A\tilde{\Theta}\tilde{E}^H(\tilde{E}\tilde{\Theta}\tilde{E}^H + \lambda\Psi)^{-1}\boldsymbol{\rho_{alias}} \tag{4.55}$$

The most fundamental assumption of *k-t* PCA is that the true *x-f* data $\boldsymbol{\rho}$ are given by:

$$\boldsymbol{\rho} = A\boldsymbol{w} \tag{4.56}$$

where, according to Eq. 4.55, $\boldsymbol{w}$ is the solution of the following inversion problem:

$$\boldsymbol{w} = \tilde{\Theta}\tilde{E}^H(\tilde{E}\tilde{\Theta}\tilde{E}^H + \lambda\Psi)^{-1}\boldsymbol{\rho}_{alias} \tag{4.57}$$

Choice of A

The choice of A can affect reconstruction significantly. Pedersen et al. [132] proposed the application of *Principal Component Analysis* (PCA) along the temporal frequency dimension of the training data in the *x-f* space.

Let's assume that P_{tr} is the training data in the *x-f* space formulated as a $N_x \times N_f$ array, where N_x is the number of elements along all spatial dimensions and N_f is the number of dynamics (size of the temporal dimension). PCA decomposes this matrix, such that:

$$P_{tr} = W_{tr}B \tag{4.58}$$

where W_{tr} and B are matrices of size $N_x \times N_{pc}$ and $N_{pc} \times N_f$ respectively, with N_{pc} being the number of *principal components* (PCs) used in the decomposition.

In order to incorporate this transformation in Eq. 4.51, it should be noted that

$$\boldsymbol{\rho}_{tr} = vec(P_{tr}) \tag{4.59}$$

where the vec operator creates a column vector by stacking the column vectors of P_{tr}. Using Eq. 4.58 and the following property of the vec operator:

$$vec(AB) = (B^T \otimes I)vec(A) \tag{4.60}$$

Eq. 4.59 can be written as:

$$\begin{aligned}\boldsymbol{\rho} &= vec(W_{tr}B) \\ &= (B^T \otimes I_{N_x})vec(W_{tr}) \\ &= (B^T \otimes I_{N_x})\boldsymbol{w}_{tr}\end{aligned} \tag{4.61}$$

Comparing this equation with Eq. 4.51, we see that, in case PCA is applied to the training data, the transformation matrix A will be written as:

$$A = B^T \otimes I_{N_x} \tag{4.62}$$

and it will have a size of $N_\rho \times N_{\rho'}$, where $N_\rho = N_f N_x$ and $N_{\rho'} = N_{pc} N_x$.

By using A to reconstruct $\boldsymbol{\rho}$ (Eq. 4.56), we assume that the PCs along the temporal frequency dimension describe the temporal behavior of both training ($\boldsymbol{\rho}_{tr}$) and final reconstructed data ($\boldsymbol{\rho}$) in the same way.

Advantages of using Principal Component Analysis

In *k-t* SENSE, reconstruction accuracy is dependent on the sparsity of the data in the domain where the unfolding takes place. As explained in [133], improved fidelity can be achieved, if there is as little aliasing as possible, since there will be fewer overlapped signals to separate. From a mathematical perspective there are fewer unknowns to solve for, which improves the conditioning of the inversion problem. On a similar note, if the object replicas in the *x-f* space are far apart, any inaccuracies in the estimated signal covariance become less significant and affect fidelity less.

With higher acceleration factors, the number of unknowns to solve for increases. A worse conditioning of the inversion implies in turn an increase in artifacts in the form of residual aliasing. To remove such artifacts, additional filtering can be applied by regularizing further. The drawback of this approach is that finer image features or certain more dynamic voxels that lie in the higher frequencies of the *x-f* space are attenuated. This is an inherent problem of the L^2 minimization methods, which ”punish” larger (i.e. the square of) differences between the reconstructed and the training signals and therefore favor the larger signals that lie in the lower frequencies. In general, when imaging periodic motion (e.g. cine cardial imaging) the attenuation of the higher temporal frequencies is less severe a problem, since the Fourier transform along the temporal dimension effectively sparsifies the signal within a few harmonics. However, for images that represent a more general motion (e.g. cardiac perfusion images), favoring the lower temporal frequencies over the higher ones results in an erroneous representation of signals at the beginning and at the end of the image sequence and subsequent *temporal filtering*, also referred to as *temporal blurring*.

The application of PCA on the data prior to the reconstruction can alleviate the issues described above. PCA is more efficient than the Fourier transform in sparsifying non-periodic image sequences and is capable of modeling most of the signal variation within a small number of expansion coefficients (PCs). As such, the number of overlapping voxels is reduced and higher temporal frequency components are more accurately reconstructed. From a mathematical point of view, PCA improves the conditioning of the inversion problem by reducing the number of unknowns to solve for without trading-off higher with lower temporal frequencies (which are now both ”mixed” in the temporal bases derived from the PCA).

Using PCA along the temporal frequency dimension has one further implication with respect to the reconstruction fidelity related to the fact that PCA decouples the spatial and temporal dimensions of the data. Using PCA, the training data is decomposed into (a) a spatially invariant term B, containing the basis functions that represent every temporal frequency profile of the training data and (b) a temporally invariant term W_{tr}, containing the weighting coefficients of the PCs for all spatial locations of the training. Exploiting the fact that the training data are acquired at full temporal resolution, the basis functions in B capture most of the temporal behavior present in the data. This fact, along with the assumption that the reconstructed data $\boldsymbol{\rho}$ are linear combinations of those basis functions (Eq. 4.56) and the improved conditioning of the inversion problem, explain why the reconstruction result exhibits high temporal fidelity even at high accelerations.

CHAPTER 5

Perfusion Imaging Using *k-t* SENSE With SENSE Training

As stated in Chapter 3, in first-pass, contrast-enhanced myocardial perfusion imaging, several requirements must be met in order to acquire diagnostically useful perfusion information: 1) high temporal resolution to resolve the rapid signal intensity changes; 2) high spatial resolution; and 3) adequate cardiac coverage to allow accurate detection and quantification of myocardial ischemia [48]. However, as it is generally the case in dynamic MRI, there is a tradeoff between the achievable spatial and temporal resolutions [133]. *k-t* SENSE (see Ch. 4) is one of the methods commonly employed to relax this trade-off and has been successfully applied to perfusion imaging [18; 134].

This chapter is adapted from "Vitanis V., Manka R., Boesiger P. and Kozerke S., *Accelerated Cardiac Perfusion Imaging Using k-t SENSE With SENSE Training. Magnetic Resonance in Medicine* 2009; 62: 955–965"

In this chapter, a modified *k-t* SENSE reconstruction approach is presented, which aims at improving the temporal fidelity of perfusion images at higher accelerations than those achieved with previously introduced methods. Here a set of simulations and experiments that depict the method are shown. In the following chapter the results of a first clinical study that demonstrates its feasibility are presented.

Before giving a detailed description of the method, we cite techniques that addressed this issue in the past by exploiting either coil encoding [15; 16] or coil encoding jointly with spatiotemporal correlations [17; 119; 135; 136].

Using SENSE [15; 108] or Auto-SENSE [16] and two-fold acceleration, improved coverage of the human heart can be achieved without loss in diagnostic performance. Quantitative or semiquantitative analyses using both methods showed good agreement between the perfusion values of accelerated and nonaccelerated imaging, despite the $\sqrt{2}$ signal-to-noise ratio (SNR) loss.

Kellman et al. [17] proposed the combination of two-fold accelerated TSENSE [137] and shot-to-shot interleaving of two slices to increase spatial coverage of the heart without compromising image quality. The $\sqrt{2}$ SNR loss from accelerated imaging is largely compensated for by the increase of the effective TR due to slice interleaving and increased readout flip angles associated with slice interleaving.

Recently, Jung et al. [119] introduced a modified *k-t* GRAPPA [138] to accelerate perfusion imaging in the *k-t* space at a net reduction factor of 3.4. This work demonstrated that improved image quality could be achieved in comparison to conventional GRAPPA by exploiting correlations not only in *k*-space, but also in the higher-dimensional *k-t* space.

Several researchers have investigated the feasibility of accelerating myocardial perfusion imaging using *k-t* SENSE [18; 135; 136]. As shown by Plein at al. [18], a 3.9 net acceleration factor (nominal *k-t* factor = 5, training profiles = 11) could successfully be employed without compromising the diagnostic performance of perfusion images. The shorter acquisition time was used to improve spatial resolution and to reduce dark rim artifacts. A comprehensive consideration of the latter was first presented in [106].

In accordance to previous research regarding *k-t* SENSE [139], Plein et al. [18] state that with increasing acceleration factors the temporal fidelity of the reconstructed data is severely compromised. This, in part, relates to the coarse spatial resolution of the training data, which results in partial volume effects and consequently in underestimation of signal amplitudes of voxels containing tissue interfaces or components of different resonance frequencies due to chemical shift or B0 inhomogeneity. At high acceleration factors, the reconstruction problem in *k-t* SENSE tends to be underdetermined, i.e., the number of unknowns per *x-f* voxel to reconstruct exceeds the effective number of coil encoding functions. As a consequence, reconstruction in a least-squares sense gives rise to signal cross-talk and underestimation of weak signals at high temporal frequencies. An expression of this problem is the fact that myocardial baseline images at higher accelerations show contamination from the contrast passage through the right and left ventricular cavities, in particular at the septal segments, and temporal blurring of signal intensities over time.

To reduce temporal blurring and signal contamination induced by high reduction factors and the coarse spatial resolution of the training data, we propose applying parallel imaging to the training data, thus achieving higher spatial resolution while keeping the same number of acquired profiles. Effects from coil sensitivity variations across the relatively large voxels of the training data are addressed by using the minimum-norm formalism for SENSE [140]. In the following, we describe the methods used to evaluate the performance of the modified *k-t* SENSE relative to the conventional *k-t* SENSE method and subsequently present the results.

5.1 Materials and Methods

The *k-t* SENSE reconstruction method has been thoroughly described in Chapter 4. As explained there, signal correlations from a fully-sampled low-resolution training data set along with the spatial encoding capabilities of a coil array are exploited to resolve the signal overlap occurring due to undersampling data in the *k-t* space.

Briefly, in *k-t* SENSE acquisition efficiency is increased by sparsely sampling data in *k-t* space. As a result, the object signals are replicated in the reciprocal *x-f* space, potentially leading to undesirable signal overlap (i.e., aliasing). Signal correlations from a fully-sampled low-resolution training data set along with the are exploited to resolve the signal overlap in *x-f* space. The equation that describes the reconstruction reads (Eq. 4.50):

$$\boldsymbol{\rho} = \Theta E^H (E \Theta E^H + \lambda \Psi)^{-1} \boldsymbol{\rho}_{alias} \tag{5.1}$$

To obtain higher resolution in the training data the distance between the acquired training profiles in *k*-space was increased, and the resulting spatial aliasing was resolved using frame-by-frame SENSE. Using frame-by-frame SENSE prevents undesired mixing of temporal frequency components in the training data. Reduction factors of two and three were investigated, corresponding to two- and three-fold increased training data resolution.

SENSE Reconstruction

Since the training data are undersampled on a Cartesian grid, the aliasing in the *x*-space in every dynamic frame occurs among small sets of equidistant voxels. The straightforward and computationally efficient way to perform the reconstruction is to individually unfold each of those aliased sets taking into consideration the sensitivities of the receiver coils using the conventional SENSE reconstruction (see [108] and Section 4.3). It is important to note here that conventional SENSE strictly enforces the elimination of aliasing only at voxel centers (weak approach). The negative aspect of this approach is that appreciable residual aliasing may occur when coil sensitivities vary considerably over the extent of a voxel and its significant side lobes. While this is not a problem when scanning at high resolution, it becomes an issue when SENSE is utilized to unfold low-resolution images. This side-lobe aliasing, first encountered in SENSE spectroscopic imaging, can be mitigated by reconstructing using the minimum-norm formalism [140]. When using conventional SENSE, zero-padding the training data to the extent of the high-resolution acquisition matrix can also alleviate the residual aliasing [141].

Minimum-Norm SENSE Reconstruction

To mitigate potential side-lobe aliasing due to the low-resolution acquisition of the training data, the minimum-norm SENSE reconstruction is employed [140]. Briefly, minimum-norm SENSE aims at optimizing the spatial response function of reconstructed voxels as a whole rather than only at voxel centers. The encoding equation of the imaging experiment in its general form reads:

$$\boldsymbol{m} = E\boldsymbol{\rho} \tag{5.2}$$

In Eq. 5.2, $\boldsymbol{m}$ is a vector containing all $N_c N_k$ sampled *k*-space values from all coils (N_c: number of coils, N_k: sampled *k*-space values) while $\boldsymbol{\rho}$ is a vector listing all N_ρ unknown image values for the finite set of pixel positions according to the discretization. E is the $(N_c N_k) \times N_\rho$ encoding matrix, listing the values of the encoding functions [108]:

$$enc_{\gamma,\kappa}(\boldsymbol{\rho}) = e^{i\boldsymbol{k}_\kappa \boldsymbol{\rho}} S_\gamma(\boldsymbol{\rho}) \tag{5.3}$$

For each coil γ, $\boldsymbol{k}_\kappa$ is the *k*-space position and $\boldsymbol{r}$ is the *x*-space position. Note that the matrix representation is not limiting because the discretization can be made arbitrarily fine to achieve any desired level of accuracy.

Image reconstruction amounts to solving Eq. 5.2 for $\boldsymbol{\rho}$. For high discretization, Eq. 5.2 is underdetermined and therefore has an infinite number of solutions. Among those, as proposed in Ref. [140], the minimum-norm solution is chosen:

$$\boldsymbol{\rho} = E^\dagger \boldsymbol{m} \tag{5.4}$$

where the dagger indicates the Moore-Penrose pseudoinverse. Equation 5.4 can be solved using several numerically efficient algorithms [128; 140]. In this work, the system described in Eq. 5.2 was solved iteratively using the conjugate-gradient method [142].

The key difference between the proposed reconstruction and the conventional SENSE is that for minimum-norm reconstruction the encoding matrix E is discretized at a much finer resolution than the nominal image resolution, which is determined by the extent of the sampled k-space. In this work, the size of matrix E was that corresponding to the full matrix of the undersampled *k*-*t* SENSE data.

Numerical Phantom

A numerical phantom was used as a basis for computer simulations. The phantom was generated from an actual perfusion scan and its sensitivity map (six-channel coil array). The reconstruction matrix was 256 x 192 with 24 dynamics. Perfusion curves for the different anatomical regions were extracted from the same scan and intensity variations in the model were simulated accordingly.

Simulations

Two series of simulations were performed based on the phantom described above. The first series investigated the efficacy of the proposed modified *k*-*t* SENSE method as a function of the signal-to-noise ratio (SNR) of the model. For this purpose, uncorrelated Gaussian noise, with varying standard deviation corresponding to eight distinct data sets, was added to the real and imaginary channels of each coil, such that the combined fully sampled image had an SNR between 5 and 100 (eight values) on the septal wall during signal peak. Subsequently, the data sets were decimated to simulate an 8× nominal acceleration with 11 training profiles (5.7× net acceleration). Comparisons were performed between the *k*-*t* SENSE algorithms using the conventionally acquired training and the two-fold or three-fold reduced field-of-view (FOV) training data. In the latter case, both the conventional and the minimum-norm SENSE reconstructions were employed. To allow for quantitative assessment of the reconstruction result, perfusion curves were extracted from several regions of the myocardium and the mean absolute error was calculated having as reference the curves from the corresponding Roemer reconstructed [130] fully sampled data sets. To evaluate noise propagation, noise maps were computed by replacing the measured data with uncorrelated noise in the *k-t* SENSE reconstruction (see Eq. 5.1) while the signal variance estimate Θ and the coil sensitivities in E were pre-computed from the actual object signals [18]. Finally, mean and standard deviation values were calculated for the same myocardial regions as described above, this time on the noise maps.

The second series of simulations aimed at investigating the problem of signal contamination in the septal wall. Since the partial volume effect is pronounced along the phase-encoding direction, one would expect that, if the planning of the exam is such that the septal wall is aligned along the frequency encoding direction, the signal contamination will increase. To verify this hypothesis, the FOV of the numerical phantom was rotated from 0 to 20 degrees (5 data sets) – 0 degrees corresponding to the orientation where the FOV is parallel to the torso and 20 degrees corresponding to the orientation where ventricles and septal wall are along the frequency encoding direction. In order to avoid any aliasing along the phase encoding direction, the FOV was extended in all 5 data sets, so that the whole torso lies in the FOV. The data matrix was 256 x 232 and the net acceleration was 6× (8× *k-t* SENSE with 11 training profiles). The phantom was subsequently decimated and reconstructed as in the first series of simulations and comparisons to the reference were carried out.

It is important to note at this point, that the sensitivity maps used for the SENSE and *k-t* SENSE reconstructions were the ones used to create the numerical phantom. Moreover, the regularization factor (Eq. 5.2) was set equal to 0.5 in all simulations. Initial tests indicated that any value between 0.5 and 2.5 leads to very similar results. As such, and in order to be consistent throughout the experiments, the originally proposed value for the regularization factor [118] was used.

In Vivo Experiments

In vivo experiments comparing *k-t* SENSE reconstructions using conventional training and reconstructions using 2× and 3× SENSE reconstructed training data were carried out in 10 volunteers with no history of cardiac disease (five males, mean age = 27.1 ± 6.9 years). All subjects gave informed consent according to the institutional policy. All experiments were performed on a 3T system (Philips Healthcare, Best, The Netherlands) using a saturation-recovery gradient-echo pulse sequence (TR = 2.6 ms, TE = 0.92 ms, flip angle = 20°, saturation prepulse delay = 150 ms, partial Fourier acquisition, acquisition window = 90 ms, typical FOV = 380 × 340 mm^2, slice thickness = 10 mm, short-axis slices = 2, dynamics = 24, inspiration breathhold). The acquisition matrix was chosen so that the in-plane spatial resolution was constant and equal to 1.52 × 1.48 mm^2. A typical matrix of 250 × 232 with 11 training profiles and an undersampling factor of 8 resulted in six-fold net acceleration.

In each volunteer, three *k-t* SENSE perfusion experiments were performed using the following training data acquisitions: 11 profiles at full FOV, 11 profiles at 2x reduced FOV, and 11 profiles at 3x reduced FOV. Each experiment consisted of an injection of 0.05 mmol/kg Gadolinium (Bayer Schering Pharma AG, Switzerland) at a rate of 5 ml/s, followed by a 20-ml saline flush, with 25-min intervals permitted between the injections to allow for contrast agent washout. The acquisitions in each session were ordered randomly.

The sensitivity maps used both for the SENSE and the *k-t* SENSE reconstructions were estimated using the following autocalibrated method [137; 143]. First, a temporal average of the data in the *k-t* domain is obtained to synthesize a full data set without aliasing. Inverse Fourier transformation is then performed to calculate sensitivity-weighted images, which are then divided by the root-sum-of-squares image to estimate the sensitivity maps. Finally, polynomial fitting can be optionally applied to reduce noise and improve estimation accuracy [108].

Partial Fourier data were reconstructed using homodyne reconstruction [144].

Quantitative Analysis

In the absence of “ground truth” non-accelerated data in the *in vivo* situation, the quantitative analysis was done as follows. Signal intensity curves were extracted from four regions on the myocardium (i.e., septal, inferior, lateral, anterior) during systole, and Fermi-fitting of those perfusion curves was performed [88]. To investigate the temporal fidelity of each reconstruction method, the spectra of the actual and the fitted curves were calculated and subsequently compared with each other. In order to avoid any bias errors due to shifts of the baseline and to concentrate only in the representation of the higher harmonics, the spectrum was normalized to the temporal DC, which was subsequently set to zero for better visualization. The mean and SD values were finally used to quantify the error.

5.2 Results

Numerical Phantom

Figure 5.1 (upper half) illustrates the results from the different training acquisition methods and reconstructions. It can be seen that the 2× (Fig. 5.1b and d) and 3× reduced FOV acquisitions (Fig. 5.1c and e) result in training data of improved resolution. The reconstructions using the minimum-norm formulation reduce the residual folding of the ringing in comparison to the conventional “weak” SENSE reconstruction. In Fig. 5.1 (lower half), *k-t* SENSE reconstruction results using the different training data are given. Residual folding artifacts in the 2× and 3× conventional SENSE training (Fig. 5.1g and h) propagate to the final reconstruction result, particularly in regions with low signal intensity (e.g., lungs). Contrary to that, those artifacts are not visible when the minimum-norm SENSE reconstruction is employed (Fig. 5.1i and j). At the same time, the minimum-norm reconstruction of the training results in increased noise in the final *k-t* SENSE reconstruction relative to the one using conventional SENSE training reconstruction (Fig. 5.1i and j, compared to f).

Training data

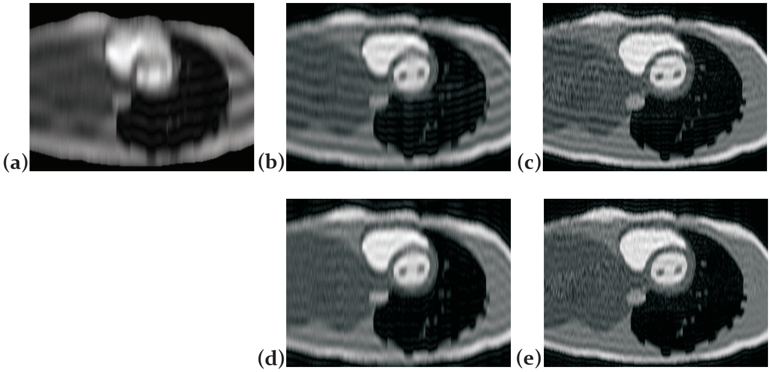

Final *k-t* SENSE result

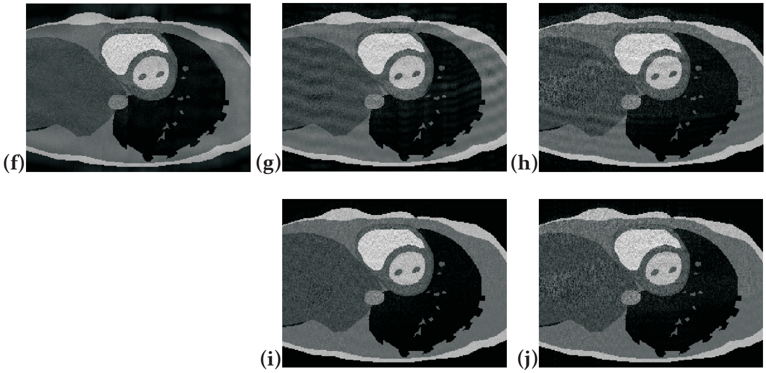

FIGURE 5.1 *Computer simulation showing a time frame before the myocardial upslope of the k-t SENSE training (upper half) and final reconstruction result (lower half of the image) using (a,f) the conventional training acquisition, (b,g) 2× SENSE, (c,h) 3× SENSE, (d,i) 2× minimum-norm SENSE, and (e,j) 3× minimum-norm SENSE training.*

Figure 5.2 depicts the mean absolute error between those perfusion curves and the reference curves as a function of the SNR of the reference data set for different regions of the myocardium (Fig. 5.3).

It can be seen that *k-t* SENSE with SENSE training results in lower errors than the conventional *k-t* SENSE reconstruction above a minimum

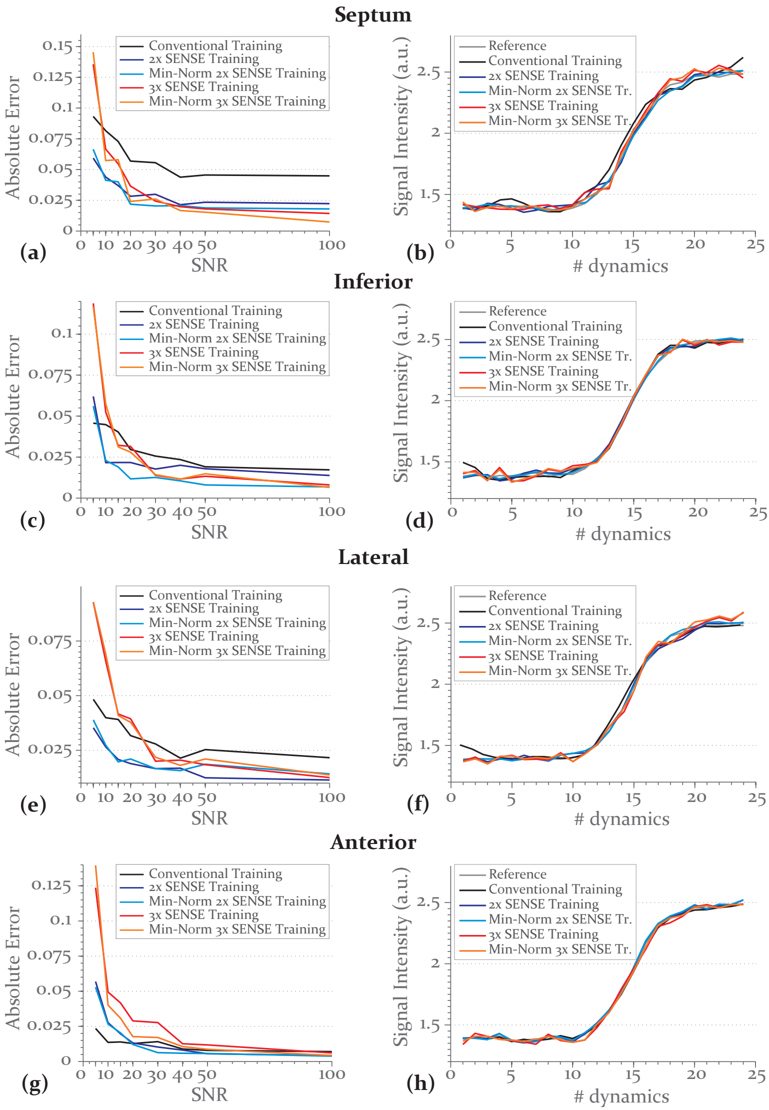

FIGURE 5.2 *Computer simulations. Mean absolute error vs. SNR (left column) and the perfusion curves for a typical SNR of 20 (right column) calculated for four myocardial regions: (a,b) septal, (c,d) inferior, (e,f) lateral, and (g,h) anterior wall, using different training acquisition methods and reconstructions.*

SNR. The cutoff SNR value, below which the conventional reconstruction is better, is approximately 10 for the 2× SENSE training and 15 for the 3× SENSE training (e.g., Fig. 5.2, left column). Two-fold (2×) SENSE training yields better reconstructions than the 3× SENSE training up to an SNR of approximately 50. The advantage of the higher training resolution of the 3× SENSE training is only appreciable when the base SNR is high enough to prevent propagation of the SENSE reconstruction noise through the *k-t* SENSE reconstruction. The minimum-norm SENSE reconstruction results in slightly lower perfusion curve errors than the conventional SENSE. Using SENSE training eliminates the signal contamination in the septal wall (Fig. 5.2b). Despite the slightly increased noise on the perfusion curves, the temporal fidelity achieved using 2× and 3× accelerated SENSE training is better, particularly at the septal region. Figures 5.3a and b illustrate the geometry factor maps (g-maps) [108] of the 2× and 3× SENSE reconstructions of the training data. The overlaid illustration of the myocardium demonstrates the variability of the g-map values depending on the region under consideration.

Figure 5.3c–g illustrates the noise maps for an SNR value of 20. It is seen that the SENSE training reconstructions (Fig. 5.3d–g) result in increased noise in *k-t* SENSE, which becomes accentuated at 3× accelerated SENSE training. It is also observed that the noise maps derived with conventional and 2× SENSE training are dominated by the underlying dynamic structure, i.e., noise amplification is confined to dynamic image regions. With 3× SENSE training, overall noise levels are increased corresponding to the SENSE g-map structure (see also Fig. 5.3b).

Figure 5.4 gives the mean absolute value of the noise maps as a function of the SNR of the reference data set for the regions of the myocardium shown in Fig. 5.3. It is seen that for an SNR below 20 the mean values are slightly lower for the noise maps derived using the conventional training acquisition than for those derived using 2× SENSE, and substantially lower in comparison to those derived using 3× SENSE. On the other hand, for SNR values larger than 30, the mean values of the noise maps using all training reconstruction methods are approximately on the same level. The

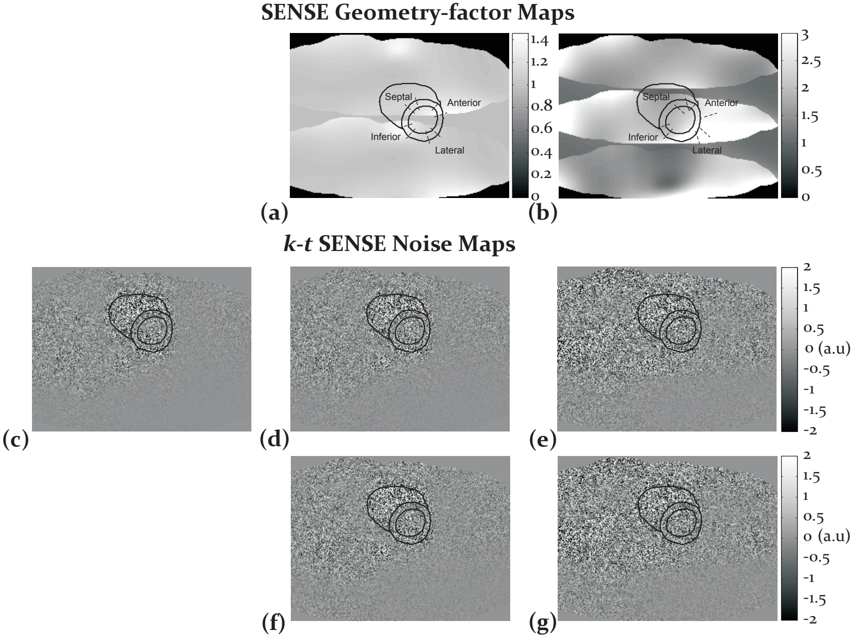

FIGURE 5.3 *Upper row: Geometry maps (g-maps) corresponding to (a) 2× SENSE and (b) 3× SENSE reconstructions. Lower two rows: Real part of the noise maps for the k-t SENSE reconstruction for an SNR value of 20, corresponding to (c) conventional training acquisition, (d) 2× SENSE, (e) 3× SENSE, (f) 2× minimum-norm SENSE, and (g) 3× minimum-norm SENSE training. The position of the myocardium and the 30° sectors where perfusion curves were extracted from are also indicated.*

SD values calculated for all methods and for all regions showed the exact same tendencies and were omitted for brevity.

Figure 5.5 illustrates the mean absolute error between the perfusion curves corresponding to different *k-t* SENSE reconstructions (with conventional and 2×/3× accelerated training) and the reference curves as a function of the rotation angle of the FOV with respect to the torso. It is seen that for the septal wall and using the conventional *k-t* SENSE reconstruction the error tends to increase with the rotation angle, whereas for the other myocardial regions and using the other training

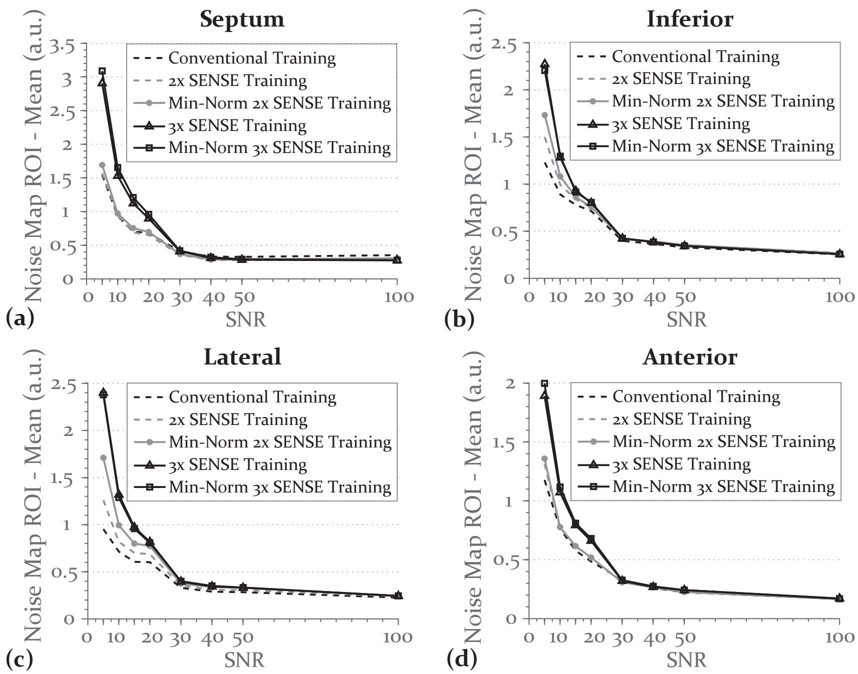

FIGURE 5.4 *Computer simulations: Mean value vs. SNR of the noise maps calculated for four myocardial regions: (a) septal, (b) inferior, (c) lateral, and (d) anterior wall, using different training acquisition methods and reconstructions. The SD values showed the exact same tendencies as the mean values and were omitted for reasons of space.*

reconstruction methods the error does not appear to increase or decrease monotonically as the rotation angle changes.

In Vivo Experiments

Figure 5.6 shows the comparison between the conventional SENSE and minimum-norm SENSE reconstructions for the training (left column) as well as the corresponding final *k-t* SENSE results (right column). Comparing the training reconstructions using the conventional (Fig. 5.6a)

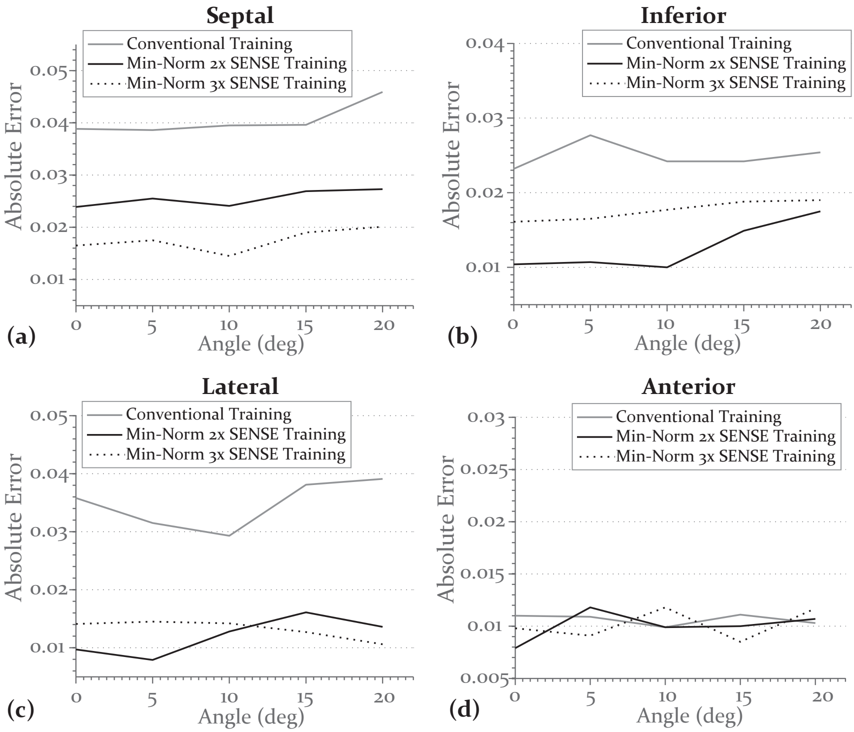

FIGURE 5.5 *Computer simulations. Mean absolute error vs. FOV rotation angle with SNR = 20 calculated for four myocardial regions: (a) septal, (b) inferior, (c) lateral, and (d) anterior wall, using different training acquisition methods and reconstructions.*

and the minimum-norm (Fig. 5.6b) SENSE methods, as well as the corresponding profiles along the myocardium, one notices that the visual differences are only minor. The residual aliasing of the ringing is in both cases diminished, with the exception of the region outside the torso for the conventionally reconstructed training.

The average reconstruction times for three of the *in vivo* datasets with different reconstruction matrices on a PC with an Intel Pentium 4 processor and 2 GB RAM were the following (code written in C): *k-t* SENSE with: 1) conventional training at 30.7 s/slice; 2) 2× SENSE training at 39 s/slice; 3)

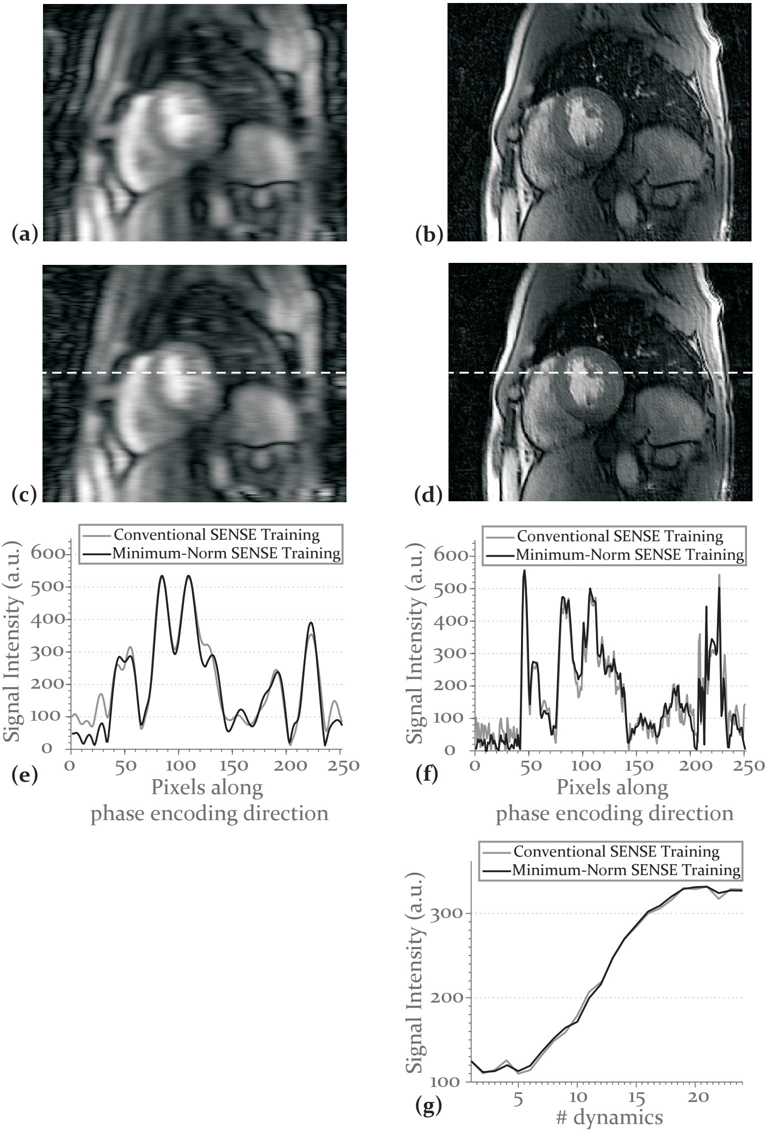

FIGURE 5.6 *In vivo data. A frame of the training and final reconstructed images using conventional 2× SENSE training (a and b, respectively) and 2× minimum-norm SENSE training (c,d, respectively). Signal profiles along the heart (dashed line in (c) and(d)) for the training (e) and final reconstructions (f) using both methods. Perfusion curves extracted for the septal region (g) using both reconstruction methods.*

2× minimum-norm SENSE training at 122.8 s/slice; 4) 3× SENSE training at 39.7 s/slice; and 5) 3× minimum-norm SENSE training at 135.7 s/slice.

Figure 5.7 illustrates actual perfusion curves extracted from the septal wall region in three *in vivo* scans and the fitted Fermi curves (left column). The corresponding processed spectra are shown in the right column. Using the conventional training acquisition (Fig. 5.7a) leads to signal contamination in the reconstruction, to temporal filtering in the form of sinusoidal signal increase during the first dynamics and sinusoidal drop during the last dynamics. These deviations are not seen when using 2× and 3× SENSE training (Fig. 5.7c and e). The corresponding spectra (Fig. 5.7, right column), further reflect the observations with respect to temporal fidelity: using the conventional training acquisition (Fig. 5.7b), one underestimates most temporal frequencies, whereas using the modified acquisition (Fig. 5.7d and f) one achieves higher fidelity. The spectrum of the 3× accelerated training is slightly noisier than that of the 2× accelerated training. The analysis aggregate for all volunteers, presented in Fig. 5.8, further depicts that the proposed method results in lower errors (both mean and SD values), when compared to the conventional *k-t* SENSE. A very interesting observation is that 2× SENSE training does not always yield better reconstructions than 3× SENSE training. The general tendency observed in Fig.5.8 is that the best reconstruction is the one that comes later in the scanning protocol. At this point, it is important to note that the estimated SNR values of the four datasets in which the conventional training acquisition was first employed matched the values used in the computer simulations (mean value = 38.1, range = 33.9–43.3).

5.3 Discussion

When *k-t* SENSE is employed to accelerate perfusion imaging, reconstruction quality is largely dependent on the number of training profiles acquired. In the present work, we have described a method for increasing the spatial resolution of the training data. It has been shown that

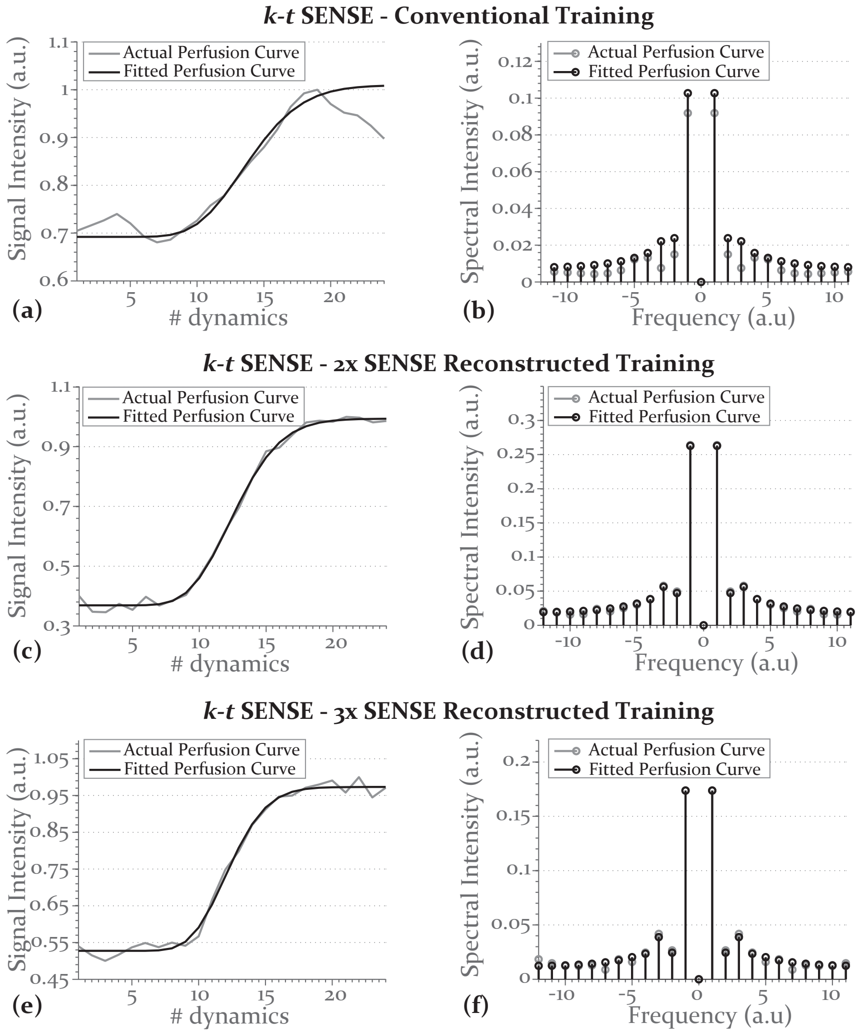

FIGURE 5.7 *In vivo data. Actual and fitted perfusion curves (left column) for a septal region, using k-t SENSE and three different training reconstruction methods: (a) conventionally acquired training, (c) 2× SENSE reconstructed training, and (e) 3× SENSE reconstructed training. Comparison between the corresponding spectra (right column) after normalization to the temporal DC and subsequent nulling of the DC term (b,d,f). The sequence of the experiments was as follows: 1) conventional training acquisition; 2) 3× SENSE accelerated training; and 3) 2× SENSE accelerated training.*

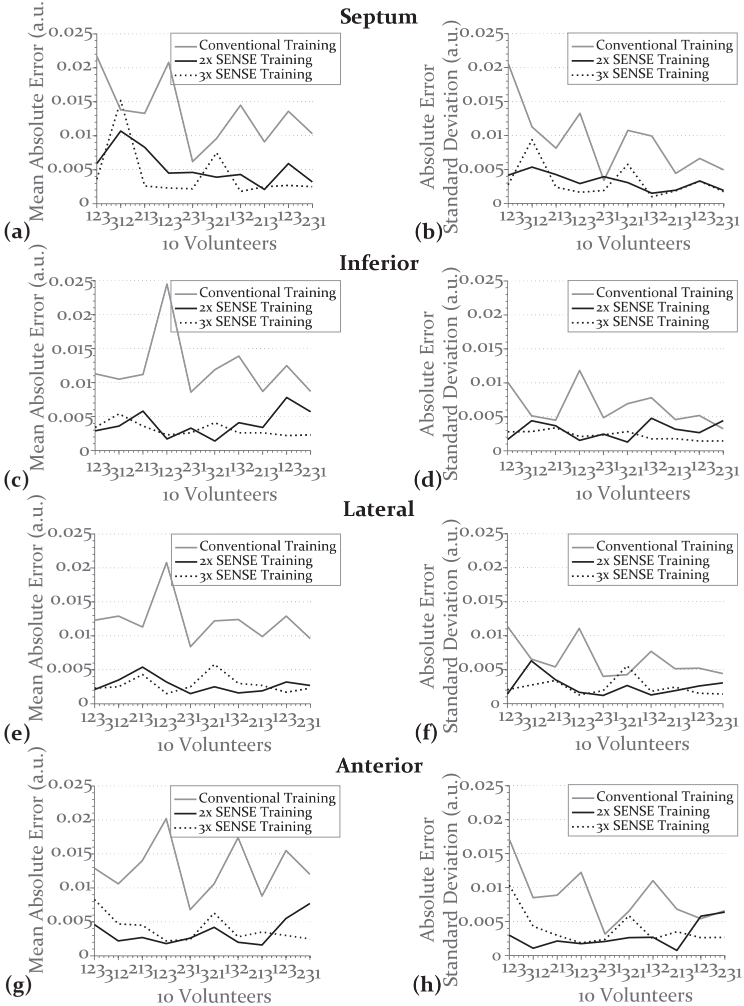

Figure 5.8 *In vivo data. Mean (left column) and SD (right column) of the absolute error between the actual and the fitted spectra for: (a,b) a septal, (c,d) an inferior, (e,f) a lateral, and (g,h) an anterior myocardial region. On the horizontal axis the sequence of the injections is also indicated: 1) conventional training acquisition; 2) 2× SENSE reconstructed acquisition; and 3) 3× SENSE reconstructed acquisition, e.g., 213 indicates that the acquisition of training during the first injection was done using 2× SENSE, the second injection followed with conventional training acquisition (1× SENSE), and the third injection was performed with a 3× SENSE reconstructed training acquisition.*

this method results in improved temporal fidelity without compromising overall acquisition time.

Both computer simulations and *in vivo* experiments assessed that, for an 8× nominal acceleration, the temporal fidelity of the conventional *k-t* SENSE method is not sufficient to correctly depict myocardial perfusion. An overall observation is that the conventional method consistently underestimates high temporal frequencies, resulting in sinusoidal-shaped curves and signal contamination in the septal wall. This temporal low-pass filtering is significantly diminished when training data is acquired at 2× or 3× reduced FOV and subsequently reconstructed using SENSE. Extracted signal intensity vs. time curves and their corresponding spectra confirmed the efficacy of this approach.

Improvement in the resolution of the training data comes at the expense of increased noise. This increased noise, a result of the nonorthogonality of the SENSE, propagates partially through the final *k-t* SENSE reconstruction. Simulations on a numerical phantom indicated that this effect is significant when the SNR of the perfusion image is very low. For SNR values beyond 15 and 20, the proposed method with a 2× and 3× SENSE accelerated training, respectively, results in consistently better reconstructions than the conventional *k-t* SENSE method for all myocardial regions. These SNR limits also agree with the threshold beyond which the SENSE reconstruction noise does not propagate through the *k-t* SENSE reconstruction, as the calculated noise maps illustrated.

Noise amplification using the proposed method is dependent on the myocardial region under consideration. Since the noise in the training after the SENSE reconstruction is spatially varying, the noise in the final reconstructed images will also vary spatially. This general trend in accelerated imaging slightly affected results in computer simulations, but could not be observed in real experiments, where the errors between the different myocardial regions did not deviate noticeably.

The computer simulations also proved the robustness of the proposed method to rotations of the FOV. Despite observing a general trend of increased reconstruction error for the septal region as the phase encoding direction aligns with the septum when the conventional training reconstruction is employed, this observation cannot be generalized to other myocardial regions or training reconstruction methods. There are several reasons that explain the presented erratic error curves in those regions. First, a limitation of the simulation itself should be pointed out: with increasing rotation, the number of points that fold together changes, since now a different number of points correspond to regions with no sensitivity; i.e., regions outside the object. From a mathematical point of view, this results in different conditioning of the *k*-*t* SENSE inversion problem, since a different number of entries in the matrices to be inverted (Eq. 5.1) are set to zero. On the other hand, as seen in Fig. 5.3, different myocardial regions have different g-map values, and the position of those regions changes with rotation of the FOV. As such, the conditioning of the inversion problem changes for each rotation and, with it, the reconstruction error. This can be more of an issue for the proposed SENSE training method, in which the sensitivity maps of the coils are used for both the SENSE and the subsequent *k*-*t* SENSE reconstructions.

The comparison between the minimum-norm SENSE and the conventional SENSE reconstruction with zero-padded *k*-space indicated that the former yields better results only when sharp edges are present in the image (e.g., in the numerical phantom). However, this is not the case in actual *in vivo* experiments, where significant differences can only be observed for regions outside the torso. This is attributed to the fact that the ringing from different structures in the body is cancelled out by the overlap with other structures or ringing signals, something that is not the case outside the torso, where the minimum-norm approach performs better than the conventional SENSE reconstruction. This reasoning agrees with the conclusions of previous work on the topic (16) and suggests that, in clinical environments, where reconstruction speed is of interest, the conventional SENSE method should be used.

The *in vivo* experiments demonstrated that, despite the 25-min interval between the acquisitions and their random order, there is a clear tendency toward reduced error with increasing signal levels due to incomplete contrast washout. This can be explained by the higher signal, and therefore SNR values of the images to be reconstructed, after each subsequent injection. In certain cases, where the 3× accelerated training acquisition was the last in a series of three, this SNR increase counterbalanced the noise increase from the SENSE reconstruction and resulted in error levels similar to the 2× accelerated SENSE. In a clinical setting, where the diagnostically most important stress exam often precedes the rest exam, a 2× accelerated training acquisition is proposed for optimal reconstruction fidelity and reduced noise levels.

Finally, we should note that the usage of the same sensitivities for both reconstruction steps, i.e., first SENSE on the training, then *k-t* SENSE on the undersampled data, should not have further implications per se with respect to the fidelity achieved. This is similar to the conventional *k-t* SENSE case, where the same sensitivities are employed to combine the training with the Roemer [130] reconstruction method and to reconstruct the undersampled data. However, the following consideration should be made: in cases where the calculation of the sensitivity maps is inaccurate, e.g., due to severe motion during the acquisition, folding artifacts occurring after the SENSE reconstruction are expected to affect the final *k-t* SENSE result as well. It should be stated, though, that such issues were not observed in the *in vivo* study performed, even in cases for which the respiratory position was not well held. Further discussion follows in the next chapter where the clinical validation of the method is presented.

CHAPTER 6

CLINICAL VALIDATION OF *K-T* SENSE WITH SENSE TRAINING

The aim of the study presented here was to prospectively determine the feasibility and clinical performance of highly accelerated cardiac perfusion imaging using *k-t* SENSE with SENSE training described in the previous chapter for the detection of CAD using X-ray coronary angiography as the reference standard.

This chapter is adapted from "Manka R., Vitanis V., Boesiger P., Flammer A., Plein S. and Kozerke S., *Clinical Feasibility of Accelerated, High Spatial Resolution Myocardial Perfusion Imaging*. *JACC: Cardiovascular Imaging* 2010; 3(7): 710–717"

6.1 Materials and Methods

Study Population

Twenty patients (16 male, age 60±7 years (mean ± standard deviation), range 45–71) awaiting diagnostic invasive X-ray coronary angiography for evaluation of known or suspected CAD were recruited consecutively between July and November 2008. All patients gave written informed consent and the study was approved by the local ethics review board. Exclusion criteria were contraindications to CMR (mainly incompatible metallic implants, claustrophobia) or to adenosine infusion (asthma, atrioventricular block more severe than grade I), myocardial infarction within 7 days, unstable angina pectoris and NYHA Class IV heart failure. Moreover, patients with arrhythmia and those who had undergone previous coronary artery bypass graft surgery were not considered for study inclusion. Patients were instructed to refrain from substances containing caffeine during 24 hours before the examination. Cardiac medication was not stopped prior to CMR.

Cardiac Magnetic Resonance Imaging

Patients underwent CMR imaging on a 3.0 T clinical MR system (Philips Healthcare, Best, The Netherlands). Patients were placed in supine position and a six-element cardiac phased array coil was used for signal reception. Cardiac synchronization was performed by using four electrodes placed on the hemithorax (vector electrocardiography), and imaging was triggered on the R-wave of the electrocardiogram [145].

After acquisition of standard cine scans for the assessment of left ventricular function, perfusion imaging data were acquired in the short-axis orientation at three different cardiac levels. Adenosine was administered intravenously at a dose of 140 mg/kg/min under continuous heart rate and blood pressure monitoring at 1 min intervals. After 3 min of the adenosine infusion, an intravenous bolus injection of 0.1 mmol/kg Gadobutrolum (Gadovist, Schering, Berlin, Germany) was administered into an antecubital vein on the opposing arm with the use of a power injector (Medrad Spectris Solaris, Medrad, Indianola, PA, USA; injection rate; 5 ml/s followed by a 20 ml saline flush at 5 ml/s).

The CMR perfusion imaging protocol used consisted of a saturation-recovery gradient-echo pulse sequence (TR = 2.7 ms, TE = 0.92 ms, flip angle = 20°, saturation prepulse delay = 150 ms, 75% partial Fourier acquisition with homodyne reconstruction, FOV = 380×280-350 mm^2, slice thickness = 10 mm, number dynamics = 24, end-inspiration breathhold). The acquisition matrix was kept constant (320×256 profiles) resulting in an in-plane resolution of 1.1×1.1-1.4mm2. With 11 training profiles and an undersampling factor of 8 the net acceleration was 6.15. Accordingly, the total number of acquired profiles per slice and heart beat amounted to $256 \times 0.75/6.15 = 32$ resulting in an acquisition window of $32 \times \mathrm{TR} = 87$ ms. As explained in the previous sections of this chapter, in the proposed method, the undersampled data are reconstructed using information from training data. Prior to this image reconstruction step, the training data, which are acquired at 2-fold reduction, are reconstructed using parallel imaging methods to yield a matrix consisting of 2×11 profiles.

Data Analysis

All data were analysed on a post-processing workstation (Viewforum, Philips Healthcare, Best, The Netherlands) by an expert observer with 4 years experience in CMR imaging. The observer was blinded to all clinical information. For assessment of interobserver variability, a second expert (8 years experience in CMR imaging), who was equally blinded to all clinical information, independently repeated the analysis. Image quality with regard to artifacts and blurring was graded on a scale between 0 and 3 (0 = non-diagnostic, 1 = poor, 2 = good, 3 = excellent). Visual perfusion analysis used 16 segments of the American Heart Association (AHA) model for LV assessment (23). Perfusion in a segment was considered abnormal a) if contrast enhancement was reduced in comparison to non-ischemic myocardial segments or b) in cases where a transmural enhancement gradient was seen and the perfusion defect was not located within scar tissue on the corresponding LGE images. Stress perfusion in each segment was scored on a scale from 0 to 3 (0 = normal, 1 = probably normal, 2 = probably abnormal or subendocardial defect, 3 = abnormal or transmural defect). A perfusion score was calculated as the sum of all segmental scores (0-48) for each patient. Separate perfusion scores were calculated for the left anterior descending (LAD), circumflex (LCX), and right coronary artery (RCA) territories according to the AHA segmentation.

In order to assess the value of the high spatial resolution in perfusion imaging, the acquired data were re-sampled to two-fold increased voxel sizes corresponding to four-fold increased voxel volumes by setting to zero all *k*-space samples above a cut-off frequency given by $1/(2\delta\omega)$ where $\delta\omega$ denotes the in-plane voxel widths of the high-resolution data. Additional processing such as Hamming filtering was not applied. Accordingly, in-plane voxel sizes of the resulting low resolution data were $2.2\times2.2\text{-}2.8\text{mm}^2$ and thus comparable to previous clinical trial studies [74]. The low-resolution data were analyzed blinded to the original high resolution data by the two independent observers.

Coronary Angiography

Following the CMR examination, all patients underwent biplane X-ray coronary angiography using a standard technique. Angiograms were analysed by quantitative coronary analysis (QCA) (Xelera 1.2 L4 SP1, Philips Healthcare, Best, The Netherlands) by an independent blinded reviewer. Coronary lesions were analyzed in several projections. The severity of any coronary lesion was evaluated by measuring minimal lumen diameter and per cent diameter stenosis in several angiographic views. The most severe stenosis was recorded. For analysis purposes, only vessels with a reference diameter larger than 2 mm were included. Based on these analyses, patients were classified as having one-, two-, or three-vessel disease. A significant left main stenosis was considered double-vessel disease.

Statistics

Continuous data were expressed as mean ± standard deviation, and comparisons between groups were made by using a two-tailed paired *t* test. No corrections were made for multiple comparisons. Discrete data were expressed as percentages. Categorical data were compared by using the $\chi 2$ test. $p<0.05$ was considered to indicate a significant difference. The diagnostic accuracy of visual analysis to detect coronary stenosis with a diameter of more than 50% with quantitative coronary analysis of x-ray angiograms in vessels with a reference diameter of more than 2 mm was determined with *Receiver Operating Characteristic* (ROC) analysis [146] by using MedCalc® (MedCalc Software, Belgium). The areas under the curves were compared using the method of DeLong et al. [147]. The total perfusion score on a quantitative scale of 0–48 served as the analysis metric. Agreement between observers for the overall perfusion scores was assessed using the method described by Bland and Altman [148].

6.2 Results

Patient Characteristics and Hemodynamic Data

All 20 patients' cohort successfully completed CMR scans and were included in the final analysis.

Table 6.1 summarizes patient characteristics and Table 6.2 presents hemodynamic data. X-ray coronary angiography demonstrated significant coronary artery stenoses (>50% luminal diameter reduction in vessels with >2mm diameter) in 10 patients (50%). Eight patients (40%) had single-vessel and 2 patients (10%) had multi-vessel disease. In terms of anatomical location of coronary artery stenosis, 4 patients (20%) had significant left anterior descenting (LAD) coronary stenosis, 3 patients (15%) had significant left circumflex coronary artery (LCX) stenosis, and 5 patient (25%) had significant right coronary artery stenosis (RCA).

The mean heart rate showed a significant ($p<0.0001$) increase during adenosine infusion. There were no significant changes in systolic ($p=0.07$)

Patient Characteristics		
Age (Years ± SD)	60±7	
Sex, n (%)		
Male	16	(80%)
Female	4	(20%)
Risk Factors and Patient History, n (%)		
Hypertension	12	(60%)
Hypercholesterolemia	13	(65%)
Diabetes mellitus	6	(30%)
Smoking	8	(40%)
Family history of premature CAD	2	(10%)
Suspected CAD	9	(45%)
Known CAD	11	(55%)
Previous PCI	11	(55%)
Previous MI	4	(20%)
Angiography Findings		
No significant CAD§	10	(50%)
One-vessel disease§	8	(40%)
Two-vessel disease§	2	(10%)
Three-vessel disease§	0	(0%)
Left anterior descending§	4	(20%)
Left circumflex coronary artery§	3	(15%)
Right coronary artery§	5	(25%)

SD = standard deviation; CAD=coronary artery disease; PCI=percutaneous coronary intervention; MI=myocardial infarction; §Coronary artery stenosis >50% on quantitative coronary analysis

Table 6.1 *Patient Characteristics*

or diastolic (p=0.81) blood pressure. Most patients (n=17) had minimal side effects (breathlessness, flushing, headache). No serious adverse events occured.

Hemodynamic Data at Rest and Stress		
Hemodynamic Aspect	Rest	Stress
Heart rate (beats/min)	63±11	81±15[§]
Systolic blood pressure (mm Hg)	136±14	134±14
Diastolic blood pressure (mm Hg)	67±9	67±12
Pulse pressure product (beats/min × mm Hg)	8561±1711	10794±2422[§]
Data are means ± standard deviations; [§]$p<0.05$		

TABLE 6.2 *Hemodynamic Data at Rest and Stress*

Diagnostic Accuracy

Figure 6.1 presents *k-t* SENSE with SENSE training perfusion images acquired during adenosine stress in a patient with suspected CAD (upper row) and the corresponding X-ray coronary angiography images (lower row). The CMR images show an inferior perfusion defect in the apical slice and an inferior/inferolateral defect in the equatorial and basal slices. The X-ray images show a subtotal occlusion of the RCA and a high degree stenosis of the left Cx coronary artery with no significant disease in the LAD.

A second case is presented in Fig. 6.2. The perfusion images (upper row) show a circular perfusion defect in the apical slice and an anterior, anteroseptal and inferoseptal defect in the equatorial and basal slices. The X-ray coronary angiography (lower row) gives evidence of a high degree stenosis in the LAD, no significant disease in the Cx and a small, non-dominant RCA.

The overall mean perfusion score was 6.2 (95% CI 3–10). The area under the curve (AUC) of the ROC analysis for the ability of the perfusion score to detect the presence of coronary artery disease (>50%) was 0.94 (95% CI 0.74–0.99) (Fig. 6.3). At a cut-off value of 2, this resulted in a sensitivity and specificity of 90% and 100%, respectively. Using a cut-off value of 1, sensitivity and specificity were 90% and 90%, respectively. AUC of the ROC

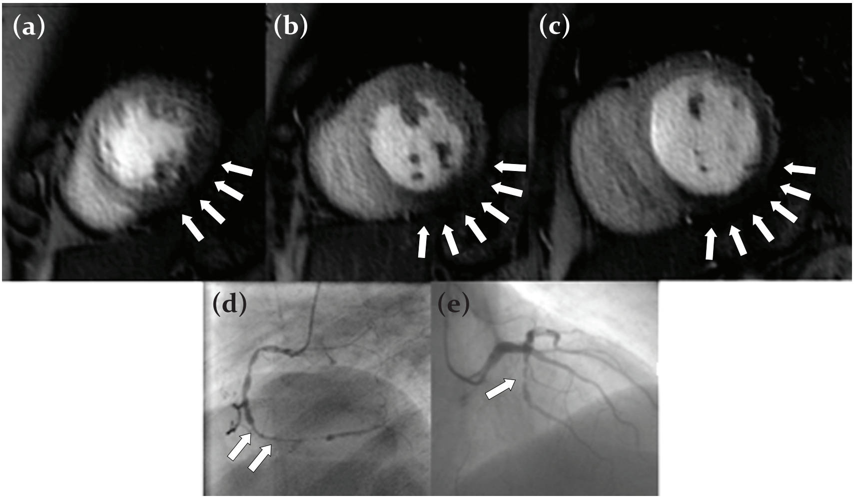

FIGURE 6.1 *k-t SENSE with SENSE training: CMR perfusion images acquired during adenosine stress shows a perfusion defect inferior in the apical slice (a), and inferior and inferolateral defects in the equatorial (b) and basal (c) slices. X-ray coronary angiography showed diffuse disease with subtotal occlusion of the right coronary artery (d; arrows) and a high degree stenosis of the left circumflex coronary artery (e; arrow).*

analysis were 0.75 (95% CI 0.51–0.91), 0.92 (95% CI 0.69–0.96), and 0.79 (95% CI 0.55–0.93) for the detection of >50% coronary artery stenosis in the LAD, LCX, and RCA, respectively. The mean perfusion scores for single and two-vessel disease at disease severity >50% were 11.0 (95% CI 5-17) and 16.0 (95% CI -35-67), respectively). Patients without significant coronary artery disease had a mean perfusion score of 0.4 (95% CI 0-1). Lower diagnostic accuracy was seen for the detection of coronary artery disease >75% (AUC 0.82 (95% CI 0.59–0.95) p=NS vs coronary artery disease >50%). At a cut-off value of 2, this resulted in a sensitivity and specificity of 86% and 77%, respectively.

The diagnostic accuracy for the low-resolution data were not significantly different compared to the high resolution data: 0.82 (CI 0.58-0.95) and 0.79 (CI 0.55-0.94) for the detection of >50% (p = 0.13) and >75%

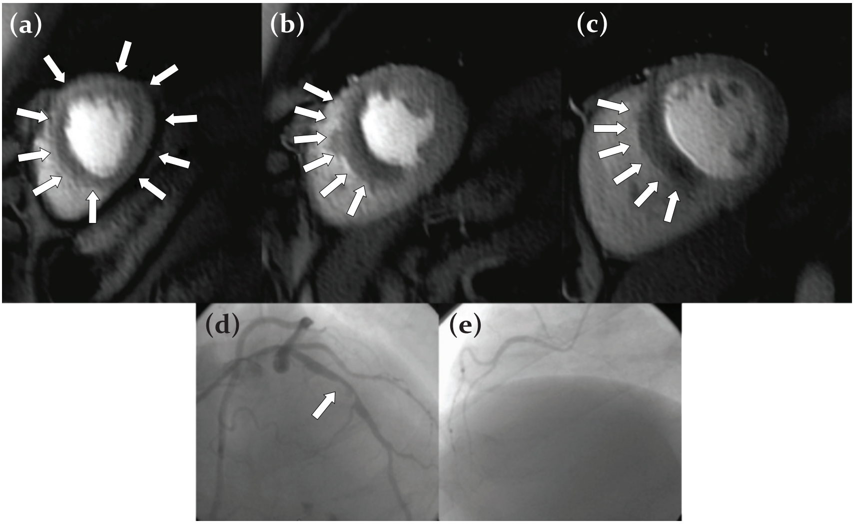

FIGURE 6.2 *k-t SENSE with SENSE training: CMR perfusion images acquired during adenosine stress in a patient with suspected CAD shows a circular perfusion defect in the apical slice (a), and anterior, anteroseptal and inferoseptal defects in equatorial and basal slices (b, c). X-ray coronary angiography confirmed a high degree stenosis of the left anterior descending artery (d; arrow) and a small right coronary artery (e)*

(p = 0.72) coronary artery disease, respectively (Fig. 6.3). Using a cut-off value of 2, sensitivity and specificity for the detection of >50% and >75% coronary artery stenoses were 80%, 50% and 86%, 46%, respectively.

Interobserver Agreement

Agreement analysis for the overall perfusion score showed a mean bias of 0.0 with 95% limits of agreement of 3.2 to -3.2. AUC of the ROC analysis were similar between the two observers for the main analysis of coronary artery stenosis >50%: 0.94 (95% CI 0.74–0.99) vs. 0.98 (95% CI 0.80–1.0), (p = 0.13).

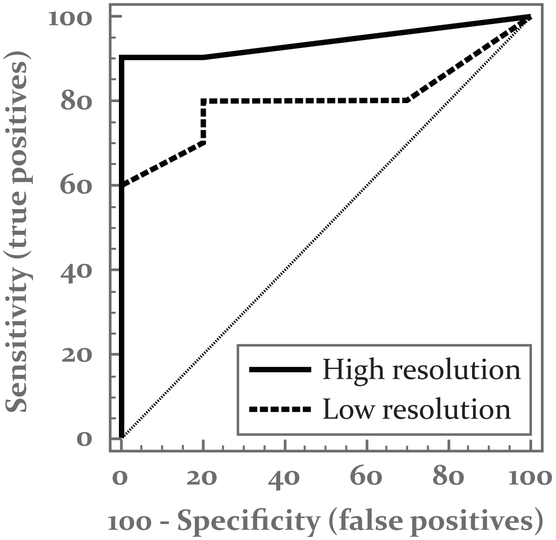

FIGURE 6.3 *Receiver-operating characteristics curve for the ability of the perfusion score to detect coronary artery disease (>50%) for high and low resolution data. The area under the ROC curve was 0.94 for the high resolution data and 0.82 for the low resolution data (p=0.13).*

Image Quality

The mean image quality score was 2.2 ± 0.7. None of the images were considered non-diagnostic.

6.3 Discussion

The clinical validation presented shows that highly accelerated CMR perfusion imaging using *k-t* SENSE with SENSE training is feasible in a clinical population, with excellent diagnostic performance in detecting coronary stenosis. Despite being able to only give an indication of the potential role of this novel method, the study demonstrated that it can be applied to a consecutive clinical population and can achieve high diagnostic accuracy and reproducibility.

As explained before in this chapter, *k-t* SENSE with SENSE training allows for higher acceleration compared to the standard *k-t* SENSE approach. In the current implementation, the speed-up was invested in improved spatial resolution, while keeping acquisition duration short. The decision for adopting this approach was based on the conclusions of recent work investigating the dark rim image artifacts [18; 106], which both placed emphasis on high spatial resolution as a factor to address this issue. In the present study, spatial resolution could be increased in comparison to previous studies, preventing the appearance of such artifacts and allowing for precise assessment of the transmural extent of the ischemic region. It is important to note that the diagnostic advantage comes at no cost with respect to the length of the acquisition window, which was kept below 90 ms per heartbeat. This has the additional benefit of reduced inter-shot cardiac motion, which could otherwise result in blurring or even contribute to dark rim artifacts.

With the current acceleration factors and the given shorter cycle intervals during stress exams, three slices could be acquired. It should also be noted that all subjects of this small study population could either perform the inspiration breathholds or were asked to perform shallow expiration after an initial inspiration breathhold. The latter was shown to minimize respiration related image artifacts often present when *k-t* SENSE is employed [134].

The overall diagnostic accuracy of perfusion imaging was slightly better relative to results from a previous study by Plein et al. [134], which presented an area under the curve of 0.94 vs 0.89, respectively. Cheng et al [149] also reported a slightly smaller area under the curve of 0.89 for imaging at 3.0 T. This particular study also compared high resolution datasets to low resolution ones, without proving a significantly better diagnostic accuracy. Here, however, it could be shown that despite the fact that the sensitivity using the high resolution data remained approximately the same compared to the case of the low resolution data, the specificity was lower. This increase in specificity in the high resolution data sets might be explained by the reduction of subendocardial dark rim artifacts which, in turn, results in less false positive interpretations of perfusion studies. In view of these differences, larger patient studies are warranted to verify the trend for higher diagnostic performance when the *k-t* SENSE with SENSE training method is employed.

A clear limitation of the present work is the limited sample size. The accuracy, however, of previous studies that used a similar evaluation method as well as the agreement of the analyses of the two observers who evaluated the data, could justify confidence to the conclusion. Another limitation is the use of X-ray coronary angiography to determine whether relevant CAD was present. Despite the fact that it remains the most important clinical modality to assess ischemia, it only provides an indirect estimate of the flow reduction caused by coronary artery stenosis.

In the following chapter, we will present a modification of *k-t* PCA, which addresses similar temporal fidelity issues as the method presented here, this time, though, in 3D datasets.

CHAPTER 7

3D Perfusion Imaging Using *k-t* PCA

As we alluded in Chapters 1 and 3, the extent of hypoperfused tissue and hence the tissue weight contributing to the ischemic burden is a strong predictor of cardiac outcome. This has also been demonstrated in the past in patient studies performed using CMR or other imaging modalities [19–21]. Considering this, one can draw the conclusion that the extent of ischemic tissue should accurately be assessed with adequate spatiotemporal resolution [150].

Three dimensional imaging allows for contiguous coverage of the whole left ventricle and subsequently for more accurate estimation of the extent of ischemic burden. Moreover, due to its inherently high SNR and reduced geometry-related noise enhancement [151], higher acceleration factors can be employed with parallel imaging without severely compromising

---

This chapter is adapted from "Vitanis V., Manka R., Giese D., Pedersen H., Plein S., Boesiger P. and Kozerke S., *High resolution 3D cardiac perfusion imaging using compartment-based k-t PCA. Magnetic Resonance in Medicine, Under Review*" image quality. Another advantage of 3D imaging is the prevention of misregistration problems often seen in multi-slice acquisitions. Such problems can affect myocardial perfusion imaging, especially when the acquisition is performed over more than one heartbeat. In previous work, Kellman et al. [152] acquired 10 slices at 1.5T, using 6× 2D TSENSE [137] and a matrix of 128×78×10 within an acquisition window of 312 ms. Recently, Shin et al. [153] were able to acquire 3D perfusion data with 10 slices at 3.0T, using 6× 2D SENSE [151] and a matrix of 100×66×10 within a window of 304 ms. Experiments in both cases were performed under rest conditions.

The spatial resolution in these previous studies [152; 153] may be insufficient to detect subendocardial defects and remains substantially below that of 2D CMR perfusion methods. As explained in Chapter 3, increased resolution for 3D perfusion may reduce the dark-rim artifacts reported in studies [18; 106]. Another limitation of these previous studies is the long acquisition window on the order of 300 ms, which needs to be shortened to avoid potential motion artifacts, especially under stress conditions.

In order to increase resolution and reduce the acquisition window, we propose in this chapter the application of *k-t* PCA (see [132] and Section 4.5) with an undersampling factor of 10 for acquiring high-resolution 3D perfusion images at 3T.

7.1 Materials and Methods

The proposed method is based on the *k-t* PCA method, described in detail in Section 4.5. Briefly, in *k-t* PCA reconstruction fidelity is increased by transforming the training data from the *x-f* domain to the *x-pc* domain using a matrix A (Eq. 4.51).

$$\boldsymbol{\rho}_{tr} = A\boldsymbol{w}_{tr} \tag{7.1}$$

This matrix A can be calculated from the Principal Components of the training along the temporal frequency direction, represented as rows in matrix B. For easy reference Eq. 4.62 is given again here:

$$A = B^T \otimes I_{N_x} \tag{7.2}$$

As explained in Chapter 4, the fundamental assumption of *k-t* PCA is that the true *x-f* data $\boldsymbol{\rho}$ are given by (Eq. 4.56)

$$\boldsymbol{\rho} = A\boldsymbol{w} \tag{7.3}$$

where $\boldsymbol{w}$ is the solution of the following inversion problem (Eq. 4.57):

$$\boldsymbol{w} = \tilde{\Theta}\tilde{E}^H(\tilde{E}\tilde{\Theta}\tilde{E}^H + \lambda\Psi)^{-1}\boldsymbol{\rho}_{alias} \tag{7.4}$$

The assumption in Eq. 7.3 can be restated as follows: the true *x-f* data $\boldsymbol{\rho}$ are described by the same temporal basis functions (B) as the ones describing the training data. This highlights the fact that any error in the calculation of the basis functions can directly affect the final reconstruction result.

A significant source of error in the calculation of matrix B are partial-volume effects in the low-resolution training data. For instance, in a perfusion dataset the large voxels of the septal wall in the training contain temporal information from both the septal wall and the two ventricles, an issue also referred to as *signal contamination*. As such, the temporal response given as input to the PCA does not reflect the actual contrast uptake, but a mixture of signals from the myocardium and the left and right ventricles (Fig. 7.1h, perfusion curves in color), therefore compromising the accuracy of matrix B.

The modified *k-t* PCA reconstruction proposed herein aims at circumventing errors in the calculation of the temporal basis functions by defining spatial compartments within the 3D volume of a perfusion dataset. The idea is as follows: On a higher resolution dataset (e.g. a dataset consisting of the sliding window reconstruction of the undersampled data and the training) a number of compartments of interest (e.g. right ventricular blood pool, left ventricular blood pool, left ventricular myocardium, rest of image) are automatically defined (more details in the following subsection). Subsequently, the perfusion curves of the myocardium are derived and voxels that display non-physiological temporal behavior due to partial-volume effects are automatically excluded based on the bolus arrival times and the gradients and deviations of those perfusion curves. Finally, from the selected voxels of each compartment i the $B_{comp(i)}$ matrices are calculated and the reconstruction problem is solved using a $B_{comp(i)}$ matrix for each compartment, including the non-selected voxels. It should be noted at this point, that, in order to avoid any temporal filtering due to the sliding window reconstruction of the undersampled data, the derivation of the perfusion curves and the exclusion of the voxels were performed solely on the training dataset.

Using the notation introduced before (Eq. 7.2), the transformation A will now contain replicas not of the one matrix B representing the temporal basis functions of the whole image (conventional *k-t* PCA), but replicas of the $B_{comp(i)}$ matrices calculated for each compartment:

$$A = B^T_{comp(i)} \otimes I_{N_x} \tag{7.5}$$

For completeness, we should note here that:

$$\sum_{i=1}^{\substack{number\ of\\ compartments}} voxels \in comp(i) = N_x \tag{7.6}$$

The definition of the compartments and the exclusion of certain voxels from the calculation of the B matrix are expected to have two main implications with respect to the reconstruction fidelity. First, by using a certain set of temporal bases adapted to each compartment, the sparsity achieved by the transform will be higher, the number of overlapping signals will be reduced and the conditioning of the inversion will be improved. Secondly, the exclusion of voxels that exhibit non-physiological temporal behavior due to partial-volume effects will result in more accurate temporal basis functions and consequently in more accurate reconstructions. To test these hypotheses, simulations were performed on a numerical phantom. The fidelity of the reconstruction was then tested *in vivo*.

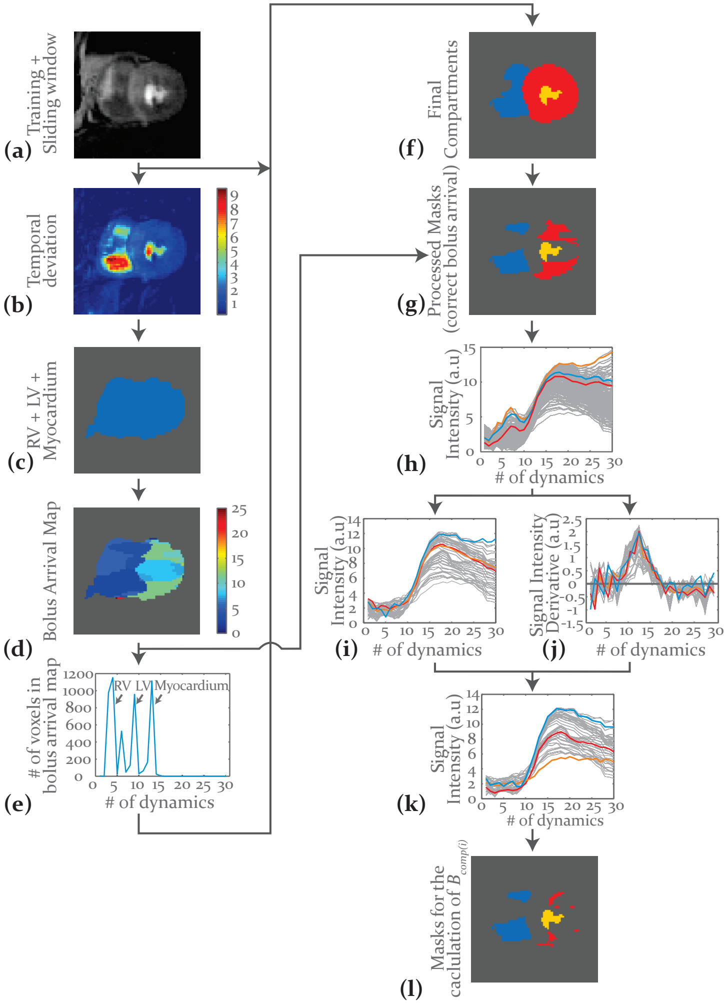

FIGURE 7.1 *Flowchart of the algorithm employed to define compartments. From the composite dataset (a), the temporal deviation of the data is calculated (b). After thresholding, a mask containing the right ventricular pool (RV), the left ventricular pool (LV) and the left ventricular myocardium (myocardium) (c) and subsequently a bolus arrival map are calculated (d). From a histogram of the bolus arrival values (e) the final compartment masks are defined (f), which are then processed (g) and used to calculate signal intensity-time curves (h). After excluding signal contaminated (i) and temporally filtered curves based on signal derivatives (j), the final perfusion curves (k) and the corresponding masks for the calculation of the $B_{comp(i)}$ matrices (l) are derived.*

Compartment Definition

In order to reduce errors in the $B_{comp(i)}$ matrices, the masks that define the final compartments (Fig. 7.1f) are further processed: The voxels of each compartment that exhibit a bolus arrival time different from the one expected from the histogram (Fig. 7.1e) are excluded from the calculation of the $B_{comp(i)}$ matrices (Fig. 7.1g). Then, the myocardial voxels that display high relative temporal deviation before the upslope (3x the mean noise variance), due to signal contamination (Fig. 7.1h), are excluded (Fig. 7.1i) and finally the voxels whose perfusion curves exhibit high negative gradients (Fig. 7.1j) before the upslope (1.5x higher compared to those after the upslope), due to temporal blurring, are also removed from the mask (Fig. 7.1k). The remaining voxels define the masks (Fig. 7.1l) which the matrices $B_{comp(i)}$ will be derived from.

The masks for RV and LV (Fig. 7.1g) are not further modified, since the temporal behavior exhibited by the underlying voxels does not suffer from severe partial volume effects. In order to give an order of magnitude with respect to the number of myocardial voxels excluded during compartment definition for all slices of the exemplary dataset of Fig. 7.1, the number of myocardial voxels before and after exclusion was 1318 and 495, respectively.

Acquisition Scheme

Fig. 7.2a illustrates the data acquisition pattern in the k_y-k_z plane for two consecutive dynamics used both in computer simulations and *in vivo* experiments. As indicated, training data were acquired interleaved with undersampled data using a partial Fourier scheme. In addition, an elliptical *k*-space shutter was applied to reduce the number of points to be sampled by 25%.

Numerical Phantom

A numerical phantom was used as a basis for computer simulations. The phantom was generated from an actual 3D perfusion scan and its sensitivity

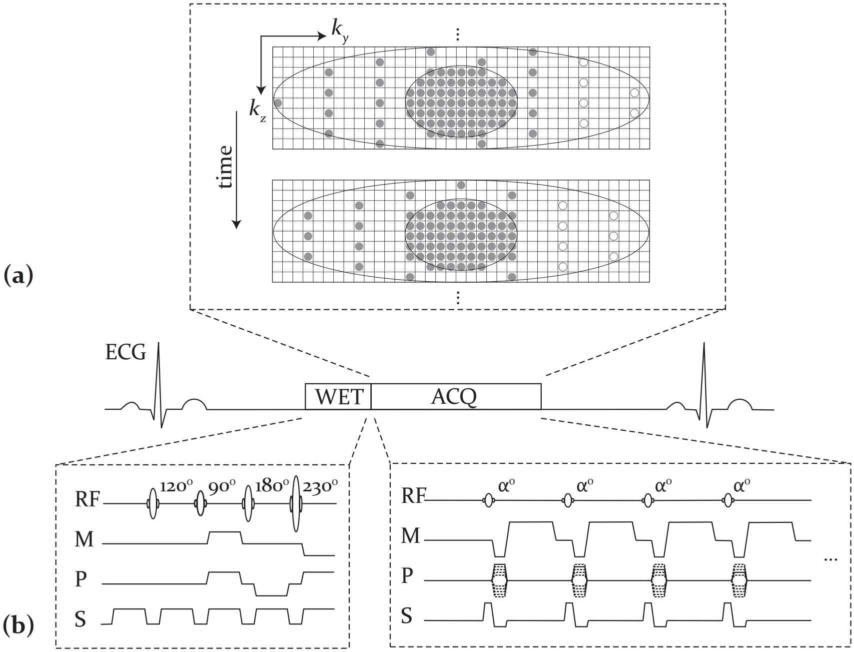

FIGURE 7.2 *(a) Acquisition pattern. Training and undersampled data were acquired on a sheared-grid in an interleaved manner. The empty circles indicate the points on the sheared-grid that were not sampled due to the partial Fourier acquisition scheme. The two ellipses denote the shutter used to reduce the sampled points by approximately 25%. (b) The acquisition scheme comprising a WET saturation pre-pulse and a gradient echo sequence.*

map (six-channel coil array). The reconstruction matrix was 144×144×10 with 30 dynamics. Perfusion curves for the different anatomical regions were extracted from the same scan and intensity variations in the model were simulated accordingly. Uncorrelated Gaussian noise was added to the real and imaginary channels of each coil, such that the combined fully sampled image had a typical SNR value of 30 [120] on the septal wall during signal peak.

Simulations

Three series of simulations were performed based on the phantom described above. The first series investigated the efficacy of the proposed modified *k-t* PCA method as a function of the number of training profiles and of the Principal Components (PCs) used in the reconstruction. For this purpose, the data sets were decimated to simulate a 10x nominal acceleration with 9 to 21 training profiles (4 values) along the k_y direction and 7 profiles along the k_z direction, resulting in a net acceleration of 7.5-5.6×. Comparisons were performed between the conventional and the compartment-based *k-t* PCA algorithms using 3 to 30 PCs (13 values). To allow for quantitative assessment of the reconstruction result, perfusion curves were extracted from several regions of the myocardium and the mean absolute error was calculated having as reference the curves from the corresponding Roemer reconstructed [130] fully sampled data sets.

The second series of simulations aimed at investigating the efficacy of the method as a function of the k-t PCA acceleration factor. The data sets were decimated to simulate a nominal acceleration between 3× and 12× (5 values) with 9 to 21 training profiles (4 values). The number of PCs used in the reconstruction was kept constant and equal to 12. The evaluation of the reconstruction result was performed by comparing perfusion curves, similar to the first series of simulations.

The objective of the third series of simulations was to test the robustness of the proposed method to drifting in the breathing position during the last dynamics as well as to sudden motion during the myocardial signal upslope. To simulate drift the myocardium was shifted during the last 10 dynamics in the inferior and lateral directions [154], in each by 1-5 pixels (4 values), corresponding to a displacement of 2.5-12.5 mm for a FOV_y of 360 mm. To simulate sudden motion the myocardium was shifted by the same amount (4 values) in the inferolateral direction during dynamics 15-17 and in the opposite direction during dynamics 17-19. Then the datasets were reconstructed using 11 training profiles and 12 PCs and the perfusion curves derived were compared to the reference, as in the previous simulations. For this particular series of simulations a comparison with *k-t* SENSE was additionally performed, since this method is known to be sensitive to motion of the myocardium in perfusion imaging.

It is important to note at this point, that the sensitivity maps used for the *k-t* PCA reconstructions were estimated using an autocalibrated method [120; 143]. Moreover, the regularization factor (Eq. 7.4) was set equal to 1 in all simulations to match the value proposed in [132].

In Vivo Experiments

In vivo experiments comparing *k-t* PCA with and without compartments were carried out in six patients (age 52.6±8) with suspected coronary artery disease. All subjects gave informed consent according to the institutional policy.

Perfusion images were acquired with 10-fold undersampling on a 3T Philips Achieva scanner (Philips Healthcare, Best, The Netherlands) with a 6-element phased array, using a WET saturation pulse (30) and a gradient echo sequence. Imaging parameters included TR = 1.8 ms, TE = 0.7 ms, flip angle = 15°, typical FOV 380×330 mm^2, saturation prepulse delay = 150 ms, acquisition time per heart beat = 225 ms, 75% partial Fourier acquisition in k$_y$, acquired slices = 10, slice thickness = 10 mm, dynamics = 30, inspiration breathhold). The acquisition matrix was chosen such that the in-plane spatial resolution was constant and equal to 2.3×2.3 mm^2. For a typical matrix of 168×133, acquired using partial Fourier and the elliptical shutter described in Fig. 7.2, 11 k$_y$ and 7 k$_z$ training profiles a net acceleration factor of 7.0 was achieved.

The patients underwent vasodilator-stress and rest CMR perfusion studies. For stress acquisitions, adenosine was administered intravenously at a dose of 140 µg/kg/min for 4 minutes. At 3 minutes of the infusion, an intravenous bolus injection of 0.1 mmol/kg gadopentetate dimeglumine, (Magnevist, Bayer Schering Pharma, Berlin, Germany) was given via a power injector (Spectris Solaris, MEDRAD, Minneapolis, USA) at a rate of 4ml/s, followed by a 20ml saline flush. After a 15 minute waiting period for contrast agent washout, an identical perfusion scan was repeated at rest. All patients went on to invasive X-ray coronary angiography. The coil sensitivity maps were estimated using the same autocalibrated method as used for the model reconstructions. To partly compensate for the signal drop-off due to B1 inhomogeneities, the final images were divided pixel-wise by the virtual body coil calculated from the sensitivity maps [155; 156]. The partial Fourier data were reconstructed using homodyne reconstruction [144].

Quality Analysis

Due to absence of “ground truth” non-accelerated data in the *in vivo* experiments, the comparison of the conventional *k-t* PCA and the compartment based *k-t* PCA schemes was performed as follows. First, signal intensity curves were extracted from six sectors on the myocardium on each slice of the 3D volume. The resulting curves were visually compared with respect to signal contamination or temporal blurring artifacts. The signal upslopes were then calculated and bulls-eye plots were derived. The uniformity of the upslope values of healthy sectors was used as an indication of the fidelity of the reconstruction.

7.2 Results

Numerical Phantom

In the upper half of Figure 7.3 perfusion curves from the anteroseptal sectors of an apical, a midventricular and a basal slice of the 3D model are illustrated, using the conventional and the compartment-based *k-t* PCA. In the lower half, the same perfusion curves are presented, this time for the inferolateral sectors. It can be seen that the proposed reconstruction scheme eliminates the signal contamination observed (arrows in Fig. 7.3b, c, f) with conventional *k-t* PCA. It can also be noted that the signal contamination is more pronounced in the septal regions, which are affected by the high signal transitions in the right and left ventricles.

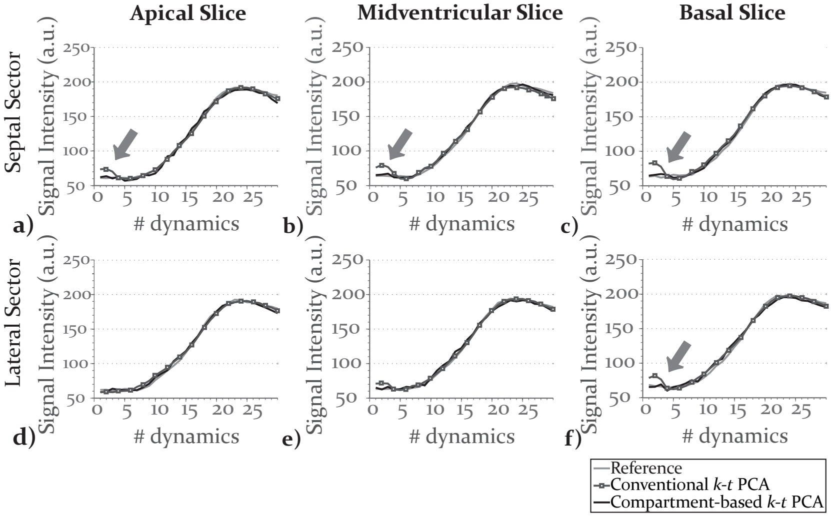

FIGURE 7.3 *Computer simulations. Comparison of perfusion curves between the conventional and the compartment-based k-t PCA reconstructions (11 k_y and 7 k_z training profiles, 12 PCs) for an apical slice (left column), a midventricular slice (middle column) and a basal slice (right column). Subfigures (a), (b) and (c) correspond to an anteroseptal sector, whereas subfigures (d), (e) and (f) correspond to an inferolateral sector. The arrows indicate the curves that are affected by signal contamination. The reference curve from fully sampled data is given in black.*

Figure 7.4a illustrates a slice of the reconstructed numerical phantom during contrast uptake in the LV. The *y-t* plots along the dashed line, presented in Fig. 7.4b and c, appear very similar between the two methods under consideration. The magnified error plots are also very similar, with the exception of the septal region, where a slightly increased error for the conventional *k-t* PCA can be seen in the first dynamics. This can be better illustrated in the perfusion curves of Fig. 7.4d, as well as in the error curves of Fig. 7.4g. Both were calculated only on the specified section for all pixels within the septal region. The signal contamination on the septal wall before the upslope is the main issue affecting the conventional *k-t* PCA reconstruction and is sufficiently addressed by the proposed, compartment-based *k-t* PCA.

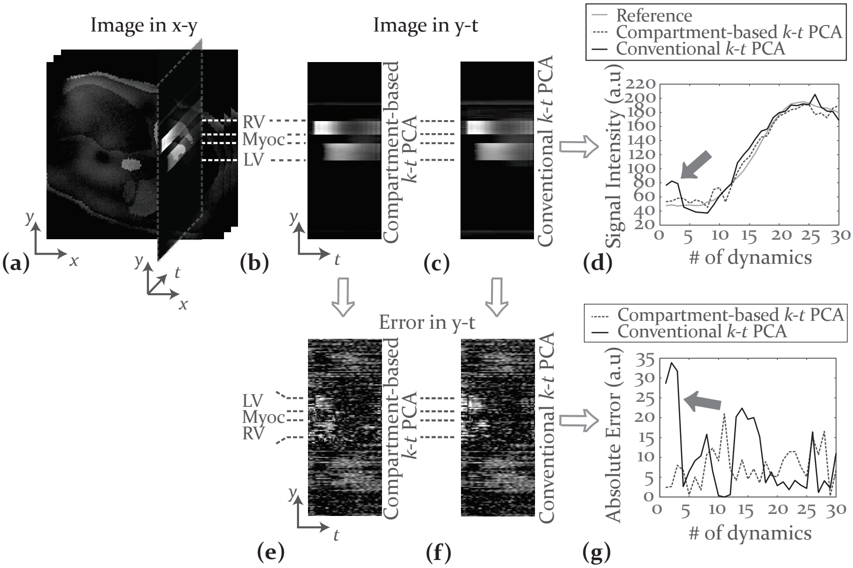

FIGURE 7.4 *Computer simulations. (a) A reconstructed midventricular slice of the numerical phantom during contrast uptake in the LV. A section along the dashed line plotted over time for the compartment-based and the conventional k-t PCA reconstructions (b and c, respectively). The corresponding error images with respect to the reference dataset (e and f) (upscaled 10×) along with perfusion (d) and error curves (g) from the septal region of the myocardial section. The dotted lines show the different regions of interest in the y-t plots, whereas the arrows indicate the time points where the curves are affected by signal contamination.*

Figure 7.5 depicts the mean absolute error between the reference perfusion curves and those from the conventional and compartment-based *k-t* PCA reconstructions as a function of the number of principal components and training profiles. It is seen that the compartment-based scheme results in lower errors compared to the conventional one both for the septal and the lateral sector for all numbers of principal components

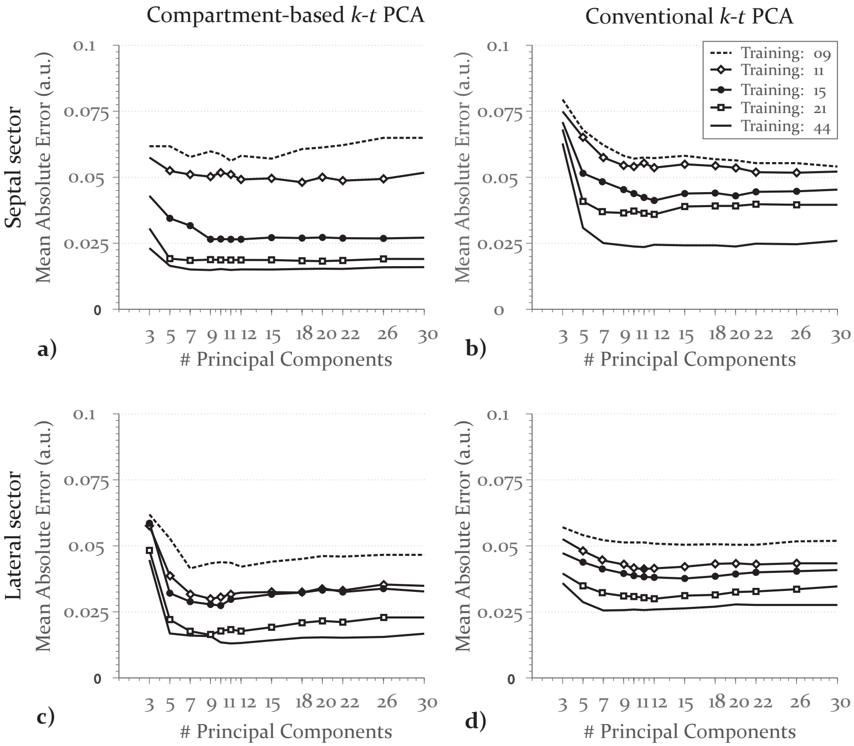

FIGURE 7.5 *Computer simulations. Mean absolute error vs. number of principal components for different number of training profiles for the compartment-based k-t PCA reconstruction (left column) and the conventional k-t PCA (right column). The upper row reflects the errors for the anteroseptal sector, while the lower row reflects the errors for the inferolateral sector. For easy reference, the same scaling has been used in all subfigures.*

and training profiles used, except for the case when 9 profiles are used, where the two methods in the septal region perform similarly.

Another observation is that errors decay as a function of the principal components up to a number of approximately 10 and then stay almost constant for larger numbers. As before, exception is the case of the compartment-based *k-t* PCA for the septal region and for 9 training profiles. It should finally be noted, that the error decreases with increasing number of training profiles and is lower for the lateral region than for the septal one.

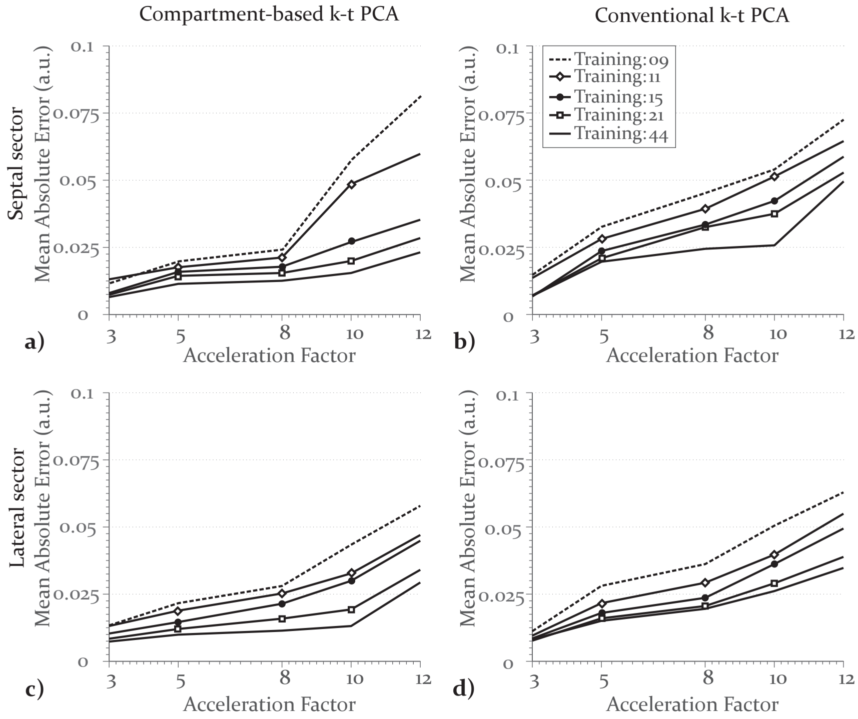

FIGURE 7.6 *Computer simulations. Mean absolute error vs. acceleration factor for different number of training profiles for the compartment-based k-t PCA reconstruction (left column) and the conventional k-t PCA (right column). The upper row reflects the errors for the anteroseptal sector, while the lower row reflects the errors for the inferolateral sector. For easy reference, the same scaling has been used in all subfigures.*

Figure 7.6 gives the mean absolute error between the reference perfusion curves and those from the *k-t* PCA reconstructions as a function of the acceleration factor for a number of training profiles. Only the septal sector is plotted for brevity.

It is seen that the error in the perfusion curves increases monotonically with respect to the acceleration factor. Comparing the two reconstruction methods, one notices that the proposed scheme results in lower errors for almost all acceleration factors and number of training profiles. Exception is again the case of the septal region when 9 profiles are used. Another general observation is that for low acceleration factors, the two methods produce similar results, whereas for higher acceleration factors and for more than 9 profiles the differences are larger and in favor of the compartment-based variant.

Figure 7.7 illustrates the results of the third series of simulations. Compared to *k-t* SENSE, *k-t* PCA results in significantly better reconstructions both for drifting and abrupt motion. When the motion of the myocardium is gradual (Fig. 7.7a and c), *k-t* PCA is robust, with the compartment-based variant resulting in slightly lower errors compared to the conventional one. However, when the motion is large, abrupt, and occurs during the myocardial upslope (Fig. 7.7b and d), the reconstruction result is compromised. Even in this extreme case, the delineation of the myocardium by *k-t* PCA is clearer compared to *k-t* SENSE.

In Vivo Experiments

Figure 7.8 illustrates the comparison between the two *k-t* PCA variants for the first two subjects, one with a normal X-ray coronary angiogram (Fig. 7.8a-d) and the other with 80% stenosis of the right coronary artery. In the first, it can be seen that the proposed compartment-based *k-t* PCA (7.8a) eliminates the temporal blurring seen with the conventional variant (7.8c, arrow). Moreover, it results in a more uniform distribution of upslope values in the bull's-eye plot (7.8b vs d). Similar observations can be made for the second subject; signal contamination and temporal blurring artifacts seen with the conventional *k-t* PCA (Fig. 7.8g) are prevented with the proposed method (Fig. 7.8e). Furthermore, the bull's-eye plots of the compartment-based *k-t* PCA exhibit more uniformity in the healthy and in

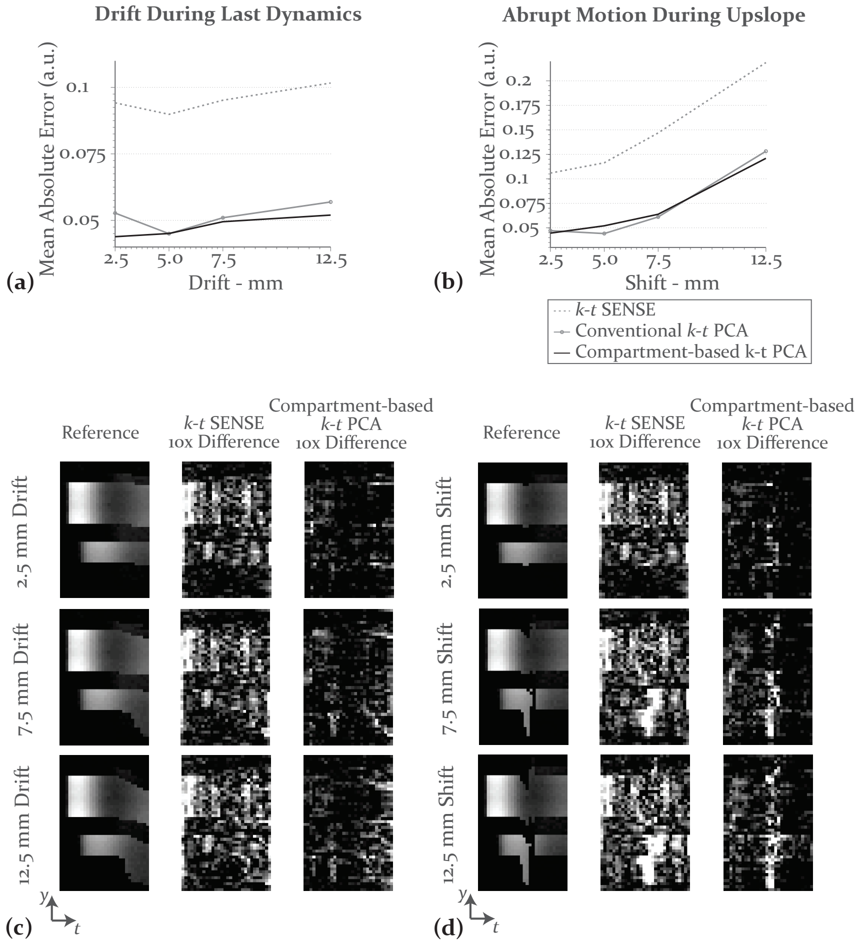

FIGURE 7.7 *Computer simulations. Mean absolute error vs. shift of the myocardium in each direction for k-t SENSE and k-t PCA with and without compartments. The error for the k-t PCA variants is significantly lower compared to k-t SENSE for all cases. If the motion is gradual and occurs during the last dynamics, the error is low (a and c, first two rows). For large drifting (c, last row), some blurring occurs in the septal wall. If the motion is abrupt and occurs during the upslope (b and d), k-t PCA performs well for small shifts (d, first two rows) and less well for large shifts (d, last row). Even for extreme shifts (d, last row), the delineation of the myocardial walls is more accurate when k-t PCA is employed, relative to k-t SENSE.*

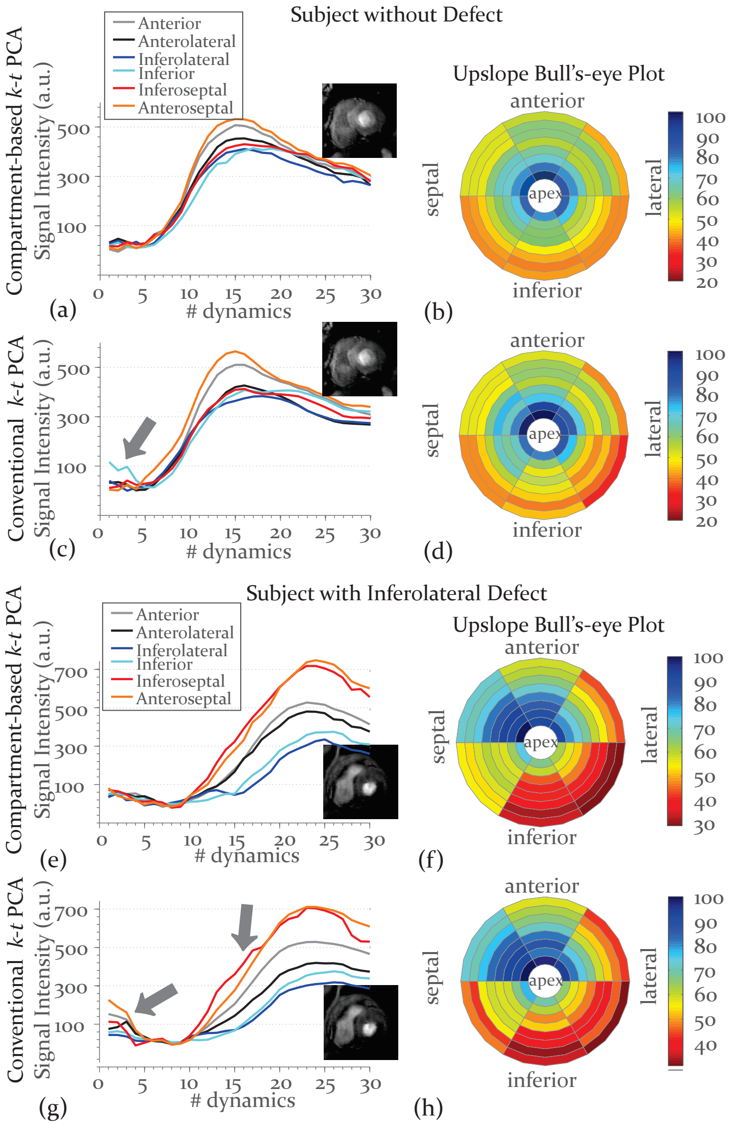

FIGURE 7.8 *In vivo data. Comparison of perfusion curves (8a and c) and upslope bull's-eye plots (b and d) between the proposed (upper row) and the conventional method (second row) for a patient without defect. The compartment-based k-t PCA eliminates the temporal blurring and signal contamination (a vs. c) seen in the curves of the original variant (arrows). It also results in a more uniform distribution of the upslope values in the bull's-eye plots (b vs. d). Similar observations can be made for the curves (e and g) and upslope bull's-eye plots (f and h) of a patient with an inferolateral defect.*

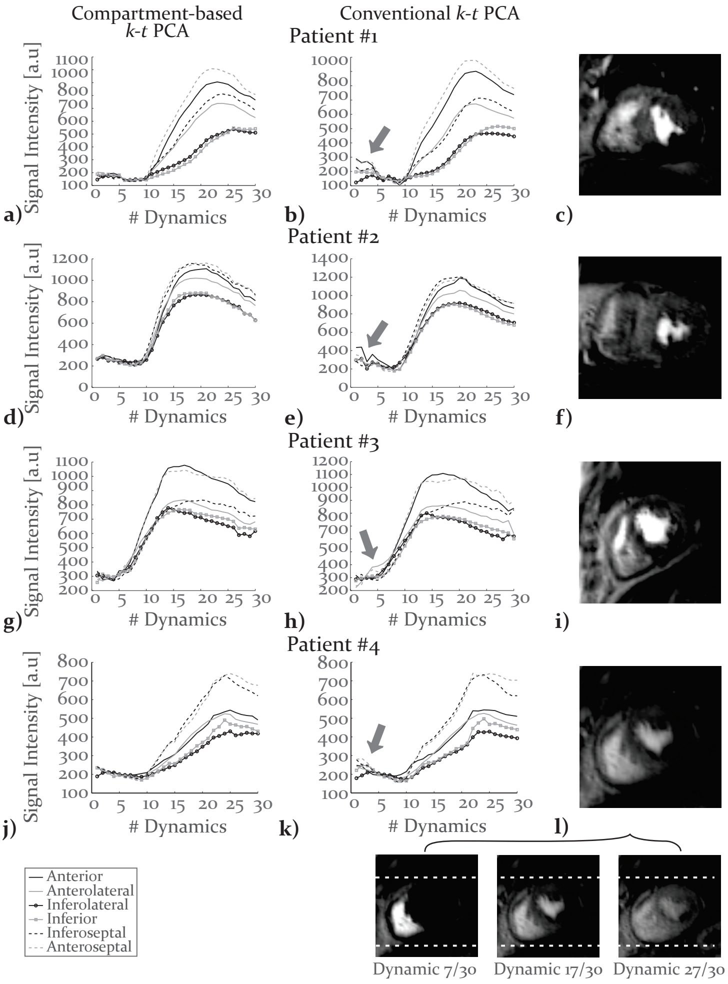

FIGURE 7.9 *In vivo data. Comparison of perfusion curves for four subjects. The compartment-based k-t PCA (left column) could eliminate temporal blurring as well as signal contamination reflected in the curves of the conventional method (middle column) for each of the four patients. The first patient had an obstructed RCX (first row), reflected in a hypointense posterolateral wall (9c). The second patient had a three-vessel disease (64% LAD, 85% RCA and 73% RCX stenosis). The third patient had a two-vessel disease (65% LAD and 75% RCA stenosis). The fourth (76% RCA stenosis) could not hold their breath throughout the scan, which resulted in a drift in the position of the myocardium during the second half of the exam. The dashed lines in the last row depict initial and final positions of the heart, corresponding to a shift of 4 pixels (∼8 mm).*

the ischemic sectors (Fig. 7.8f) compared to the plots from the conventional reconstruction (Fig. 7.8h).

Figure 7.9 presents perfusion curves and midventricular images from four additional patients with various degrees of stenosis. The first patient (first row), had an obstructed right circumflex artery (RCX), with 51% luminal diameter reduction, resulting in a hypointense posterolateral wall. The second patient (second row), had a three-vessel disease with 64% left anterior descending (LAD), 85% right coronary artery (RCA) and 73% RCX stenosis. The third patient (third row) had two-vessel disease with 65% LAD and 75% RCA stenosis. The fourth patient, who suffered from 76% stenosis of the RCA, could not hold his breath throughout the exam; as a result there was a drift in the position of the myocardium during the second half of the scan. Despite that fact, the compartment-based *k-t* PCA reconstructed the data correctly, providing diagnostic images.

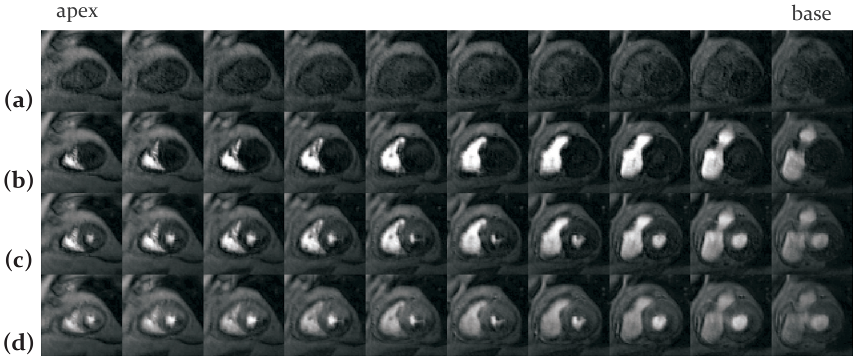

FIGURE 7.10 *In vivo data. Ten slices of the 3D volume before bolus arrival (a) and during contrast update in the RV (b), the LV (c) and the myocardium (d) are shown. The ischemic area is seen to extend to the inferolateral region.*

Figure 7.10 shows representative perfusion images from the second patient of Fig. 7.8 before contrast arrival (Fig 7.10a) and during RV, LV and myocardial enhancement (Fig. 7.10b, c, d, respectively).

7.3 Discussion

In this chapter, compartment-based *k-t* PCA has been introduced and compared to conventional *k-t* PCA reconstructions of simulated and in-vivo 3D myocardial perfusion data. Using compartment-based *k-t* PCA accurate depiction of myocardial contrast uptake is achieved permitting whole-heart 3D perfusion imaging at 7-fold net acceleration yielding a spatial resolution of $2.3\times2.3\times10$ mm^3 during a 225 ms acquisition window.

When *k-t* PCA is employed to accelerate perfusion imaging, the accuracy of the basis function set and subsequently the quality of the reconstruction is largely dependent on the number of training profiles. If the training dataset suffers from severe partial-volume effects, the temporal behavior that is encoded in the basis functions is a mixture of signals from several anatomical regions, which are collocated in the large voxels of the training data. This is a considerable issue for the critical region of the myocardium, where the strong signals from the right and left ventricles prevail, giving rise to the signal contamination artifact.

In the present work, we have described a method for ameliorating this issue by defining a number of compartments and subsequently solving the reconstruction problem based on compartment-specific temporal basis functions. In both computer simulations and *in vivo* experiments it was seen that for a 10× nominal acceleration, the temporal fidelity of the conventional *k-t* PCA cannot properly depict myocardial contrast uptake. By removing the myocardial perfusion curves affected by the signal contamination, the temporal blurring and in particular the signal contamination is significantly reduced.

An overall observation is that both conventional and compartment-based *k-t* PCA benefit from the usage of more principal components in the reconstruction. As it was noted in the preceding work by Pedersen et al. [132], a number of components around 10-12 can be considered a good trade-off between reconstruction accuracy and computing time due to larger inversion matrices.

There are two prerequisites for an effective reconstruction. First the compartment masks should be correctly defined. This implies, as the first series of numerical simulations demonstrated, that an adequate number of training profiles (preferably 11 or more in-plane) should be available, so that the composite dataset is of sufficient quality to allow for accurate thresholding of the regions of interest. If only a limited number of training profiles are available, the composite dataset contains folding artifacts, particularly replicas of the highly dynamic right and left ventricles. Since the spatial thresholding that defines the compartments is based on temporal derivatives and variance values, any folding artifacts of such dynamic regions result in improper assignments of voxels to compartments. This naturally has further implications, since those voxels will erroneously be reconstructed using another temporal basis function set.

The second prerequisite for the calculation of physiologically realistic bolus arrival times and the subsequent definition and exclusion of signal contaminated myocardial perfusion curves relates directly to the number of training profiles. If a low number of training profiles is acquired in-plane, the bolus arrival map (Fig. 7.1d) is dominated by the bolus arrival time of the spatially smeared, strong signal of the right and left ventricles. This results in erroneous identification of the myocardial curves to be filtered out (Fig. 7.1h) and calculation of inaccurate temporal basis functions for the myocardial compartment. For the typical acquisition matrices used in the experiments, it is recommended that 11 training profiles are acquired in-plane, so that there is an accurate definition of temporal basis functions.

The second series of simulations indicated that the proposed method results in lower reconstruction errors throughout the range of acceleration factors. Since the temporal fidelity issues are more pronounced with higher acceleration factors, the benefit of using the proposed method is more significant when the nominal acceleration is higher than 8-fold.

The third series of simulations confirmed the results reported in [132] with respect to the robustness of k-t PCA to motion. Compared to *k-t* SENSE, *k-t* PCA and its compartment-based variant resulted in better reconstructions, especially for small drifts during the later part of an exam. This can be explained if we consider the fact that the bolus arrival definition depends only on the images acquired during contrast uptake and, accordingly, drifts in the breathing position toward the end of the scan do not significantly affect the reconstruction result. In case there is large sudden motion during the upslope, however, the reconstruction fidelity can be compromised, since it can result in folding artifacts and subsequent improper assignment of voxels to compartments. In general, however, consistency of the breathing level during contrast uptake is desired to simplify data analysis.

The in-vivo exams confirmed the improvements by the compartment-based *k-t* PCA over the original variant. In the first two subjects, the proposed method eliminated any temporal blurring or signal contamination artifacts seen in the perfusion curves when the conventional method was used. Moreover, the upslope value distribution using the former method was more uniform in the healthy sectors compared to the one from the latter. The images and the perfusion curves of the other four subjects demonstrated that the proposed *k-t* PCA method can perform well in a variety of clinical situations and degrees of coronary artery stenosis, even in cases where slight breathing motion is present. It should be pointed out that the difference in values between the septal and the lateral regions in a healthy myocardium is attributed to B1 inhomogeneities, which could not be fully corrected for by the virtual body coil. A clear limitation of the comparison performed on the *in vivo* data is the lack of “ground truth” non-accelerated data. As such, this comparison could only be performed qualitatively by observing the perfusion curves and the corresponding signal upslopes.

An essential step in the whole reconstruction process is the exclusion of the contaminated perfusion curves before the calculation of the temporal basis functions. Special care has been given so that this filtering was not excessive and only affected the signal contaminated curves. Considering that the exclusion is based on the temporal variance of the curves, one should perform this step with caution so that low signal curves with relatively high noise and variance are not removed. By doing so, any myocardial defects in patients will be well represented and well differentiated from healthy myocardium.

As both simulations and in-vivo exams have shown, the compartment-based method is most beneficial for the septal than for other myocardial regions. This is expected, considering the fact that the filtering performed before the calculation of the temporal basis functions (Fig 7.1h and 7.1i) aims exactly at removing the signal contamination that is predominant in the septal myocardial zone.

Finally, several of the issues mentioned before, can be ameliorated, if the whole process is performed on a previously reconstructed dataset, e.g. using *k-t* SENSE, or if the compartments are drawn manually. However, we refrained from such a course of action in order to reduce the preprocessing and the total reconstruction time.

As a conclusion, it was shown that the compartment-based *k-t* PCA reconstruction method addresses issues associated with the coarse spatial resolution of the training data in perfusion imaging. Excluding signal-contaminated perfusion curves from the calculation of the temporal basis functions can improve reconstruction, leading to more accurate perfusion curves and reliable semi-quantitative perfusion analyses. In the following chapter, quantification of perfusion image series using this reconstruction method as well as its conventional variant and *k-t* SENSE is presented.

CHAPTER 8

Quantitative Analysis of Accelerated Perfusion Imaging

In the previous chapters the significance of parallel imaging methods in enhancing the clinical applicability of CMR perfusion imaging was emphasized. Those techniques can relax the trade-off between the spatial and temporal resolutions and lead to single heart-beat multi-slice 2D acquisitions with spatial resolutions of up to 1×1 mm^2 in plane or even to 3D acquisitions with spatial resolutions of up to 2.3×2.3 mm^2 in plane and 10 slices.

Despite the advent of those new techniques, the interpretation of perfusion CMR images has been performed in the majority of clinical studies only qualitatively [71–74] or semi-quantitatively [75–78]. Issues related to quantitative analysis such as nonlinearity of the relationship between signal intensity and agent concentration, signal saturation, regional variations in the B1 and B0 fields, breathing motion and registration have impeded the widespread employment of the method in a clinical setting (see also Chapter 3).

The significance of perfusion quantification has been stressed before (Section 3.4). Briefly, in patients with multiple-vessel Coronary Artery Disease, where the perfusion reserve is often globally reduced, a qualitative or semi-quantitative evaluation that detects only regional differences of perfusion reserve is inadequate for determining the severity of the disease [79; 101]. The same holds for patients who have microcirculatory dysfunction (syndrome X) and chest pain, where quantitative perfusion imaging could assist in the diagnosis of the disease [80; 83].

However, studies that adopted quantitative methods to analyze perfusion [79–81] either use no parallel imaging or restrict it in the spatial domain. As a result, the exams exhibited limited spatial resolution and coverage, i.e. 60–90 phase-encodes for a FOV$_y$ of $\sim$250 mm and up to 3 slices, respectively, and thus did not profit from the advantages high resolution and coverage can offer [134].

In this chapter we investigate whether quantification methods could successfully be employed when acquisition and reconstruction are performed using the methods described in Chapter 4, in particular *k-t* SENSE and its derivatives. The interest originates from the fact that images reconstructed using those methods could potentially suffer from temporal blurring when the acceleration factors exceed certain limits (Chapters 5 and 7). Using computer simulations the optimal acceleration factor for each of the reconstruction techniques mentioned above was determined and the different quantitative analysis methods were evaluated. Finally, initial results of quantitative, accelerated myocardial perfusion in humans are presented.

8.1 Theory

Perfusion Quantification

The central volume principle, described in Section 3.4, provides a theoretical basis to calculate blood flow from perfusion images. According to this theory, the amount of tracer $q(t)$ in a region of interest (ROI), e.g. in the myocardium, is (Eq. 3.4):

$$q(t) = F \cdot R(t) \otimes c_{in}(t) = R_F(t) \otimes c_{in}(t) \tag{8.1}$$

where F is the flow rate, $R(t)$ the impulse residue function, $R_F(t)$ the flow-weighted impulse residue function and $c_{in}(t)$ the input contrast concentration, also referred to as arterial input function (AIF), which can be calculated from the signal time course in the left-ventricular (LV) blood pool. The central volume principle states that the flow F is equal to the initial amplitude of the impulse residue function (Eq. 3.7)

$$F = R(t = 0) \tag{8.2}$$

As such, it can be calculated after deconvolution of the measure tissue residue curve $q(t)$ with the arterial input function $c_{in}(t)$.

As explained in Section 3.4, robust deconvolution analysis can be performed either by assuming that the impulse residue function can be modeled by a known function, e.g. Fermi function, or in a model-independent fashion, e.g. by using Singular Value Decomposition (SVD).

Another way to approach this problem is by transforming Eq. 8.1 into the Fourier domain [157]. There, convolution becomes multiplication:

$$Q(f) = R_F(f) \cdot C_{in}(f) \tag{8.3}$$

where f denotes frequency. Using this equation, the frequency domain representation of the tissue residue function and subsequently the flow rate F can be calculated.

k-t SENSE and *k-t* PCA

k-t SENSE, described in detail in Section 4.4, accelerates imaging by sparsely sampling data in the *k-t* space. The equation that describes the reconstruction reads (Eq. 4.50):

$$\boldsymbol{\rho} = \Theta E^H (E\Theta E^H + \lambda\Psi)^{-1} \boldsymbol{\rho}_{alias} \tag{8.4}$$

In this equation, $\boldsymbol{\rho}_{alias}$ is the vector containing all sampled *k-t* space values from all coils, while $\boldsymbol{\rho}$ contains the reconstructed image values. E refers to the encoding matrix, Θ to the signal covariance matrix and Ψ to the noise covariance matrix.

k-t PCA as well as compartment-based *k-t* PCA (Chapter 7) extend *k-t* SENSE by transforming the training data from the *x-f* domain to a coefficient *x-pc* domain. As described in that chapter, the aliasing in those two cases is solved using a transformed version of Eq. 8.4.

As alluded before, $\boldsymbol{\rho_{alias}}$ is a representation of the Fourier transformed imaged object after sampling:

$$\boldsymbol{\rho_{alias}} = W \cdot FT \cdot \boldsymbol{m} \tag{8.5}$$

where W is a binary sparsifying pattern representing the sampled phase encodes, FT is the Fourier transform matrix and $\boldsymbol{m}$ is the imaged object.

Considering Eq. 8.4 and 8.5, one concludes that a reconstruction using either *k-t* SENSE or *k-t* PCA is equivalent to the application of a filter H on the imaged object $\boldsymbol{m}$:

$$\boldsymbol{\rho} = H \cdot \boldsymbol{m} \tag{8.6}$$

The filter H will be referred to as *k-t* filter hereafter.

The effect of *k-t* SENSE or *k-t* PCA on perfusion quantification can be described by the following equation:

$$H_{ROI}(f) \cdot Q(f) = R_F(f) \cdot H_{AIF}(f) \cdot C_{in}(f) \tag{8.7}$$

where $H_{ROI}(f)$ described the *k-t* filter applied on the ROI under consideration, i.e. on the myocardium, and $H_{AIF}(f)$ the *k-t* filter on the AIF, i.e. on the LV blood pool.

If one assumes that the two *k-t* filters are equal, then it is sufficient to employ one of the methods described in this section in order to recover $R_F(t)$. However, since the two regions of interest –myocardium and LV blood pool– present different dynamic responses, *k-t* SENSE or *k-t* PCA will reconstruct those differently. In the following, we investigate using simulations how the two *k-t* filters affect perfusion quantification when *k-t* SENSE and the two *k-t* PCA variants are employed. Then we present initial results of quantitative, accelerated myocardial perfusion in humans.

8.2 Materials and Methods

Numerical Phantom

A numerical phantom was used as a basis for the computer simulations. The phantom was generated from an actual 3D perfusion scan and its sensitivity map (six-channel coil array). The reconstruction matrix was 150$\times$ 150 $\times$10 with 30 dynamics. Perfusion curves for the different anatomical regions were extracted from the same scan and, after correcting for the signal saturation in the LV blood pool using an empirical method, intensity variations in the model were simulated accordingly. The flow rate for this model was 3.2 ml/min/g, simulating a hyperemic myocardium. Uncorrelated Gaussian noise was added to to the real and imaginary channels of each coil, such that the combined fully sampled image had a typical SNR value of 30 [120] on the septal wall during signal peak. The numerical phantom is is depicted in Fig. 8.1.

Simulations

Three series of simulations were performed based on the phantom described above. The first series investigated the effect of *k-t* acceleration using all three reconstruction methods mentioned above on the arterial input function (AIF) and the signal intensity-time (SI) curves. For this purpose, the data set was decimated to simulate a range of acceleration

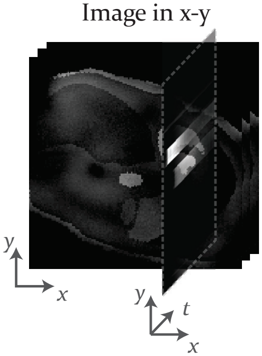

FIGURE 8.1 *The numerical phantom used for the simulations.*

factors (four values between 3× and 10×) and reconstructed using 11 training profiles along the k$_y$ direction and 7 profiles along the k$_z$ direction, resulting in a net acceleration of 2.7-7.1×. For the two *k-t* PCA variants the reconstructions were performed using 12 Principal Components (PCs) [132]. Quantifiable features of temporal fidelity for this series were the baseline, the maximum upslope and the peak signal intensity. The flow rate values were also calculated using two different deconvolution strategies, i.e. Fermi fitting and model-independent deconvolution using Singular Value Decomposition (SVD), and the relative perfusion error was used as a measure of data fidelity. In order to exclude any random error due to noise, we perform the aforementioned experiments 10 times adding different noise each time with the same SNR of 30.

The objective of the second series of simulations was to decouple the effect of *k-t* acceleration on the AIF and the SI curves by assuming either that a) the true AIF and the *k-t* reconstructed SI curves or b) the *k-t* reconstructed AIF and the true SI are used for perfusion quantification. In this manner, one can determine whether the two k-t filters, $H_{AIF}(f)$ and $H_{ROI}(f)$, have a similar effect on the AIF and the myocardial SI, respectively, and in what extent. Again, to avoid random errors, the experiment was repeated 10 times with different added noise.

Finally, considering that the *k-t* reconstruction methods accelerate imaging at the expense of noise enhancement, the dependency of the flow rate error on the signal-to-noise ratio (SNR) was investigated. To this end, we varied the SNR between 10 and 50 (5 values) on the numerical phantom, performed reconstruction and quantification using the above-mentioned methods and calculated the relative perfusion error.

For all three series of simulations the following steps were taken: First, the myocardium and the left ventricular blood pool (LV) were segmented out of the reconstructed data. Then signal intensity-time curves were extracted from the six myocardial sectors and the LV for all slices. Subsequently, the signal intensities were converted to contrast agent concentrations in an empirical manner, by first subtracting and then dividing by the baseline. The concentration units using this method are arbitrary. Finally, the flow rate was calculated using a model-based (Fermi fitting) [88] and a model-independent (SVD) [96] based deconvolution method.

In vivo experiments

In vivo experiments for perfusion quantification were carried out on a male patient (age 71) with suspected coronary artery disease. The subject gave informed consent according to the institutional policy.

Perfusion images were acquired with 10-fold undersampling on a 3T Philips Achieva scanner (Philips Healthcare, Best, The Netherlands) with a 6-element phased array, using a WET saturation pulse [62] and a gradient echo sequence. Imaging parameters included TR=1.86 ms, TE=0.76 ms, flip angle = 15°, FOV 380×361mm^2, saturation prepulse delay=150 ms, acquisition time per heart beat=300ms, 75% partial Fourier acquisition in k$_y$ and k$_z$, acquired slices=10, slice thickness=10mm, dynamics=30, expiration breathhold. The acquisition matrix was chosen such that the in-plane resolution was equal to 2.3×2.3mm^2. For an acquisition matrix of 164×147, acquired using partial Fourier and the elliptical shutter described in Chapter 7, 11 k$_y$ and 7 k$_z$ training profiles a net acceleration of 7.1 was achieved.

The patient underwent a vasodilator-stress and rest CMR perfusion exam. For the stress acquisition, adenosine was administered intravenously at a dose of 140 μg/kg/min for 4 minutes. At 3 minutes of infusion, an intravenous bolus injection of 0.1 mmol/kg gadopentetate dimeglumine, (Magnevist, Bayer Schering Pharma, Berlin, Germany) was given via a power injector (Spectris Solaris, MEDRAD, Minneapolis, USA) at a rate of 4 ml/s, followed by a 20 ml saline flush. After a 20 minute waiting period for contrast agent washout, an identical perfusion scan was repeated at rest. To correct for the signal drop-off due to B1 inhomogeneities, the final images were corrected using the sensitivities calculated during a separate scan. The partial Fourier data were reconstructed using homodyne reconstruction [144]. The patient went on to invasive X ray coronary angiography, where it was diagnosed that, despite a slightly delayed filling of the left anterior descending (LAD) artery, the patient had no significant stenosis.

To obtain accurate quantitative perfusion information signal intensity differences due to B1 field inhomogeneities have to be corrected for. Since the reconstruction was performed using auto-calibrated sensitivities [143], this correction was performed in a post-processing step using sensitivities calculated from an additional low-resolution scan. Division of the reconstructed images by the sum-of-squares of these sensitivities results in homogeneous signal distribution over the myocardium.

Then the signal intensities were converted to contrast agent concentrations. The conversion was based on the knowledge of the myocardial and blood pool T1 values acquired during a separate scan and the M_0 signal derived from the baselines of the perfusion scans using those T1 values. The equations used for this conversion were given in Chapter 3 (Eqs. 3.31 and 3.32).

Due to absence of “ground truth” non-accelerated data in the *in vivo* experiments, the acquired images were evaluated visually and the perfusion values derived after quantification were checked for conforming to the values found in the literature.

8.3 Results

Numerical Phantom

In Fig. 8.2a-c the AIF curves calculated from a midventricular slice of a 3D model are illustrated for *k-t* SENSE, *k-t* PCA and compartment-based *k-t* PCA, respectively, for all four acceleration factors. In Fig. 8.2d-f the relative errors with respect to the reference are plotted for the baseline, the maximal upslope and the maximum. Mean and standard deviation error values are plotted in percent. It can be seen that *k-t* SENSE reconstructs

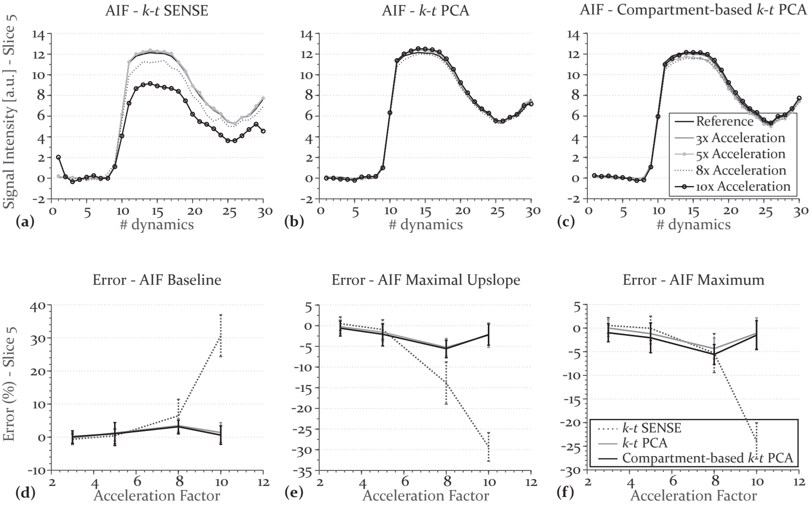

FIGURE 8.2 *Computer simulations. The AIF as reconstructed using (a) k-t SENSE (b) k-t PCA and (c) compartment-based k-t PCA for four acceleration factors. Relative error of the calculated AIF (d) baseline, (e) maximal upslope and (f) maximum values for the three reconstruction schemes and four acceleration factors. The error bars indicate mean value and standard deviation (the length of the bar is twice the standard deviation). The significant underestimation of the maximal signal intensity for 8x and 10× undersampling and the temporal filtering during the first dynamics of the AIF for 10× acceleration are to be seen in the k-t SENSE reconstructed curves. These effects are eliminated by the two k-t PCA methods.*

the AIF correctly for accelerations up to 5×, but results in high errors for 8× and 10× acceleration, with ~30% overestimation of the baseline and ~30% underestimation of upslope and signal intensity maximum for 10× undersampling. Contrary to that, the two *k-t* PCA variants result in correct reconstructions for all accelerations, with minor overestimation of the baseline (~5%) and underestimation of maximal upslope and maximum intensity (~5%), when a factor of 8 was used.

In Fig. 8.3a-c the signal intensity-time curves from the septal wall of a midventricular slice of a 3D model are illustrated for *k-t* SENSE, *k-t* PCA and compartment-based *k-t* PCA, respectively, for all four acceleration factors. In Fig. 8.3d-f the relative errors for the baseline, the maximal upslope and the maximum of the curves are plotted, while in Fig. 8.3g and h the corresponding errors for the flow rate using Fermi fitting and SVD deconvolution are given. It can be seen that *k-t* SENSE reconstructs the curves correctly for accelerations up to 5×, but results in high errors for 8× and 10× acceleration, with the curves suffering from temporal blurring during their first dynamics and noise enhancement throughout the experiment. It should be noted here that the baseline calculation was performed after excluding the first dynamic, which is usually severely overestimated by *k-t* SENSE due to temporal filtering. As it was the case before, the maximal signal intensity for an acceleration factor of 10 is underestimated (~12%). Moreover, using the AIF presented before to perform model-dependent and model-independent deconvolution, the flow rates are overestimated by ~10% and ~20%, respectively. Different observations can be made for the *k-t* PCA reconstructed curves: baseline, maximal upslope and intensity are represented correctly for all acceleration factors, with mean errors below 5%. Important exception is the 8× and 10× accelerated conventional *k-t* PCA reconstruction, which results in temporal filtering at the beginning of the upslope and thus upslope errors in the range of 10-20%. This temporal filtering results in underestimation of the flow rate by ~5% and ~20% for 8× and 10× acceleration for both deconvolution methods. It can be seen that the compartment-based *k-t* PCA corrects for this particular issue and improves the error values,

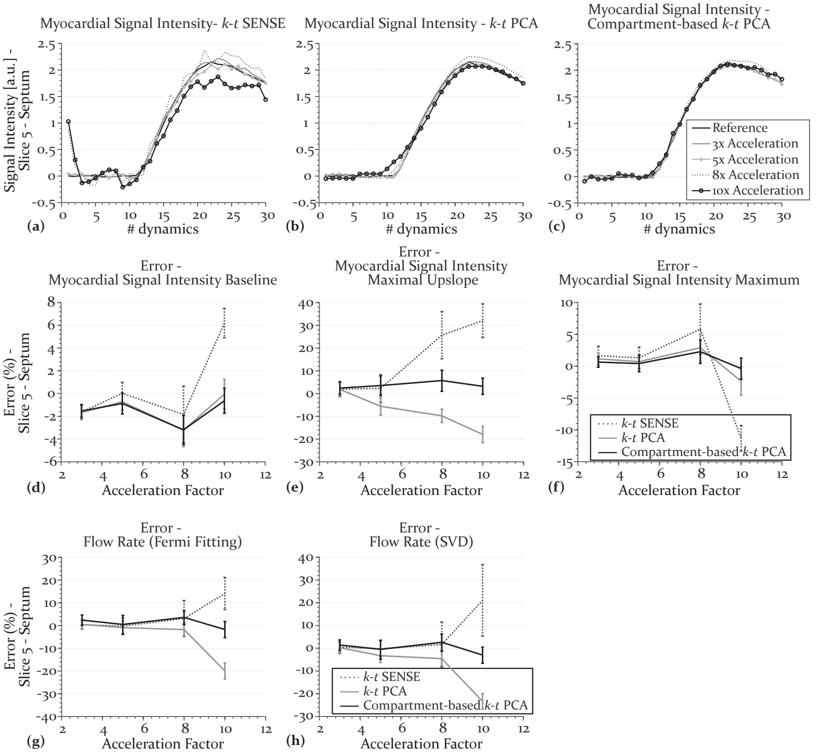

Figure 8.3 *Computer simulations. The signal intensity-time curves as reconstructed using (a) k-t SENSE (b) k-t PCA and (c) compartment-based k-t PCA for four acceleration factors. Relative error of the calculated AIF (d) baseline, (e) maximal upslope, (f) maximum values and flow rates using (g) Fermi fitting and (h) SVD deconvolution for the three reconstruction schemes and four acceleration factors. As before, the error bars indicate mean value and standard deviation (the length of the bar is twice the standard deviation). The significant underestimation of the maximal signal intensity for 8× and 10× undersampling and the temporal filtering during the first dynamics of the AIF for 10× acceleration resulting in overestimation of the flow rate are seen in the k-t SENSE reconstructed curves. Temporal filtering resulting in underestimation of the flow rate also affects k-t PCA for 10× undersampling. These effects are eliminated by the compartment-based k-t PCA method.*

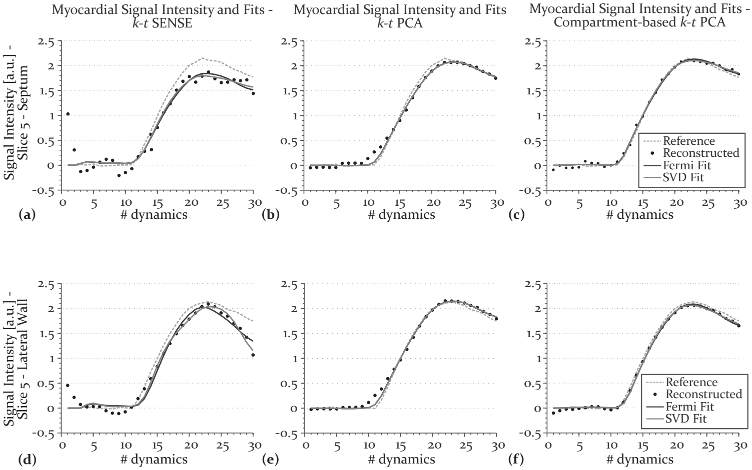

FIGURE 8.4 *Computer simulations. Signal intensity-time curves extracted from the septal (upper row) and the lateral wall (lower row) for the three reconstruction methods under consideration along with the corresponding fitted curves using Fermi fitting and SVD deconvolution*

i.e. <3% underestimation of the baseline, <5% overestimation of maximal upslope and signal intensity and minor (<5%) flow rate estimation errors. It should be noted again, that the highest errors for the compartment-based *k-t* PCA are generally visible for an undersampling factor of 8.

Figure 8.4 shows the contrast concentration curves along with the fit curves for the three reconstructions under consideration and for two myocardial regions, i.e. septum and lateral wall. Except for the observations made in Fig. 8.3a-c, one can note the reduced temporal filtering in the *k-t* SENSE reconstruction of the lateral wall compared to the one of the septum and the corresponding reduced discrepancy with respect to the reference curves. It is also seen that any deviations from the reference curves during the first dynamics due to temporal filtering or signal contamination are corrected for by the fitting process. With the exception of the lateral wall when *k-t* SENSE is employed, where SVD performs slightly worse than Fermi fitting, it is seen that the two fitting procedures are very similar to one another.

In order to have an overview of the flow rate errors for the different reconstruction methods, their mean values for eight slices and for 5× and 10× accelerations are presented in Fig. 8.5 as bull's-eye plots. The following can be observed: For 5× undersampling, all three methods result in relatively low flow rate errors (in the 10% range for *k-t* SENSE and in the 5% range for the *k-t* PCA variants), with *k-t* SENSE and compartment-based *k-t* PCA tending to overestimate flow and conventional *k-t* PCA having the opposite tendency. For 10× undersampling both *k-t* SENSE and conventional *k-t* PCA fail to calculate flow rates accurately, the former overestimating flow up to 30% in the septal region, while overestimating it by up to 50% in the lateral region. For this acceleration factor conventional *k-t* PCA consistently underestimates flow rates, with the higher error (~30%) corresponding to the septal and lateral regions. On the other hand, the compartment-based variant is more accurate with estimates lying mostly within the 5% limit of the reference values. This is also reflected in the uniformity of the distributions of flow rate error values throughout all myocardial sectors.

Another related observation is that, with the exception of *k-t* SENSE, the two deconvolution methods give approximately the same error. For *k-t* SENSE and for high accelerations the model-based deconvolution results in slightly lower errors compared to the model-independent deconvolution, although high in both cases.

The results of the second series of simulations are illustrated in Fig. 8.6. Figures 8.6a-c depict the relative flow rate error calculated using Fermi fitting as a function of the acceleration factor for the three reconstruction methods, respectively, using the true and the reconstructed AIF and SI curves in an alternating manner. Figures 8.6d-f depict the same errors, this time using SVD to perform deconvolution. In order to describe these figures, we use as a reference the error curves derived using the reconstructed AIF and SI curves, shown in black. It is seen that assuming a known AIF results in lower flow rates for all reconstructions and

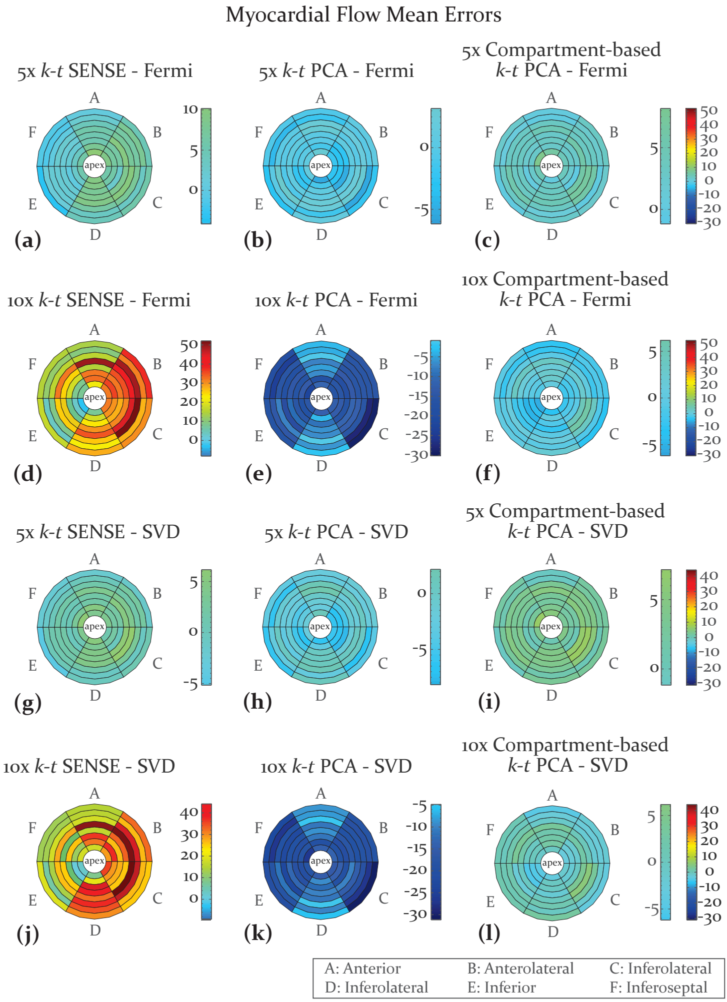

FIGURE 8.5 *Computer simulations. Bull's-eye plots of the relative error for the three reconstruction and two deconvolution methods for 5× and 10× undersampling. The upper two rows correspond to the first deconvolution method (Fermi fitting), whereas the lower two rows to the second deconvolution method (SVD). It should be noted that the scaling of the colorbars for each of the two groups mentioned is the same, shown at the right end of the figure. The leftmost column refers to k-t SENSE, the middle to the conventional k-t PCA and the rightmost to the compartment-based k-t PCA reconstruction. Finally, the first and third rows represent the errors for 5× acceleration, while the second and fourth rows the errors for 10× acceleration.*

acceleration factors, with a more dramatic effect in the case of *k-t* SENSE, where the error even changes sign (*k-t* SENSE now underestimates flow). Contrary to that, assuming known SI curves results in higher flow rates than the reference. As such the reference error curve (black line) lies always between the other two curves. A general observation that refers to all three reconstructions is that the standard deviation of the error is lower using either the known AIF or SI curves. Furthermore, assuming correct SI curves for the two *k-t* PCA reconstructions results in lower absolute flow rate errors, compared to the case when known AIFs are assumed. Again, it can be seen that, with the exception of k-t SENSE at 10× undersampling, the two deconvolution procedures result in very similar results.

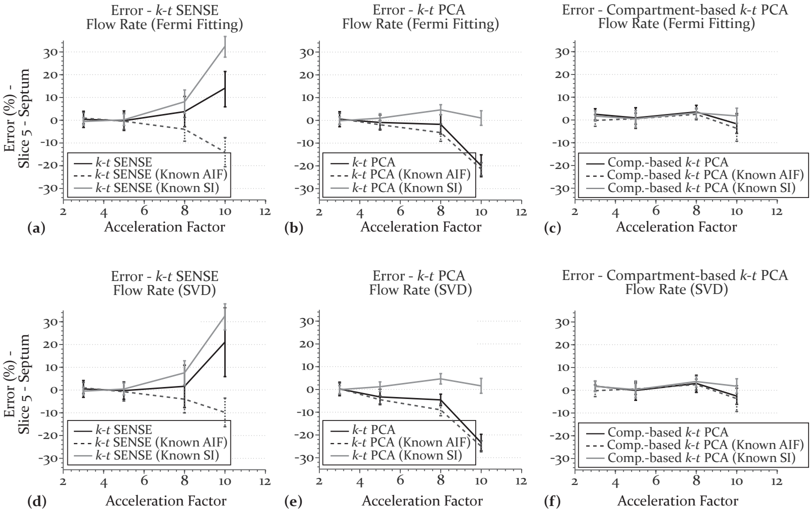

FIGURE 8.6 *Computer simulations. Relative flow rate error using Fermi fitting (upper row) or SVD deconvolution (lower row) for k-t SENSE, k-t PCA and compartment-based k-t PCA (left to right columns, respectively). The black line corresponds to the errors calculated using the reconstructed AIF and SI curves, whereas the gray line corresponds to the case where the known SI curves are assumed. The dashed line refers to the error when the correct AIF and the reconstructed SI curves are used to calculate flow rates.*

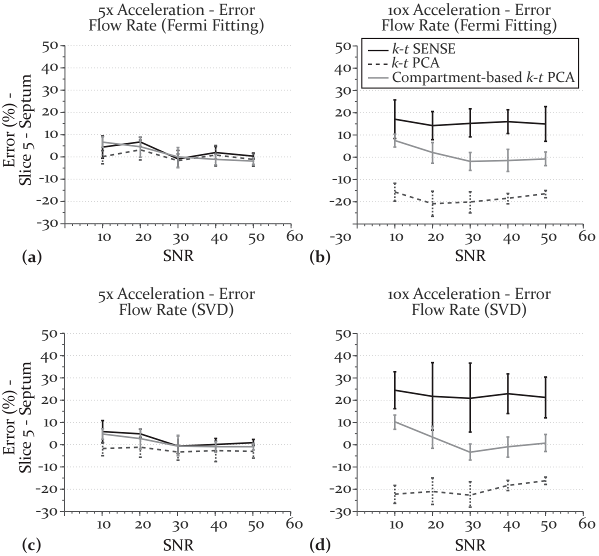

FIGURE 8.7 *Computer simulations. Relative flow rate error using Fermi fitting (upper row) or SVD deconvolution (lower row) for k-t SENSE (black line), k-t PCA (dashed-line) and compartment-based k-t PCA (gray line) as a function of the model SNR. The error for 5× acceleration (left column) lies within the 10% margin for all reconstructions and SNR values. For 10× acceleration, k-t SENSE significantly overestimates flow, whereas k-t PCA consistently underestimates it. Compartment-based k-t PCA results in more accurate flow values, especially for SNR values beyond 20 (-5% to 5% error values). For easy reference the y-axis has been scaled equally in all subfigures.*

In Fig. 8.7 the dependency of the flow rate error on the SNR is presented. For 5× undersampling, all three reconstructions result in low errors with values between -5% and 5% for SNR larger than 30. It is also seen that the standard deviation tends to be lower with increasing SNR. For 10× acceleration, *k-t* SENSE significantly overestimates the flow rate (15-20%), whereas *k-t* PCA underestimates it by approximately the same percentage. Compartment-based *k-t* PCA calculates flow accurately, especially for SNR values beyond 20. A general observation for all reconstruction and

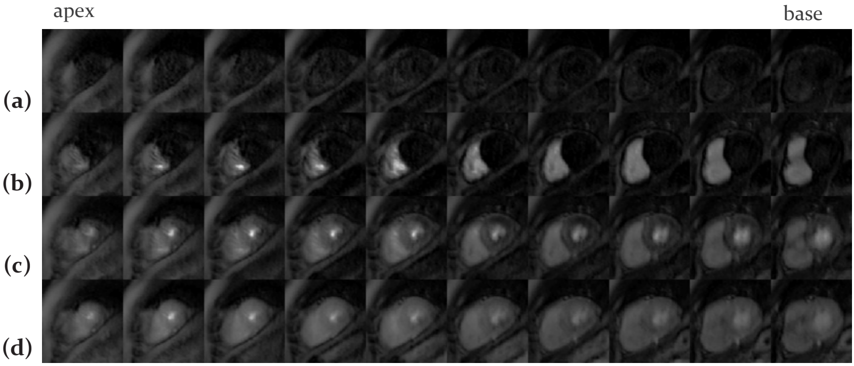

FIGURE 8.8 *In vivo data. Eight slices of the 3D volume before bolus arrival (a) and during contrast uptake in the RV (b), the LV(c) and the myocardium (d) are shown. The slight delay in the uptake on the anterior wall is partly visible.*

deconvolution methods and for both acceleration factors examined, is that the flow rate error dependency on SNR is relatively weak. In other words, except for a tendency for lower standard deviation values, no dramatic error reduction can be observed with increasing SNR.

In vivo Experiments

Figure 8.8 shows representative *k-t* PCA reconstructed perfusion images from the examined subject before contrast arrival (Fig 8.8a) and during RV, LV and myocardial enhancement (Fig. 8.8b, c, d, respectively). It can be seen that the images using this reconstruction method exhibit high image quality, sufficient to reveal the delayed contrast uptake in the anterior myocardial wall. This delayed uptake was verified by the invasive X-ray coronary angiography, which, as mentioned in section 8.2, showed late filling of the LAD.

In Fig. 8.9, the AIF (dashed line) and SI curves (black line) for a midventricular slice and for two myocardial regions (septal and lateral wall) after conversion to concentrations are presented. Overlaid on the black line are the two fitted curves, one using Fermi and the other SVD

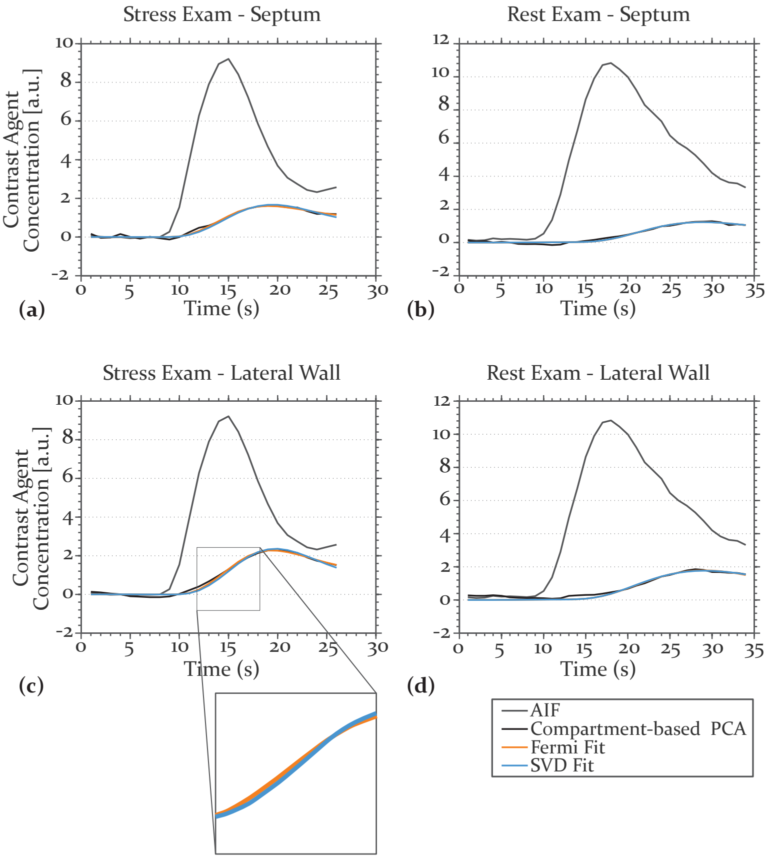

FIGURE 8.9 *In vivo data. Concentration Curves for the blood pool and the myocardium along with the fitted curves derived for the latter during stress (left column) and rest (right column). The upper row corresponds to the septum, whereas the lower row to the lateral wall.*

deconvolution. Despite the similarity, small differences between the two fitted curves can be observed. For example in the lateral region (embedded figure) the upslope of the SVD fit is larger than that of the Fermi fit. A final observation is that the rest exam has a longer duration in comparison to the

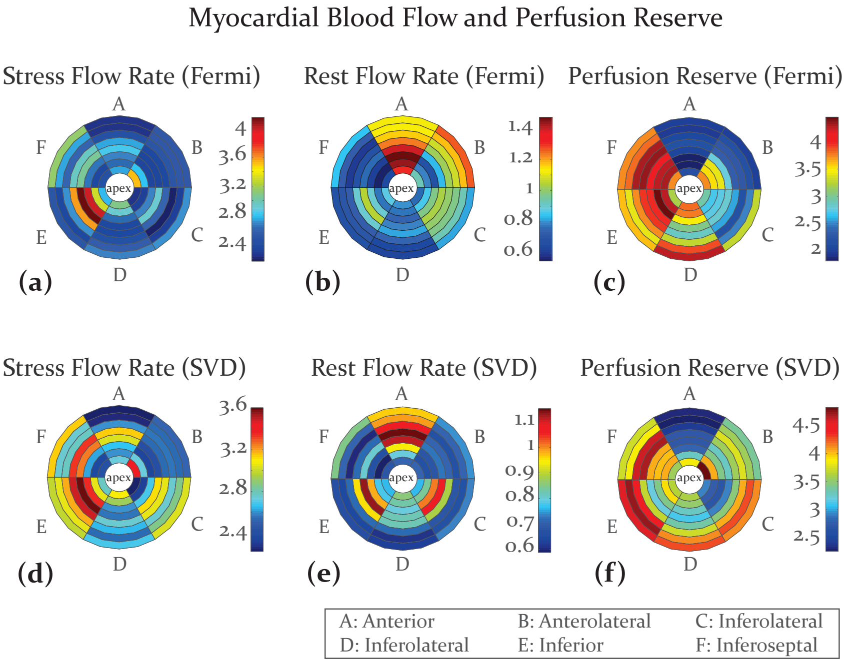

FIGURE 8.10 *In vivo data. Bull's-eye plots for absolute flow rate values for stress (left column) and rest (middle column) perfusion. The corresponding Myocardial Perfusion Reserve (MPR) is also shown (right column). The upper row refers to flow rate calculations using Fermi fitting, while the lower row to calculations using SVD deconvolution.*

stress exam and results in less steep curves both in the left ventricle and on the myocardium.

The bull's-eye plots presented in Fig. 8.10 depict the absolute flow rate values for the different slices and sectors of the 3D volume reconstructed. The leftmost column represents flow rates corresponding to the stress exam of the patient using Fermi (upper row) and SVD (lower row) deconvolution. It is seen than the flow values obtained are between 2.4 and 4 ml/min/g for the former deconvolution method, while they are between 2.4 and 4 ml/min/g for the latter. Although there is a trend for reduced flow rate in the anterior and anterolateral region, large fluctuations can be observed between different slices and sectors. The same can be said for the rest flow rates presented in the middle column. Here the flow rates are between 0.6 and 1.4 ml/min/g with Fermi resulting in slightly larger values. The rightmost column shows bull's-eye plots representing the myocardial perfusion reserve corresponding to the two deconvolution methods. Its values lie approximately between two and four for Fermi and between 2.5 and 4.5 for SVD fitting. The lowest perfusion reserve values in both cases correspond to the anterior and anterolateral regions, where, as mentioned above, the delayed LAD filling is observed.

8.4 Discussion

Aim of the work presented in this chapter was to investigate the effect of spatiotemporal acceleration on the quantification results of myocardial perfusion. Using numerical simulations we could explore the acceleration limits for the three reconstruction methods presented in the previous chapters, i.e. *k-t* SENSE, *k-t* PCA and compartment-base *k-t* PCA.

As it was shown in the Results section, for acceleration factors up to 5×, all three methods reconstruct perfusion images with adequate fidelity (flow rate errors within the 5% range). The flow rate errors are low for conventional and compartment-based *k-t* PCA also for 8-fold acceleration, while for 10× undersampling only the latter gives images with sufficient fidelity.

The underestimation of the peak intensity of the AIF in the *k-t* SENSE reconstructed images for high accelerations results in substantial overestimation of the flow rate values derived. However, the simultaneous underestimation of the peak of the myocardial curves alleviates this effect. This is seen in the following two cases: First, in the lateral wall, where the maximum is only slightly underestimated compared to the septal wall, the overestimation of the final flow rates is larger than in the septum (see Fig. 8.5). Secondly, in the simulations where the actual AIF or SI are employed for the flow calculation (Fig. 8.6) it is seen that the overestimation is larger when the known SI is used, whereas the error takes negative values when the AIF is correctly calculated.

This latter observation is also valid for the other two reconstruction schemes, although in a much lesser extent due to the overall lower errors. In other words, the underestimation of the maximal intensities in the AIF or in the concentration curves have opposite effects and result in lower absolute errors with respect to the reference. This is seen in Fig. 8.6, where the flow rate errors calculated from the reconstructed images (black lines) always lie below the errors calculated using the correct SI curves (gray line) and beyond those calculated using the correct AIF (dashed line).

It should be stated at this point that the signal contamination and the increased temporal filtering and noise in *k-t* SENSE for high accelerations results in large fit errors, which in turn lead to a large variation of the baseline values and maxima derived. As such and taking into consideration the fit curves presented in Fig. 8.4, the temporal filtering and signal contamination during the first dynamics are not present after fitting, but affect indirectly and potentially in a severe manner the subsequent calculations, due to misestimations of baselines and upslopes. This is also reflected in the large standard deviation of the flow rate errors for these high undersampling factors.

The underestimation of the flow rates for the conventional *k-t* PCA and for 10× acceleration is a consequence of the temporal filtering present in the corresponding concentration curves. Since such an effect is not present in the correctly derived AIFs, the final flows are underestimated up to 30%, particularly for those regions which are most affected by temporal filtering, i.e the septum and the lateral wall (see Fig. 8.5). Contrary to that, the compartment-based *k-t* PCA does not suffer from any of the above mentioned artifacts and results in low flow rate errors (-5% to 5%).

In order to perform the comparisons presented in this chapter, the numerical phantom dataset had to be extended to 32 dynamics for 8× acceleration. This was done by replication of the last two dynamics before decimation and by their cropping after reconstruction. It is believed that the slight deviations of the values of certain quantifiable features for 8×

from the general tendency, e.g. baseline or maximal intensity in Fig. 8.3, are exactly due to this extension along the temporal dimension.

Another interesting observation is the weak dependency of the flow rate errors on the SNR, as this was expressed in Fig. 8.7. It is seen that with the exception of compartment-based *k-t* PCA, where the error is decreasing as a function of the SNR, a trend reported also in Chapter 7, the tendency of decreasing error with increasing SNR values is only slight for the other reconstruction methods. This weak dependency is attributed to the effects of the fitting performed in order to calculate flow rates. This only applies partly to compartment-based *k-t* PCA, which, as mentioned in the previous chapter, is affected by low base SNR values (~10), since the definition of the compartments is then compromised.

The *in vivo* exams demonstrated that absolute blood flow quantification in 3D perfusion imaging is feasible using compartment-based *k-t* PCA with rest and stress values lying within the values found in the literature [158]. The same can be said for the Myocardial Perfusion Reserve (MPR) values, which also agree with what has been reported in the past. Moreover, the locations with low MPR values correspond to regions that were identified in the X-Ray angiography as having delayed contrast uptake.

Despite the progress, several remaining issues still render absolute blood flow quantification a particularly difficult task. First drawback is the additional scans that need to be performed to correct for the B1 inhomogeneities and to perform the conversion of signal intensities to contrast agent concentrations. Secondly, the sensitivity of the fitting algorithms to signal variations and the vulnerability of the baseline estimates to temporal filtering and noise impede a robust quantification. This can be seen in the fluctuation of the absolute blood flow values during stress and rest for regions which are adjacent to each other and which are not expected to present high variations. Based on the results presented in Fig. 8.10, one can state that with the current workflow the perfusion reserve values are more reliable compared to the absolute flow rate values.

A clear limitation of the work presented in this chapter is the fact that the method has been tested on only one patient. In spite of the positive results, this technique warrants further validation in a larger study. Considering the necessity for a more streamlined and robust procedure, we can say that flow quantification in 3D is a promising method to assess myocardial perfusion without compromising spatial resolution or coverage.

CHAPTER 9

DISCUSSION

Improving the diagnostic performance of perfusion MR imaging can have a strong impact on the therapeutic management and consequently on the prognosis of patients with coronary artery disease. Having this as an aim, several technical developments have been proposed and employed in the past. A number of those have occurred in the area of MR hardware (higher field strengths, faster gradient systems, improved receiver coils), while others concentrated on pulse sequence design or new contrast agents. In spite of the progress achieved, the fundamental requirements of perfusion MRI could not be fully met, mainly due to low image acquisition speeds. These requirements, namely the high spatial and temporal resolution as well as the large cardiac coverage, must be fulfilled if perfusion imaging is to be widely adopted in a clinical setting.

It should be stressed here that, in comparison to other cardiac MR imaging techniques, perfusion imaging presents one distinctive feature that renders its employment particularly challenging. That is, it is a first-pass contrast-enhanced method, which implies that (a) there is only a very limited time-window during which the acquisition can be performed and (b) it cannot be performed repeatedly until potential issues are resolved. Image reconstruction techniques based primarily on parallel imaging addressed those issues and partly fulfilled the aforementioned contradictory requirements. Nonetheless, the necessity for higher resolution and larger coverage without compromising temporal fidelity dictates further acceleration and more sophisticated reconstruction methods.

9.1 Contribution of the Thesis

The first reconstruction method presented in this thesis is based on the *k-t* SENSE framework and proposes the application of SENSE imaging to the training data in order to achieve higher spatial resolution without compromising acquisition efficiency. The increased spatial resolution of the training dataset results in reduced temporal blurring and signal contamination when high acceleration factors are employed. This modification allows for up to 8× undersampled multi-slice 2D acquisitions at the highest resolution reported up to this point (1.1×1.1 mm^2), without compromising image quality. Improvement in the resolution of the training data comes at the expense of increased noise, a result of the nonorthogonality of coil encoding. As it was shown here, this increased noise propagates through the final *k-t* SENSE reconstruction. However, this effect is significant only when the SNR of the perfusion image is very low. Otherwise the proposed method with a 2× and 3× SENSE accelerated training results in consistently better reconstructions than the conventional *k-t* SENSE method.

The clinical performance of this technique was demonstrated in a study comprising 20 patients. The overall diagnostic accuracy of perfusion imaging using *k-t* SENSE with SENSE training was better compared to previously published studies and had an area under the receiver-operator curve of 0.94. The increased spatial resolution achieved could lead to higher specificity values due to reduced subendocardial dark rim artifacts and in turn less false positive interpretations.

Considering the necessity for larger coverage, in this work a technique to reconstruct highly accelerated, high-resolution 3D perfusion imaging is further proposed. This technique, based on the *k-t* PCA framework, an extension of *k-t* SENSE, makes use of prior knowledge with respect to the temporal evolution of the first-pass experiment and reconstructs perfusion image series of high quality. A fundamental step of the proposed algorithm is the definition of compartments within the 3D volume imaged, which are then used to eliminate voxels that are severely affected by partial-volume artifacts. This process ameliorates temporal fidelity issues associated with spatiotemporally accelerated reconstruction methods, especially at such accelerations (10×) and spatial resolutions (2.3×2.3 mm^2) as the ones employed here. Another advantage of the proposed reconstruction method is the relatively short acquisition window achieved (225 ms). Within such acquisition windows stress exams are feasible without severe artifacts induced by cardiac motion.

Particular emphasis has been given on the significance of the quantitative analysis of perfusion images. As stated beforehand, such an analysis is crucial for cases where a qualitative assessment is insufficient, such as for patients suffering from multiple-vessel coronary artery disease or for patients with microcirculatory disease. In this perspective, and considering the necessity for employing spatiotemporally accelerated reconstruction techniques, an analysis of the effects of acceleration on quantification is imperative. The interest originates from the fact that *k-t* SENSE and its derivative methods, as mentioned before, have a tendency to compromise temporal fidelity.

A reconstruction using either *k-t* SENSE or *k-t* PCA is equivalent to the application of a filter on the imaged object. As it was shown all reconstruction methods discussed in this thesis can be employed for blood flow quantification up to an acceleration factor of 5. *k-t* PCA and particularly its compartment-based variant can exceed this limit without compromising image quality or the subsequent quantification. Based on the simulations performed, it can be said that, up to a certain point, an underestimation of the arterial input function (AIF) due to temporal filtering acts in a competing manner to a potential underestimation of the concentration curves. Nevertheless, for 10-fold undersampling we could observe a clear tendency of *k-t* SENSE to overestimate flow rate values. The opposite can be said for the conventional *k-t* PCA, whereas compartment-based *k-t* PCA eliminates these issues.

The *in vivo* experiment performed on a patient with suspected coronary artery disease is a first demonstration of the feasibility of absolute blood flow quantification in a clinical setting. This experiment present further evidence of the complexity of the process and the issues that still need to be addressed to render absolute quantification a method that could be widely used in practice to assess myocardial perfusion.

9.2 Outlook

One of the key issues for future research concerns the compensation for motion in perfusion images. For patients who suffer from ischemic heart disease this is a substantial issue, since they often have severe difficulties holding their breath for the duration of a perfusion exam. Despite the fact that *k-t* PCA is more robust to motion compared to *k-t* SENSE, artifacts induced by large shifts or abrupt translations of the breathhold position can compromise diagnostic accuracy. To address this problem, a more generalized reconstruction framework could be adopted. An example of such a framework is the Generalized Reconstruction by Inversion of Coupled Systems (GRICS) [159], where the required model of motion could be provided by training data.

In view of the improvements attained by introducing prior knowledge in the reconstruction, future research may consider the implementation of further constraints derived by the knowledge of the perfusion mechanism in the heart. This could either be in the direction of imposing hard constraints in the temporal behavior of the system or towards directly incorporating perfusion models, such as the ones used for quantification, into the reconstruction equation. Due to its higher sophistication, the latter could increase the computational burden of the reconstruction algorithm, but it may also conduce to exceeding the acceleration limits reached with the proposed approaches. A significant issue to be taken into consideration in the aforementioned cases is the conservative employment of these models in order to allow for physiologically acceptable deviations from the constraints they impose.

On a related note emphasis should be placed on two more fields of research that attempt to address the clinical need of myocardial perfusion assessment. The first, utilizes the dynamic nuclear polarization (DNP) of ^{13}C in labeled endogenous compounds to increase the NRM signal (typically by a factor of 30,000). The compound injected intravenously could boost the signal-to-noise ratio (SNR) by a significant amount, rendering higher acceleration factors and higher spatial and temporal resolutions feasible. Issues related to the hyperpolarization technique and its efficient application as well as methods to account for the effects of compound depolarization are subjects of ongoing research.

The second field employs conventional MRI techniques to perform quantitative measurements of tissue blood flow with no injection of contrast agent. The method, termed Arterial Spin Labeling (ASL) [160], aims at overcoming certain limitations of the first-pass contrast-enhanced method (e.g. dark rim artifacts, absolute quantification of myocardial blood flow, the potential onset of the “nephrogenic systemic fibrosis”[161]) by using slab-selective and nonselective inversion pulses applied alternately to generate control images (without inversion of out-of-slice blood) and tagged images (with inversion of out-of-slice blood). The two sets of images can then be subtracted from one another to obtain quantification information. Despite its advantages, the application of this technique is limited by its inadequate SNR and by timing restrictions related to cardiac motion. Thus, further work is required to foster its clinical adoption.

APPENDIX A

DERIVATION OF THE RECONSTRUCTION MATRIX

In order to derive the optimal reconstruction matrix, one should minimize the fidelity term Δ (see Section 4.1):

$$F_{opt} = \underset{F}{argmin}(\Delta) \tag{A.1}$$

or its square:

$$F_{opt} = \underset{F}{argmin}(\Delta^2) \tag{A.2}$$

The mean of the fidelity term squared is then equal to:

$$\Delta^2 = \|(FE - I)\|_F^2 \tag{A.3}$$

or, after expanding[1]:

$$\Delta^2 = tr\big((FE - I)^H (FE - I)\big) \tag{A.4}$$

Considering that $tr(AB) = tr(BA)$, Eq. A.4 can be rewritten as:

$$\Delta^2 = tr\big((FE - I)(FE - I)^H\big) \tag{A.5}$$

or

$$\Delta^2 = tr(FEE^H F^H - FE - E^H F^H + I) \tag{A.6}$$

The minimization of Δ^2 is an unconstrained minimization problem. To solve it, it is sufficient to set the derivative of Δ^2 with respect to F equal to zero

$$\begin{aligned} \frac{\partial \Delta^2}{\partial F} &= 0 \\ \frac{\partial\big(tr(FEE^H F^H - FE - E^H F^H + I)\big)}{\partial F} &= 0 \\ \frac{\partial\big(tr(FEE^H F^H)\big)}{\partial F} - \frac{\partial\big(tr(E^H F^H)\big)}{\partial F} - & \\ - \frac{\partial\big(tr(FE)\big)}{\partial F} + \frac{\partial I}{\partial F} &= 0 \\ 2E^H EF - E^H - E^H + 0 &= 0 \end{aligned} \tag{A.7}$$

and solve for F:

$$\begin{aligned} E^H EF &= E^H \\ F &= (E^H E)^{-1} E^H \end{aligned} \tag{A.8}$$

---

[1] It is: $\|A\|_F = \sqrt{\sum_{i=1}^{m} \sum_{j=1}^{n} ||a_{ij}|} = \sqrt{tr(A^H A)}$, where $tr(X)$ is the trace of matrix X.

APPENDIX B

BAYESIAN DERIVATION OF *k-t* SENSE

B.1 Bayesian Reconstruction

In this Appendix, the *k-t* SENSE reconstruction problem, first stated in Section 4.4, is solved from a Bayesian perspective. In this case, the reconstructed image $\boldsymbol{\rho}$ is considered a random variable and the solution is calculated such that the the posterior probability of the occurrence of this solution, given the occurrence of the *k*-space measurement $\boldsymbol{d}$, ($Pr\{\boldsymbol{\rho}|\boldsymbol{d}\}$), is maximized.

Given the imaging process

$$\boldsymbol{d} = E\boldsymbol{\rho} \tag{B.1}$$

an observation $\boldsymbol{d}$ and the prior probability distribution $Pr\{\boldsymbol{\rho}\}$ of the target image $\boldsymbol{\rho}$, Bayesian methods maximize the posterior probability

$$Pr\{\boldsymbol{\rho}|\boldsymbol{d}\} \propto Pr\{\boldsymbol{d}|\boldsymbol{\rho}\}Pr\{\boldsymbol{\rho}\} \tag{B.2}$$

The first right-hand term is called the likelihood function and depends on the imaging model $\boldsymbol{d} = E\boldsymbol{\rho}$. The second term is the prior distribution.

Assuming that $\boldsymbol{\eta} = \boldsymbol{d} - E\boldsymbol{\rho}$ is white Gaussian noise, the probability $Pr\{\boldsymbol{d}|\boldsymbol{\rho}\}$ follows a Gaussian distribution:

$$Pr\{\boldsymbol{d}|\boldsymbol{\rho}\} \propto e^{-\|\boldsymbol{\eta}\|^2} = e^{-\|\boldsymbol{d}-E\boldsymbol{\rho}\|^2} = e^{-\frac{1}{2}(\boldsymbol{d}-E\boldsymbol{\rho})^H\Psi^{-1}(\boldsymbol{d}-E\boldsymbol{\rho})} \tag{B.3}$$

where Ψ is the matrix that describes the covariance between the elements of $\boldsymbol{\eta}$, also known as *noise covariance matrix*.

Similarly, the prior can be written as

$$Pr\{\boldsymbol{\rho}\} \propto e^{-K(\boldsymbol{\rho})} \tag{B.4}$$

without loss of generality.

Combining Eqs. B.2-B.4 we get:

$$Pr\{\boldsymbol{\rho}|\boldsymbol{d}\} \propto e^{-\frac{1}{2}\|\boldsymbol{d}-E\boldsymbol{\rho}\|^2} e^{-K(\boldsymbol{\rho})} = e^{-\left(\frac{1}{2}\|\boldsymbol{d}-E\boldsymbol{\rho}\|^2+K(\boldsymbol{\rho})\right)} \tag{B.5}$$

The posterior is maximized by the maximum a posteriori (MAP) estimate:

$$\begin{aligned}\hat{\boldsymbol{\rho}} &= \underset{\boldsymbol{\rho}}{argmax}(Pr\{\boldsymbol{\rho}|\boldsymbol{d}\}) \\ &= \underset{\boldsymbol{\rho}}{argmin}\big(- logPr\{\boldsymbol{d}|\boldsymbol{\rho}\} - logPr\{\boldsymbol{\rho}\}\big) \\ &= \underset{\boldsymbol{\rho}}{argmin}\big(\frac{1}{2}\|\boldsymbol{d} - E\boldsymbol{\rho}\|^2 + K(\boldsymbol{\rho})\big)\end{aligned} \tag{B.6}$$

k-t SENSE

If the signal covariance matrix can be estimated (e.g. using training data), then

$$\overline{\boldsymbol{\rho}\boldsymbol{\rho}^H} = \Theta \tag{B.7}$$

and the prior distribution is

$$Pr\{\boldsymbol{\rho}\} \propto e^{-\frac{1}{2}\|\boldsymbol{\rho}\|} = e^{-\frac{1}{2}\boldsymbol{\rho}^H\Theta^{-1}\boldsymbol{\rho}} \tag{B.8}$$

In *k-t* SENSE, $\boldsymbol{\rho}$ corresponds to the reconstructed signal in the *x-f* space, E to the encoding matrix and d to the undersampled *k*-space data. The posterior probability $Pr\{\boldsymbol{\rho}|\boldsymbol{d}\}$ is maximized when the following Lagrange function is minimized:

$$J(\boldsymbol{\rho}) = (\boldsymbol{d} - E\boldsymbol{\rho})^H \Psi^{-1}(\boldsymbol{d} - E\boldsymbol{\rho}) + \lambda\boldsymbol{\rho}^H \Theta^{-1}\boldsymbol{\rho} \tag{B.9}$$

where λ is the Lagrange multiplier. Expanding Eq. B.9:

$$\begin{aligned} J(\boldsymbol{\rho}) = {} & \boldsymbol{d}^H \Psi^{-1}\boldsymbol{d} - \boldsymbol{d}^H \Psi^{-1} E\boldsymbol{\rho} - \\ & - \boldsymbol{\rho}^H E^H \Psi^{-1}\boldsymbol{d} + \boldsymbol{\rho}^H E^H \Psi^{-1} E\boldsymbol{\rho} + \lambda\boldsymbol{\rho}^H \Theta^{-1}\boldsymbol{\rho} \end{aligned} \tag{B.10}$$

The value of ρ that minimizes $J(\rho)$ satisfies the condition

$$\frac{\partial J}{\partial \boldsymbol{\rho}} = 0 \tag{B.11}$$

Using Wirtinger's calculus, $\partial J/\partial\boldsymbol{\rho}$ can be calculated as follows:

$$\begin{aligned} \frac{\partial J}{\partial \boldsymbol{\rho}} &= 0 - E^H \Psi^{-1}\boldsymbol{d} - E^H \Psi^{-1}\boldsymbol{d} + 2E^H \Psi^{-1} E\boldsymbol{\rho} + 2\lambda\Theta^{-1}\boldsymbol{\rho} \\ &= 2E^H \Psi^{-1}\boldsymbol{d} + 2E^H \Psi^{-1} E\boldsymbol{\rho} + 2\lambda\Theta^{-1}\boldsymbol{\rho} \end{aligned} \tag{B.12}$$

Replacing $\partial J/\partial\boldsymbol{\rho}$ in Eq. B.11, we get:

$$\begin{aligned} E^H \Psi^{-1} E\boldsymbol{\rho} + \lambda\Theta^{-1}\boldsymbol{\rho} = E^H \Psi^{-1}\boldsymbol{d} \Leftrightarrow \\ (E^H \Psi^{-1} E + \lambda\Theta^{-1})\boldsymbol{\rho} = E^H \Psi^{-1}\boldsymbol{d} \Leftrightarrow \\ \boldsymbol{\rho} = (E^H \Psi^{-1} E + \lambda\Theta^{-1})^{-1} E^H \Psi^{-1}\boldsymbol{d} \end{aligned} \tag{B.13}$$

This equation represents one formulation of the *k-t* SENSE algorithm.

Another formulation can be derived using the Woodbury matrix identity. Setting $\lambda = 1$, the reconstruction matrix in Eq. B.13 can be written as:

$$
\begin{aligned}
&(E^H\Psi^{-1}E + \Theta^{-1})^{-1}E^H\Psi^{-1} = \\
&(E^H\Psi^{-1}E + \Theta^{-1})^{-1}E^H\Psi^{-1}\underbrace{(E\Theta E^H + \Psi)(E\Theta E^H + \Psi)^{-1}}_{I} = \\
&(E^H\Psi^{-1}E + \Theta^{-1})^{-1}(E^H\Psi^{-1}E\Theta E^H + E^H\Psi^{-1}\Psi)(E\Theta E^H + \Psi)^{-1} = \\
&(E^H\Psi^{-1}E + \Theta^{-1})^{-1}(E^H\Psi^{-1}E\Theta E^H + E^H)(E\Theta E^H + \Psi)^{-1} = \\
&(E^H\Psi^{-1}E + \Theta^{-1})^{-1}(E^H\Psi^{-1}E\Theta + I)E^H(E\Theta E^H + \Psi)^{-1} = \\
&(E^H\Psi^{-1}E + \Theta^{-1})^{-1}(E^H\Psi^{-1}E\Theta + I)\Theta^{-1}\Theta E^H(E\Theta E^H + \Psi)^{-1} = \\
&(E^H\Psi^{-1}E + \Theta^{-1})^{-1}(E^H\Psi^{-1}E\Theta\Theta^{-1} + \Theta^{-1})\Theta E^H(E\Theta E^H + \Psi)^{-1} = \\
&\underbrace{(E^H\Psi^{-1}E + \Theta^{-1})^{-1}(E^H\Psi^{-1}E + \Theta^{-1})}_{I}\Theta E^H(E\Theta E^H + \Psi)^{-1} = \\
&\Theta E^H(E\Theta E^H + \Psi)^{-1}
\end{aligned}
\tag{B.14}
$$

As such, an equivalent formulation of Eq. B.13 is the following:

$$
\boldsymbol{\rho} = \Theta E^H(E\Theta E^H + \Psi)^{-1}\boldsymbol{d} \tag{B.15}
$$

BIBLIOGRAPHY

[1] Mackay, J., Mensah, G., Mendis, S., Greenlund, K. *The Atlas of Heart Disease and Stroke*. 2004.

[2] Allender, S., Scarborough, P., Peto, V., Rayner, M. *European Cardiovascular Disease Statistics 2008*. *European Heart Network* 2007;1–112.

[3] Association, A. H. *Heart Disease and Stroke Statistics – 2009 Update, American Heart Association* 2009;1–20.

[4] Organization, W. H. *The World Health Report* 2004;1–96.

[5] Leal, J., Luengo-Fernandez, R., Gray, A. *Economic Burden of Cardiovascular Diseases in the Enlarged European Union*. *European Heart Journal* 2006;.

[6] Association, A. H. *Heart Disease and Stroke Statistics – 2008 Update, American Heart Association*. *American Heart Association* 2008;1–41.

[7] Harrison, D. G., White, C. W., Hiratzka, L. F., Doty, D. B., Barnes, D. H., Eastham, C. L., Marcus, M. L. *The Value of Lesion Cross-Sectional Area Determined by Quantitative Coronary Angiography in Assessing the Physiologic Significance of Proximal Left Anterior Descending Coronary Arterial Stenoses*. *Circulation* 1984;69(6):1111–9.

[8] Gould, K. L., Kelley, K. O. *Physiological Significance of Coronary Flow Velocity and Changing Stenosis Geometry During Coronary Vasodilation in Awake Dogs*. *Circulation Research* 1982; 50(5):695–704.

[9] Schwitter, J., Nanz, D., Kneifel, S., Bertschinger, K., Büchi, M., Knüsel, P. R., Marincek, B., Lüscher, T. F., von Schulthess, G. K. *Assessment of Myocardial Perfusion in Coronary Artery Disease by Magnetic Resonance: A Comparison With Positron Emission Tomography and Coronary Angiography*. *Circulation* 2001;103(18):2230–5.

[10] Meza, M. F., Mobarek, S., Sonnemaker, R., Shuler, S., Ramee, S. R., Collins, T. J., White, C. J., Aristizabal, D., Murgo, J. P., Cheirif, J. *Myocardial contrast echocardiography in human beings: correlation of resting perfusion defects to sestamibi single photon emission computed tomography*. *American Heart Journal* 1996;132(3):528–35.

[11] Wei, K., Jayaweera, A. R., Firoozan, S., Linka, A., Skyba, D. M., Kaul, S. *Quantification of Myocardial Blood Flow with Ultrasound-Induced Destruction of Microbubbles Administered as a Constant Venous Infusion*. *Circulation* 1998;97(5):473–83.

[12] Atkinson, D. J., Burstein, D., Edelman, R. R. *First-Pass Cardiac Perfusion: Evaluation With Ultrafast MR Imaging*. *Radiology* 1990; 174(3 Pt 1):757–62.

[13] Manning, Atkinson, D., Grossman, W. *First-Pass Nuclear Magnetic Resonance Imaging Studies Using Gadolinium-DTPA in Patients With Coronary Artery Disease*. *Journal of the American College of Cardiology* 1991;.

[14] Pruessmann, K. P. *Encoding and Reconstruction in Parallel MRI. NMR in biomedicine* 2006;19(3):288–99.

[15] Plein, S., Radjenovic, A., Ridgway, J. P., Barmby, D., Greenwood, J. P., Ball, S. G., Sivananthan, M. U. *Coronary Artery Disease: Myocardial Perfusion MR Imaging With Sensitivity Encoding Versus Conventional Angiography. Radiology* 2005;235(2):423–30.

[16] Köstler, H., Sandstede, J. J. W., Lipke, C., Landschütz, W., Beer, M., Hahn, D. *Auto-SENSE Perfusion Imaging of the Whole Human Heart. Journal of Magnetic Resonance Imaging* 2003;18(6):702–8.

[17] Kellman, P., Derbyshire, J. A., Agyeman, K. O., McVeigh, E. R., Arai, A. E. *Extended Coverage First-Pass Perfusion Imaging Using Slice-Interleaved TSENSE. Magnetic Resonance in Medicine* 2004; 51(1):200–4.

[18] Plein, S., Ryf, S., Schwitter, J., Radjenovic, A., Boesiger, P., Kozerke, S. *Dynamic Contrast-Enhanced Myocardial Perfusion MRI Accelerated With k-t SENSE. Magnetic Resonance in Medicine* 2007;58(4):777–85.

[19] Lauerma, K., Virtanen, K., Sipila, L., Hekali, P., Aronen, H. *Multislice MRI in Assessment of Myocardial Perfusion in Patients With Single-Vessel Proximal Left Anterior Descending Coronary Artery Disease Before and After Revascularization. Circulation* 1997; 96(9):2859–2867.

[20] Machecourt, J., Longere, P., Fagret, D., Vanzetto, G., Wolf, J., Polidori, C., Comet, M., Denis, B. *Prognostic Value of Thallium-201 Single-Photon Emission Computed Tomographic Myocardial Perfusion Imaging According to Extent of Myocardial Defect. Study in 1,926 Patients with Follow-Up at 33 Months. Journal of the American College of Cardiology* 1994;.

[21] Marwick, T. H., Case, C., Sawada, S., Rimmerman, C., Brenneman, P., Kovacs, R., Short, L., Lauer, M. *Prediction of Mortality Using*

Dobutamine Echocardiography. Journal of the American College of Cardiology 2001;37(3):754–60.

[22] Bogaert, J., Dymarkowski, S., Taylor, A. *Clinical Cardiac MRI.* 2005.

[23] Araujo, L. I., Lammertsma, A. A., Rhodes, C. G., McFalls, E. O., Iida, H., Rechavia, E., Galassi, A., Silva, R. D., Jones, T., Maseri, A. *Noninvasive Quantification of Regional Myocardial Blood Flow in Coronary Artery Disease with Oxygen-15-labeled Carbon Dioxide Inhalation and Positron Emission Tomography. Circulation* 1991; 83(3):875–85.

[24] Czernin, J., Muller, P., Chan, S., Brunken, R., ..., G. P. *Influence of Age and Hemodynamics on Myocardial Blood Flow and Flow Reserve. Circulation* 1993;.

[25] Sambuceti, G., Parodi, O., Marcassa, C., Neglia, D. *Alteration in Regulation of Myocardial Blood Flow in One-Vessel Coronary Artery Disease Determined by Positron Emission Tomography. American Journal of Cardiology* 1993;.

[26] Strong, J. P., Malcom, G. T., Oalmann, M. C., Wissler, R. W. *The PDAY Study: Natural History, Risk Factors, and Pathobiology. Pathobiological Determinants of Atherosclerosis in Youth. Annals of the New York Academy of Sciences* 1997;811:226–35; discussion 235–7.

[27] Fuster, V., Corti, R., Fayad, Z., Badimon, J. *Understanding the Pathophysiology of the Arterial Wall: Which Method Should We Choose? European Heart Journal Supplements* 2002;4(F):41–46.

[28] Stary, H. C., Blankenhorn, D. H., Chandler, A. B., Glagov, S., Insull, W., Richardson, M., Rosenfeld, M. E., Schaffer, S. A., Schwartz, C. J., Wagner, W. D. *A Definition of the Intima of Human Arteries and of Its Atherosclerosis-Prone Regions. A Report From the Committee on Vascular Lesions of the Council on Arteriosclerosis, American Heart Association. Arteriosclerosis, Thrombosis and Vascular Biology* 1992; 12(1):120–34.

[29] Yusuf, S., Hawken, S., Ounpuu, S., Dans, T., Avezum, A., Lanas, F., McQueen, M., Budaj, A., Pais, P., Varigos, J., Lisheng, L., Investigators, I. S. *Effect of Potentially Modifiable Risk Factors Associated With Myocardial Infarction in 52 Countries (The INTERHEART Study): Case-Control Study*. *Lancet* 2004;364(9438):937–52.

[30] Fuster, V., Badimon, L., Badimon, J., Chesebro, J. *The Pathogenesis of Coronary Artery Disease and the Acute Coronary Syndromes*. *New England Journal of Medicine* 1992;326(6):242–250.

[31] Moreno, P., Bernardi, V., Lopez-Cuellar, J., Murcia, A., Palacios, I., Gold, H., Mehran, R., Sharma, S., Nemerson, Y., Fuster, V. *Macrophages, Smooth Muscle Cells, and Tissue Factor in Unstable Angina Implications for Cell-Mediated Thrombogenicity in Acute Coronary Syndromes*. *Circulation* 1996;94(12):3090–3097.

[32] Bonetti, P. O., Lerman, L. O., Lerman, A. *Endothelial Dysfunction: A Marker of Atherosclerotic Risk*. *Arteriosclerosis, Thrombosis and Vascular Biology* 2003;23(2):168–75.

[33] Reimer, K. A., Jennings, R. B. *The Changing Anatomic Reference Base of Evolving Myocardial Infarction. Underestimation of Myocardial Collateral Blood Flow and Overestimation of Experimental Anatomic Infarct Size Due to Tissue Edema, Hemorrhage and Acute Inflammation*. *Circulation* 1979;60(4):866–76.

[34] Kloner, R. A., Jennings, R. B. *Consequences of Brief Ischemia: Stunning, Preconditioning, and Their Clinical Implications: Part 2*. *Circulation* 2001;104(25):3158–67.

[35] Lewis, S., Sawada, S., Ryan, T., Segar, D., Armstrong, W., Feigenbaum, H. *Segmental Wall Motion Abnormalities in the Absence of Clinically Documented Myocardial Infarction: Clinical Significance and Evidence of Hibernating Myocardium*. *American Heart Journal* 1991;121(4 Pt 1):1088–94.

[36] Rivas, F., Cobb, F. R., Bache, R. J., Greenfield, J. C. *Relationship Between Blood Flow to Ischemic Regions and Extent of Myocardial Infarction. Serial Measurement of Blood Flow to Ischemic Regions in Dogs*. *Circulation Research* 1976;38(5):439–47.

[37] Sasayama, S. *Effect of Coronary Collateral Circulation on Myocardial Ischemia and Ventricular Dysfunction*. *Cardiovascular Drugs and Therapy* 1994;8:327–334.

[38] Petronio, A. S., Baglini, R., Limbruno, U., Mengozzi, G., Amoroso, G., Cantarelli, A., Vaghetti, M., Distante, A., Balbarini, A., Mariani, M. *Coronary collateral circulation behaviour and myocardial viability in chronic total occlusion treated with coronary angioplasty*. *European Heart Journal* 1998;19(11):1681–7.

[39] Gropler, R., Bergmann, S. *Myocardial Viability-What Is the Definition?* *Journal of Nuclear Medicine* 1991;32(1):10–12.

[40] Grundy, S. M., Pasternak, R., Greenland, P., Smith, S., Fuster, V. *Assessment of Cardiovascular Risk by Use of Multiple-Risk-Factor Assessment Equations: A Statement for Healthcare Professionals From the American Heart Association and the American College of Cardiology*. *Circulation* 1999;100(13):1481–92.

[41] Weinmann, H. J., Brasch, R. C., Press, W. R., Wesbey, G. E. *Characteristics of Gadolinium-DTPA Complex: A Potential NMR Contrast Agent*. *American Journal of Roentgenology* 1984; 142(3):619–24.

[42] Donahue, K. M., Weisskoff, R. M., Burstein, D. *Water Diffusion and Exchange as They Influence Contrast Enhancement*. *Journal of Magnetic Resonance Imaging* 1997;7(1):102–10.

[43] Gerber, B. L., Raman, S. V., Nayak, K., Epstein, F. H., Ferreira, P., Axel, L., Kraitchman, D. L. *Myocardial First-Pass Perfusion Cardiovascular Magnetic Resonance: History, Theory, and Current State of the Art*. *Journal of Cardiovascular Magnetic Resonance* 2008;10(1):18.

[44] Uren, N., Melin, J., Bruyne, B. D., Wijns, W., Baudhuin, T., Camici, P. *Relation Between Myocardial Blood Flow and the Severity of Coronary-Artery Stenosis*. *New England Journal of Medicine* 1994; 330(25):1782–1788.

[45] Fung, A., Gallagher, K., Buda, A. *The Physiologic Basis of Dobutamine as Compared With Dipyridamole Stress Interventions in the Assessment of Critical Coronary Stenosis*. *Circulation* 1987;.

[46] Jayaweera, A. R., Wei, K., Coggins, M., Bin, J. P., Goodman, C., Kaul, S. *Role of Capillaries in Determining CBF Reserve: New Insights Using Myocardial Contrast Echocardiography*. *American Journal of Physiology* 1999;277(6 Pt 2):H2363–72.

[47] Jerosch-Herold, M., Seethamraju, R. T., Swingen, C. M., Wilke, N. M., Stillman, A. E. *Analysis of myocardial perfusion MRI*. *Journal of Magnetic Resonance Imaging* 2004;19(6):758–70.

[48] Schwitter, J. *Myocardial Perfusion*. *Journal of Magnetic Resonance Imaging* 2006;24(5):953–63.

[49] Kellman, P., Arai, A. E. *Imaging Sequences for First Pass Perfusion – A Review*. *Journal of Cardiovascular Magnetic Resonance* 2007; 9(3):525–37.

[50] Wilke, N., Simm, C., Zhang, J., Ellermann, J., Ya, X., Merkle, H., Path, G., Lüdemann, H., Bache, R. J., Uğurbil, K. *Contrast-Enhanced First Pass Myocardial Perfusion Imaging: Correlation Between Myocardial Blood Flow in Dogs at Rest and During Hyperemia*. *Magnetic Resonance in Medicine* 1993;29(4):485–97.

[51] Haase, A. *Snapshot FLASH MRI. Applications to T1, T2, and Chemical-Shift Imaging*. *Magnetic Resonance in Medicine* 1990;13(1):77–89.

[52] Jivan, A., Horsfield, M. A., Moody, A. R., Cherryman, G. R. *Dynamic T1 Measurement Using Snapshot-FLASH MRI*. *Journal of Magnetic Resonance* 1997;127(1):65–72.

[53] Wendland, M. F., Saeed, M., Yu, K. K., Roberts, T. P., Lauerma, K., Derugin, N., Varadarajan, J., Watson, A. D., Higgins, C. B. *Inversion Recovery EPI of Bolus Transit in Rat Myocardium Using Intravascular and Extravascular Gadolinium-Based MR Contrast Media: Dose Effects on Peak Signal Enhancement*. *Magnetic Resonance in Medicine* 1994;32(3):319–29.

[54] Kim, D., Cernicanu, A., Axel, L. *Bo and B1-Insensitive Uniform T1-Weighting for Quantitative, First-Pass Myocardial Perfusion Magnetic Resonance Imaging*. *Magnetic Resonance in Medicine* 2005; 54(6):1423–9.

[55] Kim, D., Gonen, O., Oesingmann, N., Axel, L. *Comparison of the Effectiveness of Saturation Pulses in the Heart at 3T*. *Magnetic Resonance in Medicine* 2008;59(1):209–15.

[56] Judd, R. M., Reeder, S. B., Atalar, E., McVeigh, E. R., Zerhouni, E. A. *A Magnetization-Driven Gradient Echo Pulse Sequence for the Study of Myocardial Perfusion*. *Magnetic Resonance in Medicine* 1995; 34(2):276–82.

[57] Bertschinger, K., Nanz, D., Buechi, M., Luescher, T. F., Marincek, B., von Schulthess, G. K., Schwitter, J. *Magnetic resonance myocardial first-pass perfusion imaging: parameter optimization for signal response and cardiac coverage*. *Journal of Magnetic Resonance Imaging* 2001;14(5):556–62.

[58] Reeder, S. B., Faranesh, A. Z., Boxerman, J. L., McVeigh, E. R. *In Vivo Measurement of T*2 and Field Inhomogeneity Maps in the Human Heart at 1.5 T*. *Magnetic Resonance in Medicine* 1998;39(6):988–98.

[59] Noeske, R., Seifert, F., Rhein, K. H., Rinneberg, H. *Human Cardiac Imaging at 3 T Using Phased Array Coils*. *Magnetic Resonance in Medicine* 2000;44(6):978–82.

[60] Singerman, R. W., Denison, T. J., Wen, H., Balaban, R. S. *Simulation of B1 Field Distribution and Intrinsic Signal-to-Noise in Cardiac MRI*

as a Function of Static Magnetic Field. *Journal of Magnetic Resonance* 1997;125(1):72–83.

[61] Oesingmann, N., Zhang, Q., Simonetti, O. *Improved Saturation RF Pulse Design for Myocardial First-Pass Perfusion at 3T*. *Journal of Cardiovascular Magnetic Resonance* 2004;6(1):373–374.

[62] Sung, K., Nayak, K. S. *Design and Use of Tailored Hard-Pulse Trains for Uniformed Saturation of Myocardium at 3 Tesla*. *Magnetic Resonance in Medicine* 2008;60(4):997–1002.

[63] Ogg, R., Kingsley, P., Taylor, J. *WET, a T1-and B1-insensitive water-suppression method for in vivo localized 1H NMR Spectroscopy*. *Journal of magnetic resonance. Series B* 1994;.

[64] Kim, D., Oesingmann, N., McGorty, K. *Hybrid Adiabatic-Rectangular Pulse Train for Effective Saturation of Magnetization Within the Whole Heart at 3T*. *Magnetic Resonance in Medicine* 2009; 62(6):1368–78.

[65] Ding, S., Wolff, S. D., Epstein, F. H. *Improved Coverage in Dynamic Contrast-Enhanced Cardiac MRI Using Interleaved Gradient-Echo EPI*. *Magnetic Resonance in Medicine* 1998;39(4):514–9.

[66] Epstein, F. H., Wolff, S. D., Arai, A. E. *Segmented k-space Fast Cardiac Imaging Using an Echo-Train Readout*. *Magnetic Resonance in Medicine* 1999;41(3):609–13.

[67] Schreiber, W. G., Schmitt, M., Kalden, P., Mohrs, O. K., Kreitner, K.-F., Thelen, M. *Dynamic Contrast-Enhanced Myocardial Perfusion Imaging Using Saturation-Prepared TrueFISP*. *Journal of Magnetic Resonance Imaging* 2002;16(6):641–52.

[68] Elkington, A. G., Gatehouse, P. D., Cannell, T. M., Moon, J. C., Prasad, S. K., Firmin, D. N., Pennell, D. J. *Comparison of Hybrid Echo-Planar Imaging and FLASH Myocardial Perfusion Cardiovascular MR Imaging*. *Radiology* 2005;235(1):237–43.

[69] Fenchel, M., Helber, U., Simonetti, O. P., Stauder, N. I., Kramer, U., Nguyen, C.-N., Finn, J. P., Claussen, C. D., Miller, S. *Multislice First-Pass Myocardial Perfusion Imaging: Comparison of Saturation Recovery (SR)-TrueFISP-Two-Dimensional (2D) and SR-TurboFLASH-2D Pulse Sequences*. *Journal of Magnetic Resonance Imaging* 2004; 19(5):555–63.

[70] Wang, Y., Moin, K., Akinboboye, O., Reichek, N. *Myocardial First Pass Perfusion: Steady-State Free Precession Versus Spoiled Gradient Echo and Segmented Echo Planar Imaging*. *Magnetic Resonance in Medicine* 2005;54(5):1123–9.

[71] Ishida, N., Sakuma, H., Motoyasu, M., Okinaka, T., Isaka, N., Nakano, T., Takeda, K. *Noninfarcted myocardium: correlation between dynamic first-pass contrast-enhanced myocardial MR imaging and quantitative coronary angiography*. *Radiology* 2003;229(1):209–16.

[72] Nagel, E., Klein, C., Paetsch, I., Hettwer, S., Schnackenburg, B., Wegscheider, K., Fleck, E. *Magnetic Resonance Perfusion Measurements for the Noninvasive Detection of Coronary Artery Disease*. *Circulation* 2003;108(4):432–7.

[73] Sakuma, H., Suzawa, N., Ichikawa, Y., Makino, K., Hirano, T., Kitagawa, K., Takeda, K. *Diagnostic accuracy of stress first-pass contrast-enhanced myocardial perfusion MRI compared with stress myocardial perfusion scintigraphy*. *American Journal of Roentgenology* 2005;185(1):95–102.

[74] Schwitter, J., Wacker, C. M., Rossum, A. C. V., Lombardi, M., Al-Saadi, N., Ahlstrom, H., Dill, T., Larsson, H. B. W., Flamm, S. D., Marquardt, M., Johansson, L. *MR-IMPACT: Comparison of Perfusion-Cardiac Magnetic Resonance with Single-Photon Emission Computed Tomography for the Detection of Coronary Artery Disease in a Multicentre, Multivendor, Randomized Trial*. *European Heart Journal* 2008;29(4):480–9.

[75] Al-Saadi, N., Nagel, E., Gross, M., Bornstedt, A., Schnackenburg, B., Klein, C., Klimek, W., Oswald, H., Fleck, E. *Noninvasive Detection of Myocardial Ischemia From Perfusion Reserve Based on Cardiovascular Magnetic Resonance*. *Circulation* 2000;101(12):1379–83.

[76] Panting, J. R., Gatehouse, P. D., Yang, G. Z., Jerosch-Herold, M., Wilke, N., Firmin, D. N., Pennell, D. J. *Echo-Planar Magnetic Resonance Myocardial Perfusion Imaging: Parametric Map Analysis and Comparison With Thallium SPECT*. *Journal of Magnetic Resonance Imaging* 2001;13(2):192–200.

[77] Gebker, R., Jahnke, C., Paetsch, I., Schnackenburg, B., Kozerke, S., Bornstedt, A., Fleck, E., Nagel, E. *MR Myocardial Perfusion Imaging with k-Space and Time Broad-Use Linear Acquisition Speed-up Technique: Feasibility Study*. *Radiology* 2007;245(3):863–71.

[78] Al-Saadi, N., Nagel, E., Gross, M., Schnackenburg, B., Paetsch, I., Klein, C., Fleck, E. *Improvement of Myocardial Perfusion Reserve Early After Coronary Intervention: Assessment With Cardiac Magnetic Resonance Imaging*. *Journal of the American College of Cardiology* 2000;36(5):1557–64.

[79] Jerosch-Herold, M., Hu, X., Murthy, N. S., Rickers, C., Stillman, A. E. *Magnetic resonance imaging of myocardial contrast enhancement with MS-325 and its relation to myocardial blood flow and the perfusion reserve*. *Journal of Magnetic Resonance Imaging* 2003;18(5):544–54.

[80] Wilke, N., Jerosch-Herold, M., Wang, Y., Huang, Y., Christensen, B. V., Stillman, A. E., Ugurbil, K., McDonald, K., Wilson, R. F. *Myocardial perfusion reserve: assessment with multisection, quantitative, first-pass MR imaging*. *Radiology* 1997;204(2):373–84.

[81] Cullen, J. H., Horsfield, M. A., Reek, C. R., Cherryman, G. R., Barnett, D. B., Samani, N. J. *A Myocardial Perfusion Reserve Index in Humans Using First-Pass Contrast-Enhanced Magnetic Resonance Imaging*. *Journal of the American College of Cardiology* 1999;33(5):1386–94.

[82] Jerosch-Herold, M., Wilke, N., Wang, Y., Gong, G. R., Mansoor, A. M., Huang, H., Gurchumelidze, S., Stillman, A. E. *Direct Comparison of an Intravascular and an Extracellular Contrast Agent for Quantification of Myocardial Perfusion.* *Int J Card Imaging* 1999; 15(6):453–64.

[83] Panting, J. R., Gatehouse, P. D., Yang, G.-Z., Grothues, F., Firmin, D. N., Collins, P., Pennell, D. J. *Abnormal subendocardial perfusion in cardiac syndrome X detected by cardiovascular magnetic resonance imaging.* *New England Journal of Medicine* 2002;346(25):1948–53.

[84] Sipola, P., Lauerma, K., Husso-Saastamoinen, M., Kuikka, J. T., Vanninen, E., Laitinen, T., Manninen, H., Niemi, P., Peuhkurinen, K., Jääskeläinen, P., Laakso, M., Kuusisto, J., Aronen, H. J. *First-Pass MR Imaging in the Assessment of Perfusion Impairment in Patients With Hypertrophic Cardiomyopathy and the Asp175Asn Mutation of the α-Tropomyosin Gene.* *Radiology* 2003;226(1):129–37.

[85] Thompson, H., Starmer, C., Whalen, R., McIntosh, H. *Indicator Transit Time Considered as a Gamma Variate.* *Circulation Research* 1964;14:502–15.

[86] Zierler, K. *Theoretical Basis of Indicator-Dilution Methods For Measuring Flow and Volume.* *Circulation Research* 1962; 10(3):393–407.

[87] Zierler, K. L. *Equations for Measuring Blood Flow by External Monitoring of Radioisotopes.* *Circulation Research* 1965;16:309–21.

[88] Jerosch-Herold, M., Wilke, N., Stillman, A. E. *Magnetic Resonance Quantification of the Myocardial Perfusion Reserve With a Fermi Function Model for Constrained Deconvolution.* *Medical Physics* 1998; 25(1):73–84.

[89] Tsekos, N. V., Zhang, Y., Merkle, H., Wilke, N., Jerosch-Herold, M., Stillman, A., Uğurbil, K. *Fast Anatomical Imaging of the Heart*

and Assessment of Myocardial Perfusion With Arrhythmia Insensitive Magnetization Preparation. Magnetic Resonance in Medicine 1995; 34(4):530–6.

[90] Strich, G., Hagan, P., Gerber, K., Slutsky, R. *Tissue Distribution and Magnetic Resonance Spin Lattice Relaxation Effects of Gadolinium-DTPA. Radiology* 1985;.

[91] Koenig, S. H., Spiller, M., Brown, R. D., Wolf, G. L. *Relaxation of Water Protons in the Intra- and Extracellular Regions of Blood Containing Gd (DTPA). Magnetic Resonance in Medicine* 1986;3(5):791–5.

[92] Donahue, K. M., Weisskoff, R. M., Chesler, D. A., Kwong, K. K., Bogdanov, A. A., Mandeville, J. B., Rosen, B. R. *Improving MR Quantification of Regional Blood Volume With Intravascular T1 Contrast Agents: Accuracy, Precision, and Water Exchange. Magnetic Resonance in Medicine* 1996;36(6):858–67.

[93] Weinberg, I. N., Huang, S. C., Hoffman, E. J., Araujo, L., Nienaber, C., Grover-McKay, M., Dahlbom, M., Schelbert, H. *Validation of PET-Acquired Input Functions for Cardiac Studies. Journal of Nuclear Medicine* 1988;29(2):241–7.

[94] Axel, L. *Tissue Mean Transit Time From Dynamic Computed Tomography by a Simple Deconvolution Technique. Investigative Radiology* 1983;.

[95] Kroll, K., Wilke, N., Jerosch-Herold, M., Wang, Y., Zhang, Y., Bache, R. J., Bassingthwaighte, J. B. *Modeling Regional Myocardial Flows From Residue Functions of an Intravascular Indicator. American Journal of Physiology* 1996;271(4 Pt 2):H1643–55.

[96] Jerosch-Herold, M., Swingen, C., Seethamraju, R. T. *Myocardial Blood Flow Quantification With MRI by Model-Independent Deconvolution. Medical Physics* 2002;29(5):886–97.

[97] Pack, N. A., DiBella, E. V. R., Rust, T. C., Kadrmas, D. J., McGann, C. J., Butterfield, R., Christian, P. E., Hoffman, J. M. *Estimating myocardial perfusion from dynamic contrast-enhanced CMR with a model-independent deconvolution method. Journal of Cardiovascular Magnetic Resonance* 2008;10(1):52.

[98] Verotta, D. *Two constrained deconvolution methods using spline functions. Journal of Pharmacokinetics and Biopharmaceutics* 1993; 21(5):609–36.

[99] Verotta, D. *Estimation and Model Selection in Constrained Deconvolution. Annals of Biomedical Engineering* 1993;21(6):605–20.

[100] Hansen, P. *Analysis of Discrete Ill-Posed Problems by Means of the L-Curve. SIAM review* 1992;34(4):561–580.

[101] Gould, K. L., Lipscomb, K. *Effects of coronary stenoses on coronary flow reserve and resistance. American Journal of Cardiology* 1974; 34(1):48–55.

[102] Schaper, W., Wüsten, B., Flameng, W., Scholtholt, J., Winkler, B., Pasyk, S. *Local Dilatory Reserve in Chronic Experimental Coronary Occlusion Without Infarction. Quantitation of Collateral Development. Basic Res Cardiol* 1975;70(2):159–73.

[103] McFalls, E., Araujo, L., Lammertsma, A. *Vasodilator Reserve in Collateral-Dependent Myocardium as Measured by Positron Emission Tomography. European Heart Journal* 1993;.

[104] Weisskoff, R. M., Chesler, D., Boxerman, J. L., Rosen, B. R. *Pitfalls in MR Measurement of Tissue Blood Flow with Intravascular Tracers: Which Mean Transit Time? Magnetic Resonance in Medicine* 1993; 29(4):553–8.

[105] Ostergaard, L., Sorensen, A. G., Kwong, K. K., Weisskoff, R. M., Gyldensted, C., Rosen, B. R. *High Resolution Measurement of Cerebral Blood Flow Using Intravascular Tracer Bolus Passages. Part*

II: Experimental Comparison and Preliminary Results. Magnetic Resonance in Medicine 1996;36(5):726–36.

[106] Bella, E. V. R. D., Parker, D. L., Sinusas, A. J. *On the Dark Rim Artifact in Dynamic Contrast-Enhanced MRI Myocardial Perfusion Studies. Magnetic Resonance in Medicine* 2005;54(5):1295–9.

[107] Storey, P., Chen, Q., Li, W., Edelman, R. R., Prasad, P. V. *Band Artifacts Due to Bulk Motion. Magnetic Resonance in Medicine* 2002;48(6):1028–36.

[108] Pruessmann, K. P., Weiger, M., Scheidegger, M. B., Boesiger, P. *SENSE: Sensitivity Encoding for Fast MRI. Magnetic Resonance in Medicine* 1999;42(5):952–62.

[109] Wiesinger, F., Boesiger, P., Pruessmann, K. P. *Electrodynamics and Ultimate SNR in Parallel MR Imaging. Magnetic Resonance in Medicine* 2004;52(2):376–90.

[110] Dornier, C., Ivancevic, M. K., Thévenaz, P., Vallée, J.-P. *Improvement in the Quantification of Myocardial Perfusion Using an Automatic Spline-Based Registration Algorithm. Journal of Magnetic Resonance Imaging* 2003;18(2):160–8.

[111] Gupta, S. N., Solaiyappan, M., Beache, G. M., Arai, A. E., Foo, T. K. F. *Fast Method for Correcting Image Misregistration Due to Organ Motion in Time-Series MRI Data. Magnetic Resonance in Medicine* 2003;49(3):506–14.

[112] Cernicanu, A., Axel, L. *Theory-based signal calibration with single-point T1 measurements for first-pass quantitative perfusion MRI studies. Acad Radiol* 2006;13(6):686–93.

[113] Axel, L., Hayes, C. *Surface Coil Magnetic Resonance Imaging. Archives of Physiology and Biochemistry* 1985;93(5):11–8.

[114] Christian, T. F., Aletras, A. H., Arai, A. E. *Estimation of Absolute Myocardial Blood Flow During First-Pass MR Perfusion Imaging*

Using a Dual-Bolus Injection Technique: Comparison to Single-Bolus Injection Method. *Journal of Magnetic Resonance Imaging* 2008; 27(6):1271–7.

[115] Hsu, L., Rhoads, K., Holly, J., Kellman, P., Aletras, A., Arai, A. *Quantitative Myocardial Perfusion Analysis With a Dual-Bolus Contrast-Enhanced First-Pass MRI Technique in Humans*. *Journal of Magnetic Resonance Imaging* 2006;23(3):315.

[116] Kim, D., Axel, L. *Multislice, Dual-Imaging Sequence for Increasing the Dynamic Range of the Contrast-Enhanced Blood Signal and CNR of Myocardial Enhancement at 3T*. *Journal of Magnetic Resonance Imaging* 2006;23(1):81–6.

[117] Elkington, A. G., He, T., Gatehouse, P. D., Prasad, S. K., Firmin, D. N., Pennell, D. J. *Optimization of the Arterial Input Function for Myocardial Perfusion Cardiovascular Magnetic Resonance*. *Journal of Magnetic Resonance Imaging* 2005;21(4):354–9.

[118] Tsao, J., Boesiger, P., Pruessmann, K. P. *k-t BLAST and k-t SENSE: Dynamic MRI with High Frame Rate Exploiting Spatiotemporal Correlations*. *Magnetic Resonance in Medicine* 2003;50(5):1031–42.

[119] Jung, B., Honal, M., Hennig, J., Markl, M. *k-t-Space Accelerated Myocardial Perfusion*. *Journal of Magnetic Resonance Imaging* 2008; 28:1080–1085.

[120] Vitanis, V., Manka, R., Boesiger, P., Kozerke, S. *Accelerated Cardiac Perfusion Imaging Using k-t SENSE With SENSE Training*. *Magnetic Resonance in Medicine* 2009;62(4):955–65.

[121] Cárdenas-Blanco, A., Tejos, C., Irarrazaval, P. *Noise in Magnitude Magnetic Resonance Images*. *Concepts in Magnetic Resonance Part A* 2008;32A(6):409–416.

[122] Johnson, J. *Thermal agitation of electricity in conductors*. *Physical Review* 1928;32(1):97–109.

[123] Nyquist, H. *Thermal agitation of electric charge in conductors*. *Physical Review* 1928;32(1):110–113.

[124] Haacke, E. M., Brown, R. W., Thompson, M. R., Venkatesan, R. *Magnetic Resonance Imaging: Physical Principles and Sequence Design*. 1999.

[125] Hoult, D. *The Principle of Reciprocity in Signal Strength Calculations-a Mathematical Guide*. *Concepts in Magnetic Resonance* 2000; 12(4):173–187.

[126] Wiesinger, F., de Moortele, P.-F. V., Adriany, G., Zanche, N. D., Ugurbil, K., Pruessmann, K. P. *Potential and Feasibility of Parallel MRI at High Field*. *NMR in biomedicine* 2006;19(3):368–78.

[127] Kellman, P., McVeigh, E. R. *Image Reconstruction in SNR Units: A General Method for SNR Measurement*. *Magnetic Resonance in Medicine* 2005;54(6):1439–47.

[128] Pruessmann, K. P., Weiger, M., Börnert, P., Boesiger, P. *Advances in Sensitivity Encoding With Arbitrary k-Space Trajectories*. *Magnetic Resonance in Medicine* 2001;46(4):638–51.

[129] Golub, G., Loan, C. V. *Matrix Computations*. 1996.

[130] Roemer, P. B., Edelstein, W. A., Hayes, C. E., Souza, S. P., Mueller, O. M. *The NMR Phased Array*. *Magnetic Resonance in Medicine* 1990; 16(2):192–225.

[131] Xiang, Q. S., Henkelman, R. M. *K-Space Description for MR Imaging of Dynamic Objects*. *Magnetic Resonance in Medicine* 1993;29(3):422–8.

[132] Pedersen, H., Kozerke, S., Ringgaard, S., Nehrke, K., Kim, W. Y. *k-t PCA: Temporally Constrained k-t BLAST Reconstruction Using Principal Component Analysis*. *Magnetic Resonance in Medicine* 2009; 62(3):706–16.

[133] Tsao, J., Kozerke, S., Boesiger, P., Pruessmann, K. P. *Optimizing Spatiotemporal Sampling for k-t BLAST and k-t SENSE: Application to High-Resolution Real-Time Cardiac Steady-State Free Precession*. *Magnetic Resonance in Medicine* 2005;53(6):1372–82.

[134] Plein, S., Kozerke, S., Suerder, D., Luescher, T. F., Greenwood, J. P., Boesiger, P., Schwitter, J. *High Spatial Resolution Myocardial Perfusion Cardiac Magnetic Resonance for the Detection of Coronary Artery Disease*. *European Heart Journal* 2008;29:2148–2155.

[135] Samsonov, A., Bella, E. D., Kellman, P., Kholmovski, E., Johnson, C. *Adaptive k-t BLAST – k-t SENSE for Accelerating Cardiac Perfusion MRI*. *SCMR Proceedings* 2005;1.

[136] Kozerke, S., Plein, S. *Accelerated CMR Using Zonal, Parallel and Prior Knowledge Driven Imaging Methods*. *Journal of Cardiovascular Magnetic Resonance* 2008;10(1):29.

[137] Kellman, P., Epstein, F., McVeigh, E. R. *Adaptive Sensitivity Encoding Incorporating Temporal Filtering (TSENSE)*. *Magnetic Resonance in Medicine* 2001;45(5):846–852.

[138] Huang, F., Akao, J., Vijayakumar, S., Duensing, G. *k-t GRAPPA: A k-space Implementation for Dynamic MRI with High Reduction Factor*. *Magnetic Resonance in Medicine* 2005;54(5):1172–1184.

[139] Hansen, M. S., Kozerke, S., Pruessmann, K. P., Boesiger, P., Pedersen, E. M., Tsao, J. *On the Influence of Training Data Quality in k-t BLAST Reconstruction*. *Magnetic Resonance in Medicine* 2004;52(5):1175–83.

[140] Sánchez-González, J., Tsao, J., Dydak, U., Desco, M., Boesiger, P., Pruessmann, K. P. *Minimum-Norm Reconstruction for Sensitivity-Encoded Magnetic Resonance Spectroscopic Imaging*. *Magnetic Resonance in Medicine* 2006;55(2):287–95.

[141] Dydak, U., Weiger, M., Pruessmann, K., Meier, D., Boesiger, P. *Sensitivity-Encoded Spectroscopic Imaging*. *Magnetic Resonance in Medicine* 2001;46(4):713–722.

[142] Hestenes, M. R., Stiefel, E. *Methods of Conjugate Gradients for Solving Linear Systems*. *Journal of Research of the National Bureau of Standards* 1952;49:409–436.

[143] Xu, D., King, K. F., Liang, Z.-P. *Improving k-t SENSE by Adaptive Regularization*. *Magnetic Resonance in Medicine* 2007;57(5):918–30.

[144] Noll, D. C., Nishimura, D. G., Macovski, A. *Homodyne Detection in Magnetic Resonance Imaging*. *IEEE Transactions on Medical Imaging* 1991;10(2):154–63.

[145] Fischer, S. E., Wickline, S. A., Lorenz, C. H. *Novel Real-Time R-Wave Detection Algorithm Based on the Vectorcardiogram for Accurate Gated Magnetic Resonance Acquisitions*. *Magnetic Resonance in Medicine* 1999;42(2):361–70.

[146] Swets, J. *Measuring the Accuracy of Diagnostic Systems*. *Science* 1988; .

[147] DeLong, E. R., DeLong, D. M., Clarke-Pearson, D. L. *Comparing the Areas Under Two or More Correlated Receiver Operating Characteristic Curves: A Nonparametric Approach*. *Biometrics* 1988; 44(3):837–45.

[148] Bland, J. M., Altman, D. G. *Statistical Methods for Assessing Agreement Between Two Methods of Clinical Measurement*. *Lancet* 1986;1(8476):307–10.

[149] Cheng, A. S. H., Pegg, T. J., Karamitsos, T. D., Searle, N., Jerosch-Herold, M., Choudhury, R. P., Banning, A. P., Neubauer, S., Robson, M. D., Selvanayagam, J. B. *Cardiovascular Magnetic Resonance Perfusion Imaging at 3-Tesla for the Detection of Coronary Artery Disease: A Comparison With 1.5-Tesla*. *Journal of the American College of Cardiology* 2007;49(25):2440–9.

[150] Shaw, L. *Differential Improvement in Stress Myocardial Perfusion Ischemia Following Percutaneous Coronary Intervention as Compared

With Optimal Medical Therapy Alone: Nuclear Substudy Results From the Clinical Outcomes Utilizing Revascularization and Aggressive Drug Evaluation (COURAGE) Trial. Proc. American Heart Association 2007;Scientific Sessions(Late-breaking clinical trials 1).

[151] Weiger, M., Pruessmann, K. P., Boesiger, P. *2D SENSE for Faster 3D MRI. MAGMA* 2002;14(1):10–9.

[152] Kellman, P., Zhang, Q., Larson, A., Simonetti, O., McVeigh, E. R., Arai, A. E. *Cardiac First-Pass Perfusion MRI Using 3D trueFISP Parallel Imaging Using TSENSE. Proc. International Society for Magnetic Resonance in Medicine* 2004;(12th Meeting):310.

[153] Shin, T., Hu, H. H., Pohost, G. M., Nayak, K. S. *Three Dimensional First-Pass Myocardial Perfusion Imaging at 3T: Feasibility Study. Journal of Cardiovascular Magnetic Resonance* 2008;10(1):57.

[154] McLeish, K., Hill, D., Atkinson, D., Blackall, J., Razavi, R. *A Study of the Motion and Deformation of the Heart Due to Respiration. IEEE Transactions on Medical Imaging* 2002;21(9):1142–1150.

[155] Buehrer, M., Pruessmann, K. P., Boesiger, P., Kozerke, S. *Array Compression for MRI With Large Coil Arrays. Magnetic Resonance in Medicine* 2007;57(6):1131–9.

[156] Buehrer, M., Boesiger, P., Kozerke, S. *Virtual Body Coil Calibration for Phased-Array Imaging. Proc. International Society for Magnetic Resonance in Medicine* 2009;(17th Meeting):760.

[157] Ostergaard, L. *Cerebral Perfusion Imaging by Bolus Tracking. Topics in magnetic resonance imaging : TMRI* 2004;15(1):3–9.

[158] Pack, N. A., DiBella, E. V. R. *Comparison of Myocardial Perfusion Estimates From Dynamic Contrast-Enhanced Magnetic Resonance Imaging With Four Quantitative Analysis Methods. Magnetic Resonance in Medicine* 2010;64(1):125–137.

[159] Odille, F., Vuissoz, P.-A., Marie, P.-Y., Felblinger, J. *Generalized Reconstruction by Inversion of Coupled Systems (GRICS) Applied to Free-Breathing MRI.* *Magnetic Resonance in Medicine* 2008; 60(1):146–57.

[160] Zun, Z., Wong, E., Nayak, K. *Assessment of myocardial blood flow (MBF) in humans using arterial spin labeling (ASL): Feasibility and noise analysis.* *Magnetic Resonance in Medicine* 2009;62(4).

[161] Grobner, T. *Gadolinium–a specific trigger for the development of nephrogenic fibrosing dermopathy and nephrogenic systemic fibrosis?* *Nephrol Dial Transplant* 2006;21(4):1104–8.

LIST OF PUBLICATIONS

Journals

[1] Vitanis, V., Manka, R., Giese, D., Pedersen, H., Plein, S., Boesiger, P., Kozerke S. *High Resolution 3D Myocardial Perfusion Imaging using k-t PCA. Magnetic Resonance in Medicine, Under Review*

[2] Manka, R., Jahnke, C., Kozerke, S., Vitanis, V., Crelier, G., Gebker, R., Schnackenburg, B., Boesiger, P., Fleck, F., Paetsch, I. *Dynamic Three-Dimensional Stress Cardiac Magnetic Resonance Perfusion Imaging: Detection of Coronary Artery Disease and Volumetry of Myocardial Ischemic Burden Before and After Coronary Stenting. Journal of the American College of Cardiology, 2010, In Press*

[3] Manka, R., Vitanis, V., Boesiger, P., Flammer, A., Plein, S., Kozerke, S. *Clinical Validation of Highly Accelerated High Spatial Resolution Myocardial Perfusion Imaging, JACC Imaging 2010;vol.3(7):710–717*

[4] Vitanis, V., Manka, R., Boesiger, P., Kozerke, S. *Clinical Validation of Highly Accelerated High Spatial Resolution Myocardial Perfusion Imaging, Magnetic Resonance in Medicine 2010;vol.62:955–965*

Invited Papers

[5] Vitanis, V., Manka, R., Boesiger, P., Kozerke, S. *High Resolution 3D Myocardial Perfusion Imaging Using Compartment-Based k-t PCA, Proc. 32nd Annual International IEEE EMBS Conference, Buenos Aires, Argentina 2010; p.1585*

Proceedings

[6] Vitanis, V., Manka, Pedersen, H., Boesiger, P., Kozerke S. *High Resolution 3D Cardiac Perfusion Imaging using Compartment-based k-t PCA, Proc. ISMRM, 18th Annual Meeting, Stockholm, Sweden, 2010, p.3628*

[7] Manka, R., Jahnke, C., Kozerke, S., Vitanis, V., Crelier, G., Gebker, R., Schnackenburg, B., Boesiger, P., Fleck, F., Paetsch, I. *Three-Dimensional Stress Cardiac Magnetic Resonance Perfusion Imaging for the Detection of Coronary Artery Disease. Proc. ISMRM, 18th Annual Meeting, Stockholm, Sweden, 2010, p.583*

[8] Manka, R., Jahnke, S., Kozerke, S., Vitanis, V., Crelier, G., Gebker, R., Schnackenburg, B., Boesiger, P., Fleck, E., Paetsch, I. *Three-Dimensional Stress Cardiac Magnetic Resonance Perfusion Imaging for the Detection of Coronary Artery Disease and Quantification of Myocardial Ischemic Burden, Proc. DGK, 76th Annual Meeting, Mannheim, Germany, 2010, V636*

[9] Vitanis, V., Manka, R., Boesiger, P., Pedersen, H., Kozerke, S. *High Resolution 3D Cardiac Perfusion Imaging using k-t PCA, Proc. SCMR, 13th Annual Meeting, Phoenix, USA, 2010, p.107*

[10] Manka, R., Vitanis, V., Boesiger, Plein, S., Kozerke, S. *Highly Accelerated High Spatial Resolution Myocardial Perfusion Imaging, Proc. SCMR, 13th Annual Meeting, Phoenix, USA, 2010, p.74*

[11] Vitanis, V., Manka, R., Boesiger, Kozerke, S. *High Resolution First-pass Myocardial Perfusion using k-t SENSE, Proc. ESMRMB, 25th Annual Meeting, Valencia, Spain, 2008, p.195*

[12] Vitanis, V., Manka, R., Boesiger, P., Kozerke, S. *A Modified k-t SENSE Algorithm for High Resolution 3D First-Pass Myocardial Perfusion, Proc. Rapid MR Imaging Workshop, Freiburg, Germany, 2008*

[13] Vitanis, V., Gamper, P., Boesiger, Plein, S., Kozerke, S. *Compressed Sensing Cardiac Perfusion Imaging: Feasibility and Comparison to k-t BLAST, Proc. SCMR, 11th Annual Meeting, Los Angeles, USA, 2008, p.1143*

[14] Vitanis, V., Plein, S., Boesiger, P., Kozerke, S. *Highly Accelerated k-t SENSE Cardiac Perfusion Imaging, Proc. ISMRM, 15th Annual Meeting, Berlin, Germany, 2007, p.848*

[15] Vitanis, V., Boesiger, P., Kozerke, S. *Highly Accelerated k-t SENSE with Improved Temporal Fidelity, Proc. ESMRMB, 23rd Annual Meeting, Warsaw, Poland, 2006, p.156*

[16] Vitanis, V., Baltes, C., Tsao, J., Hansen, M.S., Boesiger, P., Kozerke, S. *Highly Accelerated k-t SENSE Using Large Coil Arrays, Proc. BMT, Annual Meeting, Zurich, Switzerland, 2006*

[17] Vitanis, V., Baltes, C., Tsao, J., Hansen, M.S., Boesiger, P., Kozerke, S. *Highly Accelerated k-t SENSE Using Large Coil Arrays, Proc. ISMRM, 14th Annual Meeting, Seattle, USA, 2006, p. 142*

CURRICULUM VITAE

I was born on February 15, 1982, in Drama, Greece, as son of Nikolaos and Lemonia Vitanis. After primary school in Drama and Eleftheroupoli, Greece, I attended high-school in Elefteroupoli, from which I received my diploma in June 1999.

From 1999 to 2004 I studied Electrical and Computer Engineering at the Polytechnic School of the Aristotle University of Thessaloniki, Greece, with a specialization in Electronics and Computers. In 2003 I did an internship at the Institute of Surgical Technology and Biomechanics of the MEM Research Center, University of Bern, Switzerland. I graduated in Autumn 2004 after having completed my diploma thesis entitled “Vascularization of Tumor Growth Models: A particle-based approach”, carried out at the Computer Vision Laboratory of the ETH Zurich, Switzerland.

Since September 2005 I have been working as teaching and research assistant at the Institute for Biomedical Engineering, University and ETH Zurich, in the Biophysics group of Prof. P. Boesiger.